University of Pennsylvania
ScholarlyCommons

Publicly Accessible Penn Dissertations

1-1-2014

Designing Nanomaterials For Electronic And Optoelectronic Devices Through Charge Carrier Control

soong ju Oh
University of Pennsylvania, sooo@seas.upenn.edu

Follow this and additional works at: http://repository.upenn.edu/edissertations

Part of the Electrical and Electronics Commons, Mechanics of Materials Commons, and the Nanoscience and Nanotechnology Commons

Recommended Citation
Oh, soong ju, "Designing Nanomaterials For Electronic And Optoelectronic Devices Through Charge Carrier Control" (2014). *Publicly Accessible Penn Dissertations*. 1392.
http://repository.upenn.edu/edissertations/1392

This paper is posted at ScholarlyCommons. http://repository.upenn.edu/edissertations/1392
For more information, please contact libraryrepository@pobox.upenn.edu.

Designing Nanomaterials For Electronic And Optoelectronic Devices Through Charge Carrier Control

Abstract
Colloidal semiconductor nanocrystals (NCs) have been shown to be promising materials for electronic and optoelectronic device applications because of their unique size-dependent properties and low-cost solution processability. However, the integration of these materials into devices has been challenging due to a lack of available methods to: 1) accurately control charge carrier statistics, such as majority carrier type and concentration, and carrier mobilities, and 2) efficiently passivate surface defects inherent in NC materials arising from their high surface-volume ratio.

In this thesis, we study the fundamental physics of charge carriers paramount for device application. Then, we introduce several measurement techniques to characterize the type, concentration, and mobility of charge carriers and the density and energy of surface states. Lastly, we propose a novel, systematic, and rational method to engineer those properties, in order to design high performance electronic and optoelectronic nanostructured devices.

We develop stoichiometry control method through thermal evaporation or solution based atomic layer deposition to precisely control the electronic and optoelectronic properties of nanocrystals. We demonstrate that remote doping in nanostructured device is effective and a promising route to realizing high mobility and reducing scattering, in contrast to commonly pursued substitutional doping methods. Thermal diffusion doping process to passivate the trap states and the use of small ligands to enhance the electronic coupling are introduced. In addition, we emphasize the important role of the metal-semiconductor interface and semiconductor-gate dielectric layer, to enhance charge injection and prevent charge trapping, respectively. Through the careful engineering of the interface and junction, as well as the precise charge carrier statistics and trap states controls, we design and fabricate low cost, high performance nanocrystal thin film field-effect transistors, photodetectors, and solar cells.

Finally, we introduce novel techniques, correlated scanning photocurrent microscopy and scanning confocal photoluminescence measurement system, that can explore the photoelectric and photophysical properties of semiconductor structures and devices.

Degree Type
Dissertation

Degree Name
Doctor of Philosophy (PhD)

Graduate Group
Materials Science & Engineering

First Advisor
Cherie R. Kagan

This dissertation is available at ScholarlyCommons: http://repository.upenn.edu/edissertations/1392

Keywords
charge carriers, electronic device, lead chalcogenide, Nanocrystals, optoelectronic device, semiconductor

Subject Categories
Electrical and Electronics | Mechanics of Materials | Nanoscience and Nanotechnology

This dissertation is available at ScholarlyCommons: http://repository.upenn.edu/edissertations/1392

DESIGNING NANOMATERIALS FOR ELECTRONIC AND OPTOELECTRONIC DEVICES THROUGH CHARGE CARRIER CONTROL

Soong Ju Oh

A DISSERTATION

in

Materials Science and Engineering

Presented to the Faculties of the University of Pennsylvania

in

Partial Fulfillment of the Requirements for the

Degree of Doctor of Philosophy

2014

Supervisor of Dissertation

Signature _____

Cherie R. Kagan, Stephen J. Angello Professor, Materials Science & Engineering

Graduate Group Chairperson

Signature _____

Shu Yang, Professor, Materials Science & Engineering

Dissertation Committee

Christopher B. Murray, Richard Perry University Professor, Materials Science & Engineering

Nader Engheta, H. Nedwill Ramsey Professor, Electrical System & Engineering

Ritesh Agarwal, Associate Professor, Materials Science & Engineering

DESIGNING NANOMATERIALS FOR ELECTRONIC AND OPTOELECTRONIC DEVICES

THROUGH CHARGE CARRIER CONTROL

COPYRIGHT

2014

Soong Ju Oh

This work is licensed under the
Creative Commons Attribution-
NonCommercial-ShareAlike 3.0
License

To view a copy of this license, visit

http://creativecommons.org/licenses/by-ny-sa/2.0/

To my Families

ACKNOWLEDGMENT

First and foremost, I would like to express my sincere gratitude to my adrvisor, Professor Cherie Kagan. She has been tremendous mentor for me and is always willing to help me and committed all the time. I have enjoyed the constructive and pleasant discussion with her. I respect the way she taught me and admire her as a great researcher, scientist and mentor. Without her endless supervision and support, it would not have been possible to finish the dissertation.

I'm also grateful from my former and current group members : Dr. Ji-hyuk Choi, Dr. Sung Hoon Hong, Dr. David K. Kim, Dr. Aaron Fafarman, Dr. Tae Kwon Lee, Dr. Guozhong Xing, Dr. Pual Frail, Dr. Sangam Saudari, Dr. Wenting Li, Dr. Marjan Saboktakin, Yuming Lai, Ed Goodwin, Eric Wong, Nathaniel Berry, Wenxiang Chen, Scott Stinner, Nicholas Greybush, Daniel Straus, Leo Tianshuo Zhao, Hangfei Lin, Jessi Zhuqwang Li, Michael Crump, Han Wang, Li Xie, Qian Gao, Prashanth Gopalan, Diya Li, Francisco Lee, Devika Mehta, Kevin Fritz, Emily Gurniak, William Cheng, and also Murray group: Dr. Dong-Kyun Ko, Dr. Xing Chen, Dr. Jun Chen, Dr.Weon-Kyu Koh, Dr. Taejong Paik, Ashley Gaulding, Ben Diroll, Vicky Doan-Nguyen, Danielle Reifsnyder. I thank to Dr. Jongbok Kim and Prof. Lynn Loo for the great collaboration. It was my pleasure to learn the real meaning of collaboration with my colleague and have great and special time to spend time with you in the states.

Last but not least, I would like to express my endless thanks and appreciations to my family – my wife Gayeon Son and my son Phillip Juwon Oh - for their support and patience for me to accomplish my goals. Thank you for being with me. I promise that I will be a good husband and father.

ABSTRACT

DESIGNING NANOMATERIALS FOR ELECTRONIC AND OPTOELECTRONIC DEVICES THROUGH CHARGE CARRIER CONTROL

Soong Ju Oh

Prof. Cherie R. Kagan

Colloidal semiconductor nanocrystals (NCs) have been shown to be promising materials for electronic and optoelectronic device applications because of their unique size-dependent properties and low-cost solution processability. However, the integration of these materials into devices has been challenging due to a lack of available methods to: 1) accurately control charge carrier statistics, such as majority carrier type and concentration, and carrier mobilities, and 2) efficiently passivate surface defects inherent in NC materials arising from their high surface-volume ratio.

In this thesis, we study the fundamental physics of charge carriers paramount for device application. Then, we introduce several measurement techniques to characterize the type, concentration, and mobility of charge carriers and the density and energy of surface states. Lastly, we propose a novel, systematic, and rational method to engineer those properties, in order to design high performance electronic and optoelectronic nanostructured devices.

We develop stoichiometry control method through thermal evaporation or solution based atomic layer deposition to precisely control the electronic and optoelectronic properties of nanocrystals. We demonstrate that remote doping in

nanostructured device is effective and a promising route to realizing high mobility and reducing scattering, in contrast to commonly pursued substitutional doping methods. Thermal diffusion doping process to passivate the trap states and the use of small ligands to enhance the electronic coupling are introduced. In addition, we emphasize the important role of the metal-semiconductor interface and semiconductor-gate dielectric layer, to enhance charge injection and prevent charge trapping, respectively. Through the careful engineering of the interface and junction, as well as the precise charge carrier statistics and trap states controls, we design and fabricate low cost, high performance nanocrystal thin film field-effect transistors, photodetectors, and solar cells.

Finally, we introduce novel techniques, correlated scanning photocurrent microscopy and scanning confocal photoluminescence measurement system, that can explore the photoelectric and photophysical properties of semiconductor structures and devices.

TABLE OF CONTENTS

1. Introduction

1.1. Semiconductors and semiconducting nanocrystals

1.1.1. Semiconductors

1.1.2. Semiconductor nanocrystals

1.2. Bulk and nanoscale lead chalcogenide semiconductors

1.3. Synthesis of NCs and lead chalcogenide NCs

1.4. Shape and structures of lead selenide NCs

1.5. Charge transport in semiconductors and NC thin film devices

1.5.1. Developments of NC thin films

1.5.2. Charge transport in semiconductors

1.5.3. Charge transport in NC thin films

1.5.4. Characterization of charge transport

1.6. Thesis Overview

1.7. References

2. Stoichiometry Control of Lead Chalcogenide Nanocrystals to Enhance the Electronic and Optoelectronic Device Performance

2.1. Introduction

2.2. Experimental details

2.3. Results and Discussions

2.3.1. Stoichiometric Control of PbSe NCs to Enhance the Electronic Properties

2.3.2. Carrier Statistics characterized by Hall and Capacitance-Voltage Measurement

2.3.3. PbSe Schottky Solar cell enhanced by non-stoichiometry

2.4. Conclusions

2.5. References

3. Designing High-Performance PbS and PbSe Nanocrystal Electronic Devices through Stepwise, Post-Synthesis, Colloidal Atomic Layer Deposition

3.1. Introduction

3.2. Experimental Details

3.2.1. Post-Synthtic-Colloidal Atomic Layer Deposition Method

3.3. Results and Discussions

3.3.1. Optical, Structural Properties of Chalcogen-rich and Pb-rich Lead chalcogenide NCs

3.3.2. Electronic Properties of Chalcogen-rich and Pb-rich Lead chalcogenide NCs.

3.4. Conclusions

3.5. References

4. Charge Injection and Transport Study of PbSe nanocrystal thin film solids

4.1. Introduction

4.2. Experimental Details

4.3. Results and Discussions

4.3.1. Band diagram of PbSe NC FETs

4.3.2. Charge injection and transport at room temperature

4.3.3. Conductivity and mobility of PbSe NC thin film solids

4.3.4. Variable temperature charge injection study

4.3.5. Variable temperautre charge transport study

4.4. Conclusions

4.5. References

5. Remote Doping and Schottky Barrier Formation in Strongly Quantum Confined Single PbSe Nanowire Field-Effect Transistors

5.1. Introduction

5.2. Experimental Details

5.3. Results and Discussions

5.3.1. Schotty Barrier FET Behavior revealed by Temperature Dependent Electrical Measurement

5.3.2. Charge Injection and Transport as a Function of Doping

5.4. Conclusions

5.5. References

6. Strongly-Coupled and In-doped CdSe NC Thin Film for Air Stable and High Performance Electronic and Optoelectronic Device

6.1. CdSe NC thin film photodetector through strong electronic coupling with thiocyanate ligands

6.2. High performance CdSe NC FETs through the combination of strong electronic coupling and indium doping.

6.3. Air stable NC FETs though recovery by In diffusion and ALD passivation

6.3. References

7. Correlated Scanning photocurrent microscopy and scanning confocal photoluminescence microscopy to investigate the photoelectric and photophysical properties of semiconductor structures and devices

7.1. Introduction

7.2. Experimental details

7.2.1. SPCM and SPLM on bulk heterojunction

7.2.2. SPCM and SPLM on patterend device

7.3. Results and discussions

7.4. References

8. Conclusions

8.1. Future works

8.1.1. P-N junctions on a single PbSe NW and PbS NC thin films

8.1.2. Investigation of charge carrier physics in NW and NC thin films using spatially resolved photocurrent measurement

8.1.3. Post-deposited, passivation of traps in NC thin films.

8.2. Concluding remarks

LIST OF TABLES

Table 2.1. Hall measurement data

Table 3.1 Stoichiometry changes of PbSe NC thin films during Post-Synthetic, colloidal Atomic Layer deposition monitored by ICP-OES and EDX

Table 3.2 Carrier concentration of Se-rich PbSe NC thin films before and as a function of the time of $PbCl_2$ treatment as measured by Capacitance-Voltage and Hall techniques.

LIST OF ILLUSTRATIONS

Figure 1.1 (A) Schematic plot of electron energy as a function of interatomic separation for an aggregate of 6 atoms (N=6) As they become closer, each of 1s and 2s atomic states splits to form an electron energy band consisting of 6 states (B) Simplifed energy level diagrams for four different types. The shaded boxes represent the fillled valence bands, the empty boxes represent the empty conduction bands at 0K. The arrows represent the forbidden band gap, E_G.

Figure 1.2 (A) Density of states in one band of a semiconductor as a function of dimension (B) Energy level diagram comparing a bulk semiconductor to its molecular analog and a quantum dot. The semiconductor's electrons are in bands. The molecule's electrons are in molecular orbitals or bonds. The electronic structure of a semiconductor quantum dot is in the intermediate regime between bands and bonds.

Figure 1.3 (A) Simple effective mass approximation to build a parabolic energy diagram (E vs k) of conduction and valence bands of a semiconductor. The confinement of NC quantizes the allowed k values. Decreasing the NC diameter shifts the first state to larger values of k and increase the separation between each state. (B) i. absorption spectrum of CdSe NCs at r.t. As size decreases, a greater blue shift in the absorption edge and a larger separation between electronic transitions occur. ii. The discrete electronic transitions in optical absorption (C) Scanning Tunneling Spectroscopy of the different size of InAs NCs. Representative tunnelling dI/dV versus V characteristics of different size of NCs shows the evolution of discrete electronic states.

Figure 1.4 (A) the change of volume energy, surface energy, and total free energy, as functions of nucleus' radius. (B) Schematic of the nucleation and growth of NCs as a function of time (La Mer model). (C) Schematic of the experimental setup to synthesize monodisperse NCs.

Figure 1.5 (A) Schematic of 6nm PbSe NCs. (B)Absorption spectroscopy, (C) Fourier Transform Infra-Red spectroscopy, (D) wide angle and (inset) small angle X-ray Diffraction pattern, (E) scanning electron microscopy, and (F) transmission electron microscopy of 6nm PbSe NCs. (scale bar : (E) 100nm, (F) 25nm)

Figure 2.1 (A) Schematic of stoichiometric control of PbX NC thin films by Pb or Se deposition (B) Fermi energy of PbX NCs as a function of the concentration of Pb (red) or Se (blue) atoms added to NC thin films

Figure 2.2 (A) Schematic of a PbX NC FET device and (inset) SEM image of a SCN-treated 6 nm PbSe NC thin film solid (scale bar : 100nm), (B) transfer characteristics of (black) as-synthesized and exchanged, (red) 1 Å excess Pb and (blue) 0.1 Å excess Se PbSe NC FETs and output characteristics of the (C) Pb-rich NC FETs with varying V_G from 0V to 50V and (D) Se-rich PbSe NC FETs with varying V_G from 0V to -50V.

Figure 2.3 (A) Transfer characteristics of PbSe NC FETs in the saturation regime (black) before and after (red) 1 Å, (green) 2 Å, (blue) 3 Å, and (purple) 4 Å of Pb deposition. (B)

Transfer characteristics of PbSe NC FET devices in the saturation regime (black) before and after (red) 0.1 Å, (green) 0.2 Å, (blue) 0.3 Å, (purple) 0.4 Å and 0.5 Å (brown) of Se deposition (C) Transfer characteristics of a PbSe NC FET in the linear regime after 3 Å of Pb deposition (D) Transfer characteristics of PbSe NC FETs in the saturation regime with NC channel thickness' of (black) 35 nm, (red) 70 nm, (green) 105 nm, (blue) 140 nm. Dashed line and solid line indicate before and after deposition of 1 Å of Pb, respectively. (E) Transfer characteristics in the saturation regime of SCN treated PbS NC FETs (black) before and after (red) 2 Å excess Pb and (blue) 0.2 Å excess Se deposition. (F) Transfer characteristics in the saturation regime of (black) before and after (red) 2 Å excess Pb and (blue) 0.2 Å excess Se PbSe NC FETs. Solid and dashed lines indicate before and after 12 hours of under vacuum of 10^{-7} Torr.

Figure 2.4 (A) Schematic of a metal-semiconductor (PbSe NC thin film)-insulator-metal (MSIM) structure for capacitance voltage (C-V) measurements, (B) equivalent circuit of the channel where r is the sheet resistance, dx is the elements of length in the channel, W is channel width, C_{NC} is capacitance of NC thin film, and C_{OX} is capacitance of oxide in the channel (C) C-V plot (black) before and after (red) 0.3 Å, (pink) 0.6 Å, (green) 0.9 Å, (blue) 1.2 Å, and (purple) 2 Å of Pb deposited (D) C-V plot (black) before and after (red) 0.3 Å, (pink) 0.6 Å, (green) 0.9 Å, and (blue) 1.2 Å of Se deposited.

Figure 2.5 (A) Schematic of 2.5 nm PbSe NC Schottky solar cell and device cross sectional SEM image (scale bar : 100nm), (B) current density-voltage characteristics of (black) pristine, after deposition of (red) 0.2 Å excess Pb and (blue) 0.2 Å excess Se, (C) band diagrams for (black) pristine, (red) Pb-rich and (blue) Se-rich PbSe NC Schottky junctions with Al electrodes, and (D) current density-voltage characteristics of Se-rich solar cells (black) before and after (red) 0.1 Å, (orange) 0.2 Å, (green) 0.4 Å, (blue) 0.8 Å and (purple) 2 Å of Se deposited.

Figure 3.1 Post-Synthetic, colloidal Atomic Layer Deposition (PS-cALD) of lead chalcogenide NC thin films. Schematic of NC assemblies, detailed illustration of the interface between NCs and TEM images exemplified by 5.9 nm PbSe NCs. (A) As-synthesized, spincast NC thin films, are treated in solutions of either Na_2Se, Na_2S, or KHS (B) to exchange the long-insulating ligands introduced during synthesis and to chalcogen enrich the NC surface. Further treatment with $PbCl_2$ (C) enriches the NC film in Pb. For the simplified picture, the organic and inorganic ligands are omitted and the atoms at the interface may reconstruct to minimize energy. (scale bar : 20nm)

Figure 3.2 (A) Absorption spectra of as-synthesized 5.9 nm PbSe NC thin films (black) and upon Se (blue) and Pb (red) enrichment. Inset : The first excitonic peak of Se-rich PbSe NCs before (blue) and after 10 s (green), 1 min (yellow), 1 h (orange), 12 h (red), and 24 h (purple) of $PbCl_2$ treatment at 65 ºC, or 10 min of $PbCl_2$ treatment at 95 ºC (grey). (B) Absorption spectra of as-synthesized 6 nm PbS NC thin films (black) and upon S (blue) and Pb (red) enrichment. Inset : The first excitonic peak of S-rich PbS NCs before (blue) and after 10 s (green), 1 min (yellow), 1 h (orange), 12 h (red), 24 h (purple) of $PbCl_2$ treatment at 65 ºC, or 10 min of $PbCl_2$ treatment at 95 ºC (grey). (C) Wide angle X-ray scattering for as-synthesized (black), Na_2Se (blue) and both $PbCl_2$ and Na_2Se (red)

treated PbSe NC thin films. (D) The red shift and broadening of the first excitonic peak of PbSe and PbS NCs with different chalcogenide exchange chemistries and after $PbCl_2$ treatment.

Figure 3.3 Absorption spectra of (A) Na_2Se treated and (B) subsequently $PbCl_2$ treated PbSe NC thin films as a function of exposure time to air. X-ray photoelectron spectroscopy of the Se 3d peak for (C) Na_2Se and (D) and subsequently $PbCl_2$ treated PbSe NC thin films. TEM images of Se-rich PbSe NC assemblies treated with Na_2Se, followed by air exposure for (E) 1min and (F) several days. Note these TEM images (E, F) are collected from the same region of the NC sample.

Figure 3.4 (A) Schematic of a PbE (E = S or Se) NC thin-film field effect transistor. (Note: The figure is not drawn to scale and the NC thin films comprise small ordered domains.) (B) Transfer curves of Na_2Se treated PbSe NCs before (black) and after $PbCl_2$ treatment for 1 h (blue), 6 h (green), and 12 h (red) at 65 ºC. (C) p-type output characteristics of a PbSe NC thin film FET treated with Na_2Se followed by 1 h of 10 mM $PbCl_2$ at 65 ºC. (D) n-type output characteristics of a PbSe NC thin film FET treated with Na_2Se followed by 12 h of $PbCl_2$ at 65 ºC. Output characteristics in the linear regime of (E) a PbSe NC FET treated with Na_2Se followed by 10 min with $PbCl_2$ at 95 ºC and (F) a PbS NC FET treated with Na_2S followed by 10 min with $PbCl_2$ at 95 ºC.

Figure 4.1 Schematic of PbSe NC field-effect transistors with different contact metallurgy (left) and different ligand chemistries (right).

Figure 4.2 (A) Cyclic voltammetry measurements (red : forward scan, black : reverse scan) and (B) absorption spectra for 6 nm PbSe NCs exchanged with (black) oleic acid, (red) MPA, (blue) EDT, (purple), SCN (grey), Na_2Se (green). (C) Band diagrams constructed from cyclic voltammetry and absorption measurements for a few representative ligand-exchanged PbSe NC thin films in comparison to the work function for Au (Ag, Cr, and Al are also shown on the left side).

Figure 4.3 PbSe NCs FETs treated with (A) BDT, (B) TBAI, (C) EDT, (D), NH_4Cl, (E) MPA and (F) TMAOH, with (red) Al, (green) Cr, (blue) Ag, (purple) Au.

Figure 4.4 Band diagram depicting charge injection and transport in PbSe NC thin films with (A) long and (B) short ligands for FETs fabricated with high work function Au contacts and with (C) long and (D) short ligands for FETs fabricated with low work function Al contacts.

Figure 4.5 (A) PbSe NC FETs treated with TBAI with bottom contact Al electrodes as a function of time in the nitrogen glovebox with an oxygen level of ~1ppm. (B) Conductivity of PbSe NC thin films with (black) MPA and (blue) SCN, (green) SCN followed by $PbCl_2$ with Au contact, (red) SCN followed by $PbCl_2$ with Al contact,. (C) PbSe NC FETs with (red) TBAI, (green) NH_4Cl, (blue) Na_2Se and $PbCl_2$, (black) SCN and $PbCl_2$ with Au contact. (D) PbSe NC FETs with SCN and $PbCl_2$ with Au contact.

Figure 4.6. Temperature dependent FET measurements of PbSe NC thin films treated with TBAI and contacted by (A) Al and (B) Au electrodes. Temperature dependent electrical measurement of current (C) in the electron accumulation regime with V_G=50V, and (D) in the off-state with VG~-20V.

Figure 4.7. Temperature-dependent electron and hole currents for PbSe NC FETs with Au contacts treated with (A) MPA, (B) EDT, and with Al contacts treated with (C) TBAI, (D) SCN and $PbCl_2$ and Se and $PbCl_2$ for (E) short and (F) long treatment times.

Figure 5.1 (A) Schematic of PbSe single nanowire (SNW) FET device and (B) SEM image of single NW device

Figure 5.2 Output characteristics in the (A) hole and (B) electron accumulation regimes and (C) transfer characteristics at (black) V_{DS}=-2V and (red) V_{DS}=+2V of an ambipolar, PbSe SNW FET. (D) Schematic band diagram of an ambipolar SNW FET. LUMO is the lowest unoccupied molecular orbital, HOMO is the highest occupied molecular orbital, E_F is the Fermi energy, Φ_m is the work function of metal, Φ_{Be} is the electron barrier height, Φ_{Bh} is the hole barrier height, χ is the electron affinity of the PbSe NW.

Figure 5.3 Ambipolar PbSe SNW FET (A) transfer characteristics at 4K (Red), 140K (Blue) and 298K (Black) and (inset) schematic band diagrams as a function of V_G and (B) electron mobility and hole mobility as a function of temperature.

Figure 5.4 (A) I_D-V_{DS} curves at V_G=0.2V at temperatures between 77K and 298K (B) Arrhenius plot of I_D at different V_{DS} and (inset) the activation energy as a function of $V_{DS}^{1/2}$ (C) Calculated barrier heights as a function of V_G. (D) Schematic band diagrams of the metal-semiconductor interface representing charge injection for constant energy gap materials at (i) high and (ii) low temperature and for materials with a positive dE_G/dT at (iii) high and (iv) low temperature. M is metal, S is semiconductor, E is energy, n is number of electrons, and x is distance. Red and blue lines indicate the electron distribution[35)] *versus* energy at high temperature and low temperature, respectively, and the arrows indicate the amplitude of electron injection from metal to semiconductor.

Figure 5.5 p-type PbSe SNW FET (A) Transfer characteristics at 4K (Red), 140K (Blue) and 298K (Black); (B) output characteristics at 4.5K. Inset magnifies the low voltage region of the I_D-V_{DS} characteristics at 4.5K (red) and 298K (black). (C) transfer characteristics at 4.5K (D) Saturation mobility as a function of temperature for holes in a unipolar p-type and electrons in a predominantly n-type PbSe SNW FET.

Figure 6.1 (A) Schematic of the ligand exchange process and (B) photoconductivity of a SCN-treated CdSe NC thin film on quartz. Dark current (black) and photo current for 488 nm illumination at 30 mW/cm^2 (green). (Inset : Spectral response and absorption spectra for the CdSe NC thin film).

Figure 6.2 (A) Photograph of SCN-treated CdSe NC films on Si wafers with varying film thickness from 25 nm (left) to 130 nm (right). (B) Output and (C) transfer characteristics

with various V_{DS} (0.1 V to 50 V) for a CdSe NC thin film FET annealed at 250 ˚C for 10 min. Inset in (B) is a schematic of the device structure.

Figure 6.3 (A) Lateral distribution of $113In^+$ as a function of depth (left) pre-annealed and (right) post-annealed sample. (inset : a schematic of the measured 100 × 100 μm^2 sample area.) (B) Depth profile of the $113In^+$ distribution for pre-annealed and post-annealed samples. (C) Conductivity of CdSe NC thin films on quartz with In/Au and Al electrodes as a function of annealing temperature. (Inset : the conductivity of CdSe NC thin films annealed with different indium thickness) (D) Capacitance-Voltage characteristics of CdSe NC thin films as function of gate-voltage annealed at a temperature from 200 ^oC to 250 ^oC.

Figure 6.4 (A) Transfer characteristics of CdSe NC thin film FETs with an Al_2O_3/SiO_2 gate dielectric stack at V_{DS}=0.1 V (inset : device output characteristics) (B) Temperature dependent mobilities of CdSe NC FETs with SiO_2 and Al_2O_3/SiO_2 gate dielectric stacks.

Figure 6.5 (A) I_D-V_G characteristics of CdSe NC thin films annealed at 250 ^oC for 10 min prior to In/Au electrode deposition (red) and then annealed at 250 ^oC for 10 min to allow indium diffusion and device doping (blue), exposed to air for 30 min (green), and re-annealed at 200 ^oC for 5 min (black). (B) Schematic of NC FET recovery after air exposure: (i) indium-doped CdSe NC devices, (ii) once exposed to air adsorb oxygen and water at the NC and gate oxide surfaces and (iii) are recovered upon annealing under nitrogen as oxygen and water desorbs and additional indium diffuses from the electrode reservoirs.

Figure 6.6 (A) Cyclic degradation as a function of air exposure time and recovery upon re-annealing at 200 ^oC for 5 min for FETs fabricated on Al_2O_3 and SiO_2 gate dielectric stacks. (B) Degradation in air versus in pure oxygen environment (open bar : initial, filled bar : exposure) for Al_2O_3 and SiO_2 gate dielectric stacks. (C) As-prepared (black) and upon successive cycles of air exposure for 30 min (red) and recovery by annealing at 200 ^oC for 5 min (blue) on Al_2O_3 and (inset) SiO_2 gate dielectric stacks.

Figure 6.7. (A) Al_2O_3 encapsulated NC FET electron mobility (black) and threshold voltage (blue) as a function of time stored and operated in air. (B) A photograph of NC FETs fabricated by photolithography on flexible Kapton substrates (C) Output and (D) transfer characteristics (V_{DS}=0.1, 2V) of flexible, NC FETs (channel length L=30 μm, width W=450 μm). [inset (C)] Schematic of the device structure.

Figure 7.1 (A) Microscope image and photocurrent map of P3HT/PCBM solar cells (top) without and (bottom) with a compatibilizer. (B) (left) Schematic and AFM image of wrinkles and folds and (right) the photocurrent map of P3HT/PCBM solar cells for surfaces that are (i) flat and (ii) with wrinkles and folds under 750 nm illumination (C) (left, top) Photograph and (left, botom) schematic of SPCM investigation of a striped PbSe NC thin film photoconductor. (right, top) 2D, and (right, down) 1D photocurrent mapping overlaid on the optical image of a striped PbSe NC film. (D) (left) Schematic

and (right) photocurrent map of plasmonic enhancement of a monolayer of nanophosphors separated by an Al_2O_3 thin film from a patterned Au NP layer.

Figure 7.2 (A) Schematic of the correlated, scanning photocurrent microscopy and scanning confocal photoluminescence microscopy setup. (B) BHJ solar cell structure and (C) line scan mapping the microscopic PC and PL across a BHJ solar cell.

Figure 7.3 (A) Schematic and (B) photograph of the PCBM/P3HT bilayer (left) and P3HT only step junction (right). EDX mapping the carbon content (C) before and (D) after annealing at 130 ºC for 3 min.

Figure 7.4. Line scan of PC and PL on a patterned device (A) before and (B) after annealing at 130 ºC for 3 min.

Figure 7.5 Hole mobility as a function of distance (A) before and (B) after annealing. Inset (A) a schematic of conductive atomic force microscopy characterization of the junction.

Figure 8.1 (A) Schematic of P-N junction on PbSe NW arrays, (B) Rectifying behavior or P-N junction NW array and (inset) SEM images of P-N junction with blocking layer, (C) band diagram of P-N junction on PbSe NW, , and (D) schematic of P-N junction on single PbSe NW with multiple electrodes.

Figure 8.2 Schematic of Post-deposited Passivation of trap states in NC thin films

Figure 8.3 (A) schematic of heterojunction PbS NC solar cell, (B) the efficiency of PbS solar cell before and after $PbCl_2$ and $CdCl_2$ treatment, and (C) the absorption spectroscopy of MPA-treated PbS NC thin films before and after $PbCl_2$ treatment.

CHAPTER 1 Introduction

1.1 Semiconductors and semiconducting nanocrystals

1.1.1 Semiconductors

Solids are classified into three categories based on their electrical resistivity: metals, semiconductors, and insulators.[1] The difference in electrical resistivity results from the different electronic band structures of the three types of solids. Solids are composed of atoms and each atom consists of a nucleus and electrons surrounding the nuclei. In a simple Bohr model, electrons have quantized energy and are located at discrete energy levels or states. As the number, N, of atoms get closer together, the electrons are perturbed and by the other nuclei or electrons and each electron state is split into N states [Figure 1.1 (A)].[1] If N is very large, then those split and quantized states appear to be a continuous band.[1]

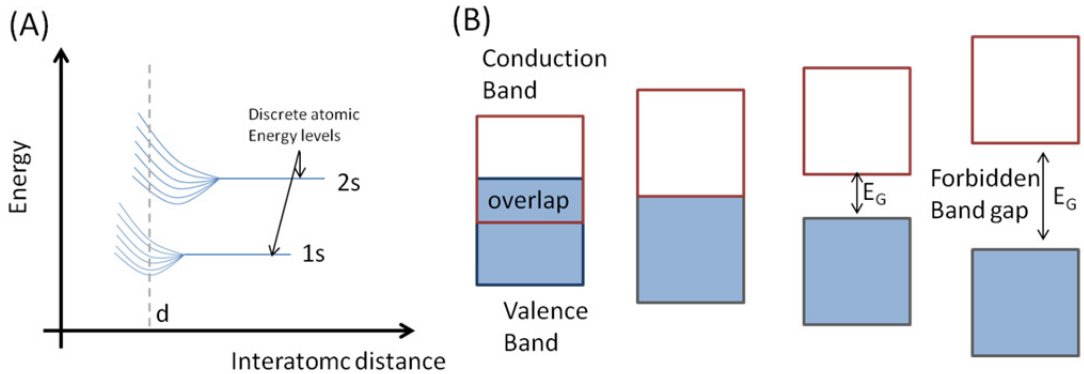

Figure 1.1 (A) Schematic plot of electron energy as a function of interatomic separation for an aggregate of 6 atoms (N=6) As they become closer, each of 1s and 2s atomic states splits to form an electron energy band consisting of 6 states (B) Simplifed energy level diagrams for four different types. The shaded boxes represent the fillled valence bands, the empty boxes represent the empty conduction bands at 0K. The arrows represent the forbidden band gap, E_G.

When these N atoms are arranged in an equilibrium crystal structure, the electronic structure shows bands and band gaps. Electrons cannot be located in the forbidden band gaps, and can only be within the bands. Electrons fill the available states from the lowest energy in accordance with the Pauli Exclusion principle. In this way, the electron configuration and Fermi energy are determined. The Fermi energy is defined as the highest energy level filled with electrons at T=0K, or the energy level in which a probability of occupancy of electron is 0.5 when T>0K.[2] The electron configuration, especially the outermost band, determines the electronic properties of solids. Figure 1.1 (B) shows the four cases of band structure. In the first case, there is no band gap as two most outer bands overlap. In the second case, the highest energy electrons are in the middle of the band, meaning that only half the band is filled. In the third, the outermost filled band or valence band is separated from the higher empty band, the conduction band, and the small band gap lies between them. The fourth case is the same as the third except the band gap is large.[1]

These electronic configurations determine the conductivity and the category of the solid. Specifically, the rate of electron transport upon the electric field dictates the electronic conductivity of the solid. Only electrons that have energy higher than the Fermi energy can be changed, move and therefore contribute to the electrical conduction. These are called free electrons. In the first and second cases of Figure 1.1 (B), the electrons need only a very small amount of energy in order to jump to the next level, within the thermal energy of k_BT, where k_B is Boltzmann's constant and T is temperature. Thus there are numerous free electrons that contribute to high electrical conductivity, and

these solids are classified as conductors or metals.[1] However, in the third and fourth cases of Figure 1.1 (B), electrons need a higher energy, E_G, to jump from the valence band to the conduction band and conduct freely through the material. When E_G is around or higher than ~3eV, the electrons cannot readily excite to the conduction band, and the solid does not conduct electrons through it well and therefore called an insulator.[1] However, if E_G is less than 2eV, it is termed a semiconductor.[1] In a semiconductor, the density of conduction electrons above E_F can be controlled by temperature, dopants, or an external field, and the electrical conductivity can be varied, typically within the range of $10^{-8} \sim 10^{3}$ S/cm.[1,2] This level of control over electronic properties and conductivity make semiconductors the basis of circuit design, fundamental to transistors, diodes, and memory. This extensively researched class of materials is the beating heart that powers our technological life.

1.1.2 Semiconductor nanocrystals

As technology has trended towards smaller and smaller devices, the dimension of semiconductor devices has decreased as well, from 3D to 2D, 1D and eventually 0D. As the dimensionality shrinks, the electronic properties and band structure also change. As stated, it is crucial to understand the electron statistics and band structure to predict the material's properties. The total number of electrons N(E) at each energy, dE, is determined by 1) how many allowed states exists in the range from E to E+dE, or the

density of states, D(E), and 2) how many electrons exist at energy E, as described by the distribution function f(E).[2]

$$N(E)dE = D(E)\, f(E)\, dE$$

The distribution of electrons is described by the Fermi-Dirac distribution

$$f(E) = \frac{1}{(\exp((E - E_F)/k_B T) + 1)}$$

The density of states, D(E) can be deduced from the time-independent Schrödinger equation for free electrons,

$$-\frac{\hbar}{2m}\left(\frac{\partial^2}{\partial x^2} + \frac{\partial^2}{\partial y^2} + \frac{\partial^2}{\partial z^2}\right)\psi_k(r) = E\psi_k(r)$$

Given the boundary conditions imposed by the 3-, 2-, 1- and 0-D cases, the density of states can be shown to be the following:

$$D(E)dE = \frac{(2m)^3}{2\pi^2\hbar^3}\sqrt{E}\, dE$$

$$D(E)dE = \frac{m}{\pi\hbar^2}\, dE$$

$$D(E)dE = \frac{m}{\pi\hbar\sqrt{2}}\frac{1}{\sqrt{E}}\, dE$$

$$D(E)dE = 2\delta(E)dE$$

In 0-D, the density of states is described as a delta function, as there is no k-space that can be filled with electrons and the only available states exist discretely. Figure 1.2 (A) shows the density of states in each space.[3]

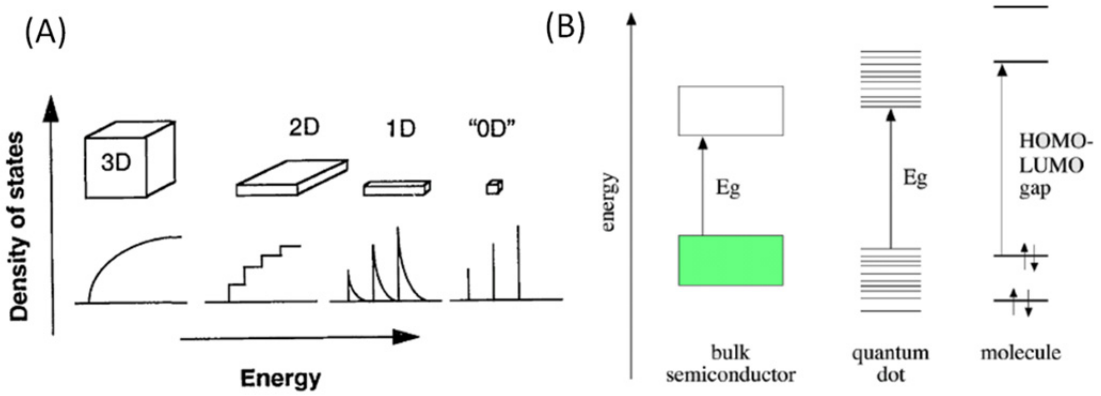

Figure 1.2 (A) Density of states in one band of a semiconductor as a function of dimension [Adapted from reference 3] (B) Energy level diagram comparing a bulk semiconductor to its molecular analog and a quantum dot. The semiconductor's electrons are in bands. The molecule's electrons are in molecular orbitals or bonds. The electronic structure of a semiconductor quantum dot is in the intermediate regime between bands and bonds. [Adapted from reference 4]

Semiconductor nanocrystals are small crystalline semiconducting materials with a spatial dimension of 1-100nm. However, this term implicitly refers to 0-D nanocrystals, often called quantum dots due to the quantization of states [Figure 1.2 (A)]. In this thesis, the term semiconductor nanocrystal denotes a 0-D nanocrystal. When the size of the semiconductor is reduced to the nanometer scale, the electronic and optical properties are dramatically changed. The continuous band becomes quantized states [Figure 1.2 (A)], resembling the pseudo states between molecules and bulk [Figure 1.2 (B)].[4] This is due to the quantum confinement effect. Carriers, electrons and holes, feel the strong spatial confinement due to the physical barriers at the surfaces. The situation is completely analogous to the three dimensional particle in a box model.

Simple effective mass approximation (EMA) theory was first used to solve the electron wave function. EMA theory solves the Schrödinger Equation with an isolated electron and an isolated hole in a sphere assuming the infinite barriers, parabolic bands, and the bulk effective masses of carriers. The density of states therefore resembles the bulk parabolic band structure, but electrons and holes have quantized states expressed as their effective masses, m_e and m_h, and the radius R. This explains the increase of the bandgap as size decreases.[Figure 1.3 (A)]

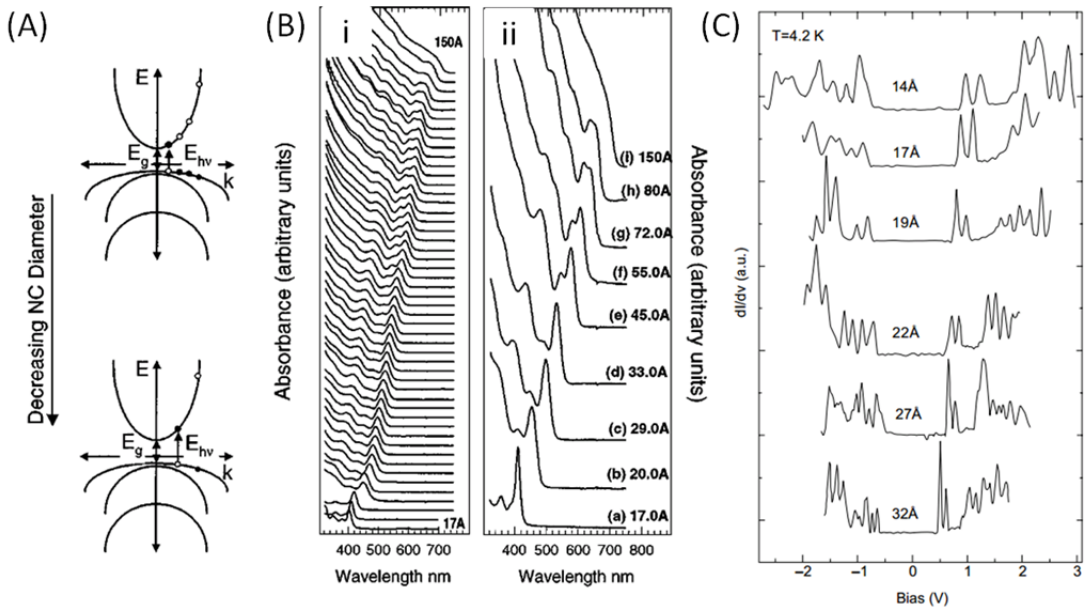

Figure 1.3 (A) Simple effective mass approximation to build a parabolic energy diagram (E vs k) of conduction and valence bands of a semiconductor.[5] The confinement of NC quantizes the allowed k values. Decreasing the NC diameter shifts the first state to larger values of k and increase the separation between each state.[Adapted from reference 5] (B) i. absorption spectrum of CdSe NCs at r.t. As size decreases, a greater blue shift in the absorption edge and a larger separation between electronic transitions occur. ii. The discrete electronic transitions in optical absorption [Adapted from reference 5] (C) Scanning Tunneling Spectroscopy of the different size of InAs NCs.[6] Representative tunnelling dI/dV versus V characteristics of different size of NCs shows the evolution of discrete electronic states.[Adapted from reference 6]

However, EMA frequently overestimates the effective bandgap of NCs. One of the reasons is that EMA does not consider the interaction between electron and holes. Brus et al.[7] first consider the interaction between electrons and holes, or Coulomb attraction, and find it to be proportional to $1/R^2$, where R is the diameter of the NC. Perturbation theory is used to simply add the 1/R potential energy, which is described as

$$E_{g,NC} = E_{g,bulk} + \frac{h^2\alpha^2}{8R^2}\left(\frac{1}{m_e} + \frac{1}{m_h}\right) - \frac{1.8e^2}{4\pi\epsilon_0\epsilon R}$$

The second term in the right side describes the confinement of the exciton, and the third term represents the Coulomb attraction.

More realistic models[8] have been developed using a finite potential instead of an infinite one,[9,10] or using a hyperbolic model,[11] (use non-parabolic band structure instead of parabolic one) or other approaches, such as k.p model,[12] and the tight binding model,[13] which give better agreement with the experimental results. In experiments, absorption data is commonly used to investigate the optical band gap. Scanning tunneling microscopy is also used to probe the electronic band structure.[6,14] Both measurements successfully show the size-dependent energy states in CdSe[5] NCs [Figure 1 (B)] and InAs NCs,[6] [Figure 1 (C)] and other NCs.

While such computational models are well developed, there are limitations to predicting the exact electronic band structures. One of the big challenges is to consider surface effects,[15] such as dangling bonds or chemical binding ligands that exist in most of the NCs synthesized by colloidal chemistry. Currently there are many efforts to consider

the actual surface states. However, in reality, there are too many variations on NC surfaces, including the different surface defect states, trap states and various ligands that can either passivate or generate the trap states or other new states.

It should be noted here that NCs have extremely high surface-to-volume ratio compared to bulk.[16] This frequently causes a problem in the real application as the surface usually consists of dangling bonds or unpassivated sites acting as surface trap or defect states.[17,18] However, careful control of the surface can be used to modify materials properties advantageously. For example, conventional semiconductors such as silicon need expensive, high energy tools to accomplish doping. One method is ion implantation, wherein dopants are accelerated at high field into the surface of silicon such that they diffuse into the bulk. However in NCs, simple chemical treatments that modify the surface can be taken advantage of to dope the NCs. For example, dipping the NCs or NC device into chemical agents can change the surface states, and this means that the number of carriers, and therefore electronic properties can be readily engineered through remote doping.[17,19–22]

1.2 Bulk and nanoscale lead chalcogenide semiconductors

Lead chalcogenides (PbS, PbSe, PbTe) have been extensively studied since the 1950s due to their unique and useful properties, especially for thermoelectric and optoelectronic technologies. They have a small bandgap, low thermal conductivity, high mobility, high static permittivity and small and similar electron and hole effective mass,

etc.[23] The low thermal conductivity, high electrical mobility and conductivity make lead chalcogenide, especially PbTe, one of the best thermoelectric materials, and resulting in a high Seebeck coefficient.[24,25] The small bandgap of ~0.2eV enables the absorption and detection of infrared signal. Combined with its high sensitivity and fast response, lead chalcogenide enabled a major advance in infrared technology. Currently PbS detectors are one of the most common commercial detectors for the near-mid infrared (IR) range.[26] Lead chalcogenides are unique in that they have a positive temperature-bandgap coefficient, and therefore when they are cooled even lower energies can be detected, covering a huge spectral range.[23] At liquid helium temperatures, PbSe is sensitive to IR radiation with wavelengths up to 9um.[26] In addition, when cooled down to liquid nitrogen or helium temperatures, the mobility increases to a very high value of up to $10^6 cm^2/Vs$, mostly due to a decrease in scattering.[27] The high mobility at room and low temperature and unique properties come from a high static permittivity that effectively screens the coulomb potential allowing transport of carriers to mostly ignore scattering due to charged impurities, even with high carrier density.[26] All three lead chalcogenides show very similar characteristics.[28,29]

Lead chalcogenide nanostructures have attracted even more attention both in scientific research and technological applications. First, out of all nanostructured materials, this material exhibits the strongest quantum confinement effect.[30] As lead chalcogenides have very small and similar electron and hole effective masses, these materials have one of the largest Bohr exciton radii, as determined by the following expression[2]

$$a_B = \frac{4\pi\hbar^2}{m_e e^2}$$

They have very large and similar Bohr electron and hole radius, and have symmetric and similar electron and hole structure.[29] The electronic and optical properties of lead chalcogenide NCs change as their size is reduced, especially in the strong quantum confinement regime ($R \ll a_B$).[8] For small Bohr radius materials, the strong quantum confinement effect starts to show around <1nm, which is difficult to fabricate or synthesize. However, for lead chalcogenide, the strong confinement regime can be achieved around r=1-3nm, a size regime which can be readily synthesized.[31–33] Due to this large Bohr radius and easily accessed and well developed fabrication methods, there is great interest in the fundamental physics of these materials.

Second, quantum confinement effects can be utilized to design lead chalcogenide NC devices.[21,34] Quantum confinement allows the band gap to be tunable, and therefore photodetective applications can be extended from the mid-IR region of the spectrum to the near IR and even visible.[31,32] The tunable bandgap also makes lead chalcogenide NCs attractive candidates for electronic applications.[20,35,36] For instance, transistors require *on* and *off* states or high and low conductivity, respectively. The small bandgap and relatively large carrier densities of bulk lead chalcogenides are not desirable as it is difficult to turn the device *off*. However, the large and tunable bandgap of lead chalcogenide NCs is more favorable to controlling the current or transistor state.

The tunable bandgap is also a big advantage for solar cell application as they can match the wide range of wavelength in the solar spectrum.[31,37,38] As was stated, due to

large Bohr radius, the band gap of PbSe can be changed from 0.26 to 0.7 to 1.6eV when the size of NCs changes from bulk to 6nm to 2.5nm, respectively. Moreover, due to high permittivity, the coulomb screening results in a low excitonic binding energy. This indicates that, in lead chalcogenides, the exciton created upon illumination can much more easily separate and contribute to the photo-current in a p-n junction than the exciton in low dielectric constant materials or organic materials. Furthermore, recent reports show that this material can be exploited for multiple exciton generation.[39–41]

Compared to other NCs, lead chalcogenide NCs have important characteristics for device applications. Due to the larger Bohr radius, the electronic wavefunction readily leaks out of the barrier of the NC.[20] This results in a high coupling energy, allowing charge carriers to move from one NC to the next NC easily, when two NCs are close together.[17,20,42–45] Typically, NC devices consists of NC thin films of thousands of NCs. If the coupling energy is small, NC thin films will be insulators. Therefore, a high coupling energy to increase and control the conductivity is one of the key parameters for a high performance device.

In addition to their favorable fundamental properties, colloidal NCs are solution processable, rendering them a great candidate for low cost and high performance device applications.[17,21,46] Owing to these advantages, over the decades, researchers have put much effort into integrating lead chalcogenide NCs into electronic, thermoelectronic, and optoelectronic devices, and great advances and outcomes have resulted.

1.3 Synthesis of NCs and lead chalcogenide NCs

There are typically two approaches to fabricate nanomaterials : top-down and bottom-up.[16] Top down methods include milling or etching the bulk material until desirable nano-sized materials are achieved. Such processes, however, often create imperfect surfaces when materials are cut into nanostructures. Bottom up methods involve building up the materials atom by atom. The most common technique for nano and microscale fabrication is lithography, which can use either or both of the top down and bottom up methods. For example, photolithography or electron-beam lithography is first used to make a pattern, and the material is etched (top-down) or deposited (bottom-up). Photolithography is commonly used for micron-scale structure but it is difficult to use to achieve nanoscale features. Electron-beam lithography provides a precise control even for nano-size materials[47] and a great opportunity to understand the physical properties of nanoscale semiconductors.[48,49] However, it has a technical and practical limit for nanostructure fabrication as it is time-consuming and very expensive.

Colloidal synthesis, one of the bottom-up methods, is a chemical method to synthesize NCs. It is a low-cost and low-temperature process, and emerges as the most promising technique to fabricate NCs.[5,50] Colloidal synthesis mostly consists of the homogeneous nucleation and subsequent growth of the species.[16] These are thermodynamically well explained and developed. Nucleation occurs when the concentration of precursors exceeds the critical concentration of the solution, or supersaturation, which possesses a high Gibbs free energy. This high Gibbs free energy makes the system unstable, but can be reduced by segregating the solute from solution

and forming a new solid phase. This reduction of Gibbs energy is the driving force for nucleation and growth. The change of Gibbs free energy per unit volume is described as[16]

$$\Delta G_v = -k_B T/V \ln(C/C_0)$$

where T is temperature, k_B is Boltzmann constant, V is atomic volume, C is the concentration of solute in solution, and C_0 is solubility. As seen in the equation, nucleation cannot occur if $C<C_0$.

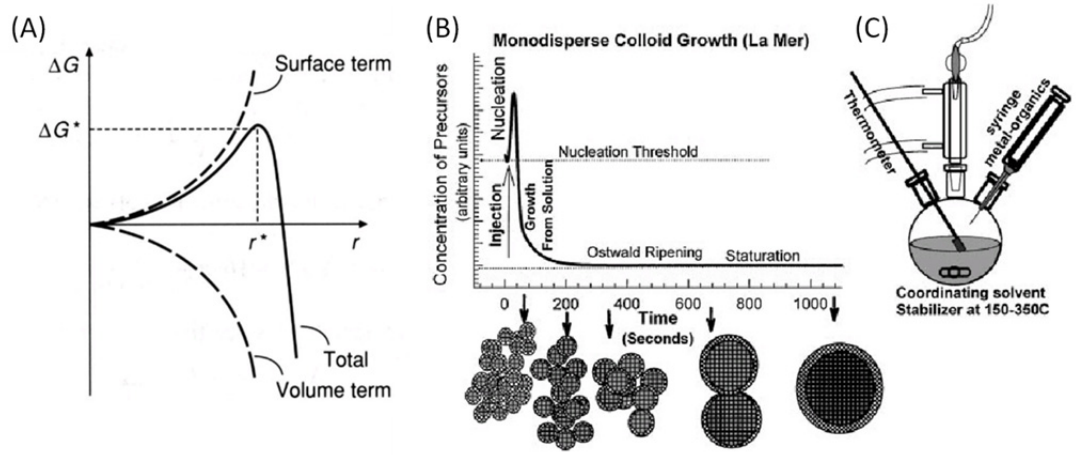

Figure 1.4 (A) The change of volume energy, surface energy, and total free energy, as functions of nucleus' radius.[16] [Adapted from Reference 16] (B) Schematic of the nucleation and growth of NCs as a function of time (La Mer model).[5] (C) Schematic of the experimental setup to synthesize monodisperse NCs. [Adapted from Reference 5]

As nucleation occurs, the surface energy of the nucleated solid increases, which will increase the Gibbs free energy, against to the nucleation driving force. The total change of free energy [Figure 1.4 (A)] is then,[16]

$$\Delta G=\Delta\mu_v+\Delta\mu_s = 4/3\pi r^3\Delta G_v + 4\pi r^2\gamma$$

The first term on the right side represents the volume energy assuming spherical NCs, and second term represents the increase in energy due to nucleation on the surface.

Even if the concentration of precursors is slightly larger than the solubility, nucleation will not occur effectively due to the surface energy unless they have a critical energy or specific size to overcome this. This critical energy and size can be extracted from the condition $d\Delta G/dr=0$, and calculated as $r^*=-2\gamma/\Delta Gv$ and $\Delta G^*=16\pi\gamma/3(\Delta G_v)_2$.[16] If r is smaller than r* the nucleus will dissolve into the solution to reduce the overall energy, and only when r>r* will the nucleus be stable and continue to grow. The critical radius, r*, decides the smallest size of a stable nucleus.[16] In an actual reaction, variable parameters such as concentration, temperature, type of solvents, and precursors are used to achieve the desirable shape and size.

As nucleation proceeds, the concentration of precursors drops quickly and becomes smaller than the critical concentration, causing nucleation to stop [Figure 1.4 (B)]. The remaining precursors contribute to NC growth. When there is a sufficient amount of precursors, smaller NCs grow faster than larger ones; this is known as the size focusing stage.[5] When the precursors are depleted, Ostwald ripening occurs.[5,16] During this process, the small species with high surface energy will be dissolved. The

decomposition of smaller NCs will promote the growth of larger NCs by supplying the materials. This process increases monodispersity in the NC synthesis and is therefore an important step for the reaction.

For the formation of uniform size NCs, it is important to control the system such that all nuclei form at the same time and with the similar size. Pioneered by Murray et al.,[51] the simple wet chemical method called hot injection method was developed to synthesize monodisperse nanocrystals. In this method, the precursors are quickly injected to cause a burst nucleation to begin everywhere uniformly. Figure 1.4 (C) describes the hot injection method for NC synthesis via nucleation followed by growth and Ostwald ripening. In this experimental method, there is another reaction parameter, namely the ligands. These organic ligands cap the NCs during the NC growth, and have several roles.[5,50,52] First, they stabilize NCs to mediate and slow down the growth. They further prevent aggregation and precipitation of NCs by creating steric hindrance and reducing the van der Waals force between NCs. Last, they electronically stabilize and passivate the NC surfaces by eliminating the surface dangling bonds and defect states.

The PbSe NC synthesis is based on the hot injection method wherein Pb precursors are injected into a hot solution containing Se precursors to nucleate and grow NCs. The growth of NCs is stopped by cooling down the system when the desirable size is reached. A typical procedure for 6nm PbSe NCs is as follows.[35,53]

A solution of 892 mg lead oxide (PbO), 3 mL of oleic acid, and 20 mL of octadecene (ODE) was heated to 120 °C and degassed for 1 hour under vacuum. The

temperature was then raised to 180 °C, at which point 8 mL of the Se precursor (1M tri-n-octylphosphine(TOP):Se and 60 μL of diphenylphophine (DPP)) was rapidly injected into the hot solution. After 80 sec of reaction time, the solution was rapidly cooled down to room temperature using an ice bath.

By varying the reaction temperature, time, precursors, and solution, different sizes of PbSe NCs [31,32] and PbS NCs[33,54,55] as well as PbSe nanorods[56,57] and nanowires[58,59] can be synthesized.

1.4. Shape and structures of lead selenide NCs

Three lead chalcogenides have very similar electronic structures and structural properties. As lead chalcogenide NCs also resemble each other, the properties of PbSe NCs will be representatively introduced here.

6nm PbSe NCs, the most extensively studied for the charge transport due to the optimal electronic characteristics, are synthesized by the method described in Chapter 1.3. They have a band gap of ~0.67eV as shown in absorption measurement [Figure 1.5 (B)]. Oleic acids are surrounding the NCs, as seen in Fourier Transformation InfraRed (FTIR) spectroscopy [Figure 1.5 (C)]. Generally NCs are assumed to be spherical, but in reality, they do have multiple facets. 6nm PbSe NCs are truncated octahedral shape, but the different sizes of NCs have different shapes with more preferential facets.[58,60–63] The structure and the facets are determined by the surface energy and the properties of bulk crystalline structure.

Bulk lead selenide is a cubic crystal of NaCl structure, and space group of FM-3M (No. 225) with 192 operators.[23,26] Lead is positioned at (0,0,0), (0,0.5,0.5), (0.5,0,0.5) ,(0.5,0.5,0) and selenium is positioned at (0,0,0.5), (0,0.5,0), (0.5,0,0), (0.5,0.5,0.5). One lead and one selenium atom together is regarded as one motif, and therefore it is considered to be a face centered cubic structure.

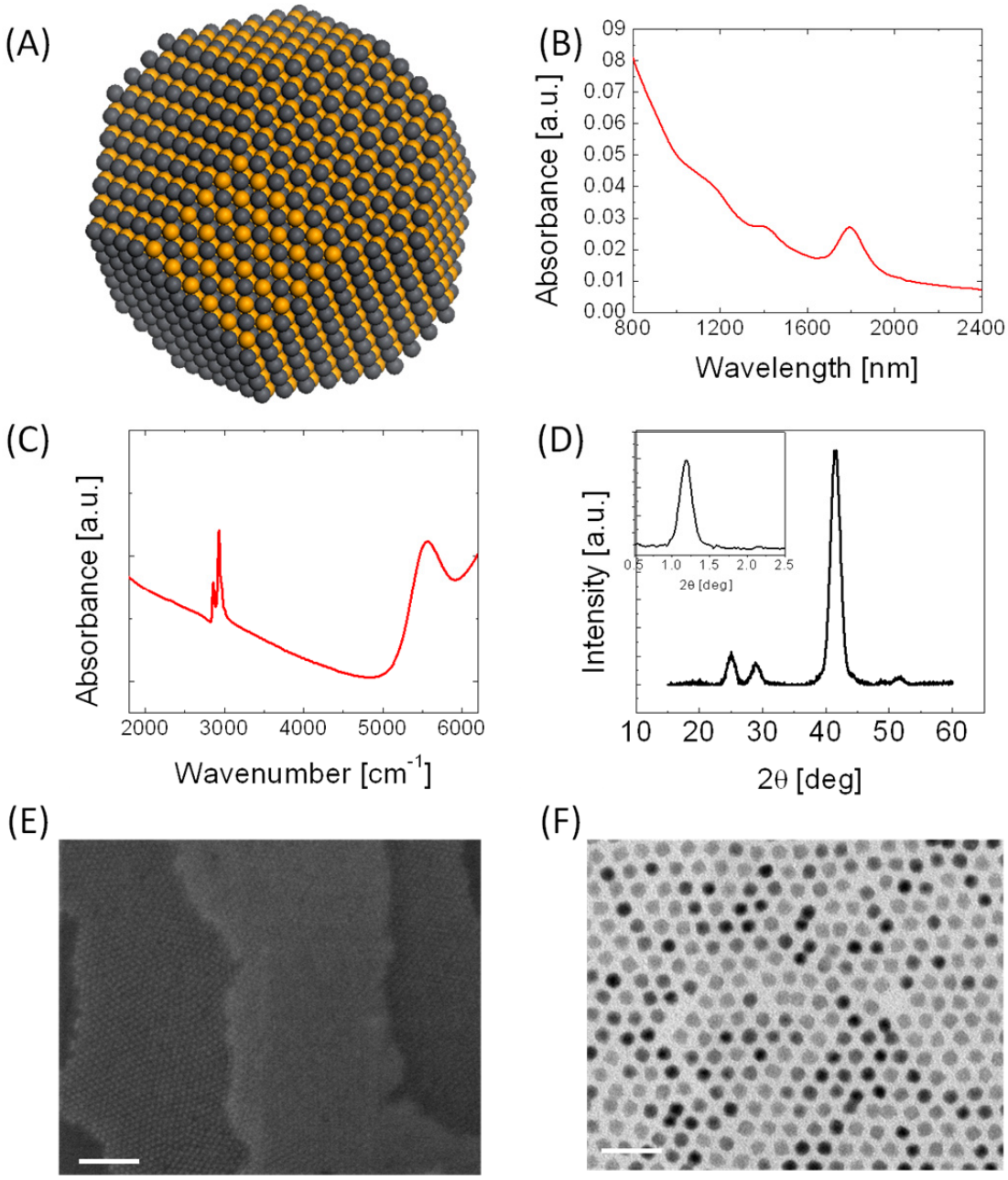

Figure 1.5 (A) Schematic of 6nm PbSe NCs. (B)Absorption spectroscopy, (C) Fourier Transform Infra-Red spectroscopy, (D) wide angle and (inset) small angle X-ray Diffraction pattern, (E) scanning electron microscopy, and (F) transmission electron microscopy of 6nm PbSe NCs. (scale bar : (E) 100nm, (F) 25nm)[35]

PbSe NCs therefore have an fcc structure, as shown in XRD pattern [Figure 1.4 (D)]. The peak of {111}, {200}, {220}, and {222} are shown from left to right [Figure 1.4 (D)]. The different facets of the crystal have different surface energies. Lead selenide NCs mostly show {111} surfaces and {100} surfaces, but depending on the size they can show {110} or other facets. As lead selenide NCs are FCC structured, {100} facets are stoichiometric but {111} facets can only terminate in lead or selenium, not both. When NCs are synthesized, they tend to have the most stable facets. Theoretical calculations using density functional theory (DFT) show that {111} surfaces are extremely unstable. Researchers argue that {111} facets can exist only when the surfaces are reconstructed in a way that {111} facets become stoichiometric by either gaining or losing atoms.[62,63] However, recent progress with DFT calculation shows that the high surface energy of {111} facets can be greatly reduced by oleic acid binding.[61] When oleic acids bind to {111} facets in oleate form, the facets become stable and have a low surface energy.[61,64,65] As {100} surfaces are stable, they do not need to have any stabilizing ligands, and therefore oleic acid binds to them very weakly. In other words, oleic acid can be detached from {100} facets easily while it is hard to detach the ligands from the {110} surfaces.

Lead selenide NCs in the 4-8nm range tend to have a truncated octahedral structure, and therefore have both {111} facets stabilized by oleic acid and {100} facets. Small NCs in the 2-3nm range are reported to show octahedron structure which has more {111} facets. This stabilizes the overall surface energy, which otherwise will be very

high for small NCs. As {111} facets are Pb-rich, small NCs have a higher Pb:Se ratio than larger NCs.

Lead selenide NCs always shows a Pb:Se ratio greater than 1. Initially researchers thought that all the surfaces were covered with only lead atoms.[66,67] Recently, new models that meet the experimental results have been proposed.[61] {100} terminated facets have stoichiometric surfaces and weakly bind with oleic acid. {111} terminated facets terminate with Pb atoms which bind with two oleate molecules, balancing the charges. However, more detailed experimental and theoretical work is needed for complete understanding of lead chalcogenide structures.

SEM and TEM image of 6nm PbSe NCs are shown in Figure 1.5 (E,F).

1.5 Charge transport in semiconductors and NC thin film devices

1.5.1 Developments of NC thin films

As-synthesized NCs have high crystallinity and stable structural properties as they are capped by surface ligands. However the long and insulating surface ligands are unfavorable when NCs are integrated to the device. For the device application, NCs are spincasted onto substrates to form a thin film. The long interparticle distance due to long ligands prevent transport of any charge carriers from one NC to other NC. There have been many efforts to replace the long original ligands with shorter ones to allow electronic communication between two NCs. One way to exchange the ligand is to

immerse the NC thin film into the solution containing shorter ligands. Researchers successfully exchange the original long ligands to shorter organic ligands such as pyridine,[68,69] butylamine,[70,71] or even shorter one, ethanedithiol,[72,73] benzenedithiol,[31,74] mercapto propionic acid,[75] hydrazine.[20,76] Later, even more shorter inorganic ligands are developed, such as Merween's salt, Molecular Metal Chalcogenide (MMC)[77,78] ($(Sn_2Se_6)^{4-}$, $(In_2Se_4)^-$,) thiocynate $(SCN)^-$,[35,79–81] chalcogenide[36,82] (selenide, Se^{2-}, sulfide, S^{2-}), halogenide[19,83,84] (bromide, Br^-, chloride, Cl^-, Iodide, I^-,). These findings enhance the electrical conductivity and mobility of NC thin films greatly, and achieve the successful device fabrication of transistor, photodetector, and solar cells.

1.5.2 Charge transport in semiconductors

The common and most important physics of these device applications is the charge transport. It is crucial to understand the device physics to successfully adapt the NCs into these devices, and the concept of charge transport will be briefly reviewed in section.

As discussed, current flow in a semiconductor is governed by the movement of electrons that have energy higher than E_F. In a typical two electrode device, charges should be first injected from one electrode to the semiconductor. Then charge will flow through the semiconductor with various scattering or other mechanism and reach the other metal, contributing to the current. We can separate the charge injection and transport mechanism for the total current flow.

When metal-semiconductor junction shows Ohmic contact with negligible barriers, charge can easily be injected from the metal to semiconductor without any further energy needed. When the junction is a Schottky contact with a significant barrier, charges need to overcome this Schottky barrier(SB) ,Φ_{SB},through thermal emission or field emission with assistance of heat or electric field. In thermal emission, the amount of electron injection, or injection current, is proportional to the number of electrons that have higher energy than the SB, described as[85]

$$I \propto \exp[-q\phi_{SB}/nk_BT]$$

where n is ideality factor. While the thermionic emission is temperature dependent, the field emission by tunneling is a temperature independent mechanism, and is described as[85]

$$I \propto V^2\exp[-b/V]$$

where V is a voltage and b is constant. Once the charge carriers pass the metal semiconductor interface, the transport of charge is determined by the semiconductor.

In single crystalline semiconductors, the electron movement is limited by either phonon scattering or ionized impurity scattering. The mobility or lifetime of electron is then typically governed by or expressed by Mathiessen's rule.[86]

$$\frac{1}{\mu} = \frac{1}{\mu_{ph}} + \frac{1}{\mu_{im}}$$

where μ_{ph} is phonon scattering limited mobility and μ_{im} is impurity scattering limited mobility.

In polycrystalline materials, the effective mobility can be expressed as the mobility in the grain and at the grain boundary.[1]

$$\frac{1}{\mu} = \frac{1}{\mu_g} + \frac{1}{\mu_{gb}}$$

where μ_g is the mobility in the grain and μ_{gb} is the mobility at the grain broundary. In most cases (g>>gb, otherwise amorphous semiconductor), the limiting process for the charge transport occurs at the grain boundary between adjacent crystalline grain, rather than the impurity or phonon scattering in each crystalline grain. The transport at the grain boundary is understood as the barriers between two grains, $\Phi_{B,}$ and thus can be similarly expressed as thermionic emission using Φ_B instead of Φ_{SB}, at high temperature, and tunneling at the low temperature.

In amorphous semiconductor or organic semiconductor where strong disorder exists, the transport is mostly governed by a hopping mechanism : a few exception exists, such as extended mini band, or band-like transport. There are many models to understand this type of charge transport physics, including the multiple trap release model and variable hopping model, etc.

1.5.3 Charge transport in NC thin films

Charge transport in NC films is typically conceptualized by analogy with disordered systems.[17] To describe the charge transport behaviors in NC thin films, three important concepts will be introduced.

a. The charging energy. When an electron moves from one NC to other NCs, it requires energy to remove the electron from one NC, and to add one electron to the other NC. In bulk, these two energies are the same as the work function.[87] In molecules, they are different and described as ionization potential (IP) and electron affinity (EA).[87] NCs are in between bulk and molecules. The difference between IP and EA is called charging energy, Ec, and described as,[17]

$$E_c = e^2/C$$

$$C = 4\pi\varepsilon_0\varepsilon_m r$$

where C is the capacitance of NCs, r is the radius of NCs, ε_o is the vacuum permittivity and ε_m is the permittivity of the surrounding medium. For an electron transfer, an electron has to be removed from one NC and added to another NC; therefore the energy of twice of E_c ($E=2E_c$) should be overcome.

b. The exchange coupling energy. As described, the carriers are confined in the NC, and the wavefunction exponentially decays outside of the NC. However, when two NCs become significantly closer, the leakage of wave function starts to overlap. This enables the charge transfer from one NC to other NCs. Therefore the coupling energy is a function of interparticle distance and barrier height, described as

$$\beta = h\,\Gamma = h\,e^{\left(-\left(2m^*\Delta E/\hbar^2\right)^{0.5}\Delta x\right)}$$

where Γ is the tunneling rate between two NCs, m* is the effective mass, ΔE is the barrier height, and Δx is the interparticle distance.

c. The disorder energy. There are two different origins for the disorders, the energy disorder and structural disorders. Since as-synthesized NCs are not 100% the same size, this will cause variation in the bandgap. The conduction and valence band edge will be located at different position in different NCs, resulting in the barrier. Charge carriers need additional energy to overcome this barrier. The other disorder, structural disorder, comes from NC packing structures. Unlike single crystalline materials, the randomly arrayed and positioned NCs do not have periodicity, and the Bloch theorem fails to hold. As a result, the continuous mini band (Bloch-like extended wave function) cannot be formed.

In weakly coupled NC thin films, $\beta < k_B T$, electron transfer only occurs via tunneling. In this regime, and at sufficiently low temperature $k_B T < Ec$, the charging energy creates the Coulomb gap ($E=2E_c$). At sufficiently high voltage, the charging energy can be overcome, and electrons can tunnel through NC thin films. However, at near zero bias (below threshold voltage, $V \ll V_{th}$), the conductance is significantly suppressed as carriers do not have sufficient energy to overcome the charging energy. Here, the conductance is described as $I=(V-V_{th})^a-1$, where a is constant.

In strongly coupled NC thin films, $\beta \gg k_B T$, delocalized states exist and efficient charge transport occurs. If the exchange coupling energy is high enough to dominate both the disorder energies and charging energy ($\beta > Ec$), the Coulomb gap disappears, and carriers can transport freely through the mini band. Therefore, high mobility, or Bloch carrier mobility, would be achieved.

So far, there are few cases that show strongly coupled NC solids. Most semiconducting NC solids are considered as disordered systems such as amorphous semiconductors. The charge transport in a disordered system is limited and mostly expressed as the carrier movement through hopping, with an Arrhenius-like temperature dependence.[88]

$$\sigma = \sigma_0 exp[-\mathrm{E_a}/\mathrm{k_B T}]$$

where E_a is the activation energy

However, depending on the temperature, a different hopping or tunneling transport will govern the system. While at high temperature thermal activated hopping dominates, at moderately high temperature, nearest neighbor hopping is the primary mode of electron transport. In this case, thermal energy, k_BT is high enough to excite the electron to hop to nearest neighbor sites by overcoming the barrier. As temperature decreases, there is not enough thermal energy to overcome this, and variable hopping mechanism dominates the transport mechanism. In this case, the carrier can only hop to further sites within a small energy difference at low K or same energy at 0K. This is expressed as Mott VRH or ES-VRH, respectively. As a function of T, the hopping mechanism can be expressed as:

$$\sigma = \sigma_0 exp\left[-\left(\frac{\mathrm{T_0}}{\mathrm{T}}\right)^{\mathrm{n}}\right]$$

with n=1 for thermal activated hopping or nearest neighbor hopping, ½ for ES variable range hopping, ¼ for Mott variable range hopping.[88–92]

1.5.4 Characterization of charge transport

The transport characteristics can be extensively investigated not only by conductivity measurement with two electrodes geometry, but also by a more complicated measurement with 2-, 3-, or 4- electrodes.

Two-electrode measurements under illumination, probe photoconductive transport characteristics can be studied. Under illumination, charge carriers will be excited, and excitons will be separated either by internal built-in potential for p-n junction or other solar cell, or by external voltage for photoconductive detector. In this case, useful photoconductive properties such as lifetime, mobility, responsivity and sensitivity can be studied.

As a three terminal measurement, the field effect transistor (FET) structure, there is an additional gate electrode and dielectric layer that can electronically change the semiconductor properties. Fermi level can be shifted down or up depending on the voltage, and electron and hole can become accumulated, depleted or inverted in the channel. With this FET geometry, the field effective characteristics including FET mobility, subthreshold voltage, and swing can be examined.

The system can be further characterized using a four electrode measurement. Here, useful information such as sheet resistivity can be extracted. By magnetic field, Hall effect characteristics such as Hall mobility, carrier concentration, and resistivity can be extensively studied.

With an additional parameter, temperature, the charge injection and charge transport characteristics can be extensively studied. These measurements allow us to understand the intrinsic properties of NC thin films, and help to provide insightful ideas to manipulate and engineer the properties.

1.6 Thesis overview

The thesis focuses on 1) characterization tools to investigate the physical properties of charge carrires, 2) the novel methods to engineer the carrier statistics and electronic properties in nanoscale materials, and 3) designing low cost, high performance nanomaterials optoelectronics and electronic device.

Chapter 2 introduces a unique method to control the electronic properties of NCs. The effect of stoichiometric imbalance in lead chalcogenide NC thin films is examined to control the carrier statistics by introducing excess lead (Pb) or selenium (Se) through thermal evaporation.

Chapter 3 introduces a simple and solution-based method to control the surface stoichiometry and therefore the electronic properties of NCs to design a low-cost and high performance NC device.

In Chapter 4, the fundamental physics of charge injection and transport in NC thin films device is investigated. This study emphasizes the important role of charge injection between metal and semiconductor in high performance NC device.

In Chapter 5, the charge injection and transport in ambipolar and unipolar single, strongly quantum confined PbSe NW FETs is investigated. This work highlights the remote doping process, a promising route to dope nanostructures, in contrast to the commonly used substitutional doping process.

In Chapter 6, the progress of CdSe NC thin film devices is introduced. This work shows the high performance, large area, air-stable and flexible CdSe NC thin film electronic and optoelectronic devices achived by the strong electronic coupling and In doping.

Chapter 7 introduces a novel technique to characterize the electronic and optoelectronic properties of semiconductor devices. Using the correlated scanning photocurrent microscope and scanning confocal photoluminescence measurement, the physics of photoexcited charge carriers in organic solar cells is investigated.

Chapter 8 introduces future works to design high performance electronic and optoelectronic NC devices and concludes this thesis work.

1.7 References

(1) Calister, W. D.. *Materials Science and Engineering: An Introduction*; 6th edition.; John Wiley and Sons, 2002

(2) Kittel, C. *Introduction to solid state physics*; 8th edition.; Wiley.

(3) Alivisatos, A. P. *Science* **1996**, *271*, 933–937.

(4) Murphy, C.; Coffer, J. *Appl. Spectrosc.* **2002**, *56*, 16.

(5) Murray, C.; Kagan, C.; Bawendi, M. G. *Annu. Rev. Mater. Sci.* **2000**, *30*, 545–610.

(6) Banin, U.; Cao, Y.; Katz, D.; Millo, O. *Nature* **1999**, *400*, 5–7.

(7) Brus, L. E. *J. Chem. Phys.* **1984**, *80*, 4403.

(8) Efros, A.; Rosen, M. *Annu. Rev. Mater. Sci.* **2000**, 475–521.

(9) Nanda, K.; Kruis, F.; Fissan, H. *Nano Lett.* **2001**, *1*, 605–611.

(10) Kayanuma, Y.; Momiji, H. *Phys. Rev. B. Condens. Matter* **1990**, *41*, 261–263.

(11) Wang, Y.; et al. *J. Chem. Phys.* **1987**, *87*, 7315–7322.

(12) Fu, H.; Wang, L.; Zunger, A. *Phys. Rev. B* **1998**, *57*, 9971–9987.

(13) Lippens, P.; Lannoo, M. *Phys. Rev. B* **1989**, *39*, 10935.

(14) Liljeroth, P.; van Emmichoven, P.; Hickey, S.; Weller, H.; Grandidier, B.; Allan, G.; Vanmaekelbergh, D. *Phys. Rev. Lett.* **2005**, *95*, 086801.

(15) Kim, D.; Kim, D.-H.; Lee, J.-H.; Grossman, J. C. *Phys. Rev. Lett.* **2013**, *110*, 196802.

(16) Cao, G. *Nanostructures & Nanomaterials*; Imperial College Press, 2004.

(17) Talapin, D. V; Lee, J.-S.; Kovalenko, M. V; Shevchenko, E. V. *Chem. Rev.* **2010**, *110*, 389–458.

(18) Kramer, I.; et al.*ACS Nano* **2011**, 8506–8514.

(19) Ning, Z.; Ren, Y.; Hoogland, S.; Voznyy, O.; Levina, L.; Stadler, P.; Lan, X.; Zhitomirsky, D.; Sargent, E. H. *Adv. Mater.* **2012**, 1–5.

(20) Talapin, D.; Murray, C. B. *Science* **2005**, *310*, 86–89.

(21) Debnath, R.; Bakr, O.; Sargent, E. H. *Energy Environ. Sci.* **2011**, *4*, 4870.

(22) Oh, S. J.; Kim, D. K.; Kagan, C. R. *ACS Nano* **2012**, *6*, 4328–4334.

(23) Ravich, U. I. *Semiconducting lead chalcogenides*; Plenum Press: New York, 1970.

(24) Snyder, G. J.; et al. *Nat. Mater.* **2008**, *7*, 105–114.

(25) LeSage, B.; Meszaros, G.; Nystrom, T. Nagoya, Japan, 1998; p. 426.

(26) Khokhlov, D. *Lead Chalcogenides physics and applications*; Taylor & Francis, 2003.

(27) Allgaier, R. S.; Scanlon, W. W. *Phys. Rev.* **1958**, *111*, 1029.

(28) An, J. M.; et al. *Nano Lett.* **2006**, *6*, 2728–2735.

(29) Wei, S.-H.; Zunger, A. *Phys. Rev. B* **1997**, *55*, 13605–13610.

(30) Efros, A. L.; Efros, A. L. *Sov. Phys. Semicond.* **1982**, *16*, 772.

(31) Ma, W.; Swisher, S.; Ewers, T.; Engel, J. *ACS Nano* **2011**, *5*, 8140–8147.

(32) Evans, C. M.; Guo, L.; Peterson, J. J.; Maccagnano-Zacher, S.; Krauss, T. D. *Nano Lett.* **2008**, *8*, 2896–2899.

(33) Moreels, I.; Justo, Y.; Geyter, B. De. *ACS Nano* **2011**, 2004–2012.

(34) Tang, J.; Liu, H.; Zhitomirsky, D.; Hoogland, S.; Wang, X.; Furukawa, M.; Levina, L.; Sargent, E. H. *Nano lett.* **2012**, *12*, 4889–4894.

(35) Oh, S. J.; Berry, N. E.; Choi, J.-H.; Gaulding, E. A.; Paik, T.; Hong, S.-H.; Murray, C. B.; Kagan, C. R. *ACS Nano* **2013**, *7*, 2413–2421.

(36) Liu, Y.; Tolentino, J.; Gibbs, M.; Ihly, R.; Perkins, C. L.; Liu, Y.; Crawford, N.; Hemminger, J. C.; Law, M. *Nano Lett.* **2013**, *13*, 1578–1587.

(37) Sargent, E. H. *Nat. Photonics* **2012**, *6*, 133–135.

(38) Ip, A. H.; Thon, S. M.; Hoogland, S.; Voznyy, O.; Zhitomirsky, D.; Debnath, R.; Levina, L.; Rollny, L. R.; Carey, G. H.; Fischer, A.; Kemp, K. W.; Kramer, I. J.;

Ning, Z.; Labelle, A. J.; Chou, K. W.; Amassian, A.; Sargent, E. H. *Nat. Nanotechnol.* **2012**, *7*, 577–582.

(39) Beard, M. C.; Midgett, A. G.; Law, M.; Semonin, O. E.; Ellingson, R. J.; Nozik, A. J. *Nano Lett.* **2009**, *9*, 836–845.

(40) Semonin, O. E.; Luther, J. M.; Choi, S.; Chen, H.-Y.; Gao, J.; Nozik, A. J.; Beard, M. C. *Science* **2011**, *334*, 1530–1533.

(41) Sukhovatkin, V.; Hinds, S.; Brzozowski, L.; Sargent, E. *Science* **2009**, *324*, 1542–1544.

(42) Liljeroth, P.; Overgaag, K.; Urbieta, A.; Grandidier, B.; Hickey, S.; Vanmaekelbergh, D. *Phys. Rev. Lett.* **2006**, *97*, 096803.

(43) Vanmaekelbergh, D.; Liljeroth, P. *Chem. Soc. Rev.* **2005**, *34*, 299–312.

(44) Choi, J. J.; Luria, J.; Hyun, B.-R.; Bartnik, A. C.; Sun, L.; Lim, Y.-F.; Marohn, J. a; Wise, F. W.; Hanrath, T. *Nano Lett.* **2010**, *10*, 1805–1811.

(45) Kagan, C.; Murray, C.; Nirmal, M.; Bawendi, M. *Phys. Rev. Lett.* **1996**, *76*, 1517–1520.

(46) Panthani, M. G.; Korgel, B. a. *Annu. Rev. Chem. Biomol. Eng.* **2012**, *3*, 287–311.

(47) Hu, W. (Walter); Sarveswaran, K.; Lieberman, M.; Bernstein, G. H. *J. Vac. Sci. Technol. B Microelectron. Nanom. Struct.* **2004**, *22*, 1711.

(48) Amlani, I. *Science* **1999**, *284*, 289–291.

(49) Chen, W. *J. Vac. Sci. Technol. B Microelectron. Nanom. Struct.* **1997**, *15*, 1402.

(50) Murray, C.; Sun, S.; Gaschler, W.; Doyle, H.; Betley, T. A.; Kagan, C. R. *IBM J. Res. & Dev.* **2001**, *45*, 47–56.

(51) Murray, C.; Norris, D.; Bawendi, M. *J. Am. Chem. Soc.* **1993**, 8706–8715.

(52) Steigerwald, M. L.; Alivisatos, a. P.; Gibson, J. M.; Harris, T. D.; Kortan, R.; Muller, a. J.; Thayer, a. M.; Duncan, T. M.; Douglass, D. C.; Brus, L. E. *J. Am. Chem. Soc.* **1988**, *110*, 3046–3050.

(53) Yu, W. W.; Falkner, J. C.; Shih, B. S.; Colvin, V. L. *Chem. Mater.* **2004**, *35*, 3318–3322.

(54) Hines, M. a.; Scholes, G. D. *Adv. Mater.* **2003**, *15*, 1844–1849.

(55) Moreels, I.; Lambert, K.; Smeets, D.; De Muynck, D.; Nollet, T.; Martins, J. C.; Vanhaecke, F.; Vantomme, A.; Delerue, C.; Allan, G.; Hens, Z. *ACS Nano* **2009**, *3*, 3023–3030.

(56) Koh, W.; Bartnik, A. C.; Wise, F. W.; Murray, C. B. *J. Am. Chem. Soc.* **2010**, *132*, 3909–3913.

(57) Koh, W.; Yoon, Y.; Murray, C. B. *Chem. Mater.* **2011**.

(58) Cho, K.-S.; Talapin, D. V; Gaschler, W.; Murray, C. B. *J. Am. Chem. Soc.* **2005**, *127*, 7140–7147.

(59) Talapin, D. V.; Black, C. T.; Kagan, C. R.; Shevchenko, E. V.; Afzali, A.; Murray, C. B. *J. Phys. Chem. C* **2007**, *111*, 13244–13249.

(60) Bealing, C. R.; Baumgardner, W. J.; Choi, J. J.; Hanrath, T.; Hennig, R. G. *ACS Nano* **2012**, *6*, 2118–2127.

(61) Argeri, M.; Fraccarollo, A. *J. Phys. Chem. C* **2011**, 11382–11389.

(62) Fang, C.; van Huis, M. a; Vanmaekelbergh, D.; Zandbergen, H. W. *ACS Nano* **2010**, *4*, 211–218.

(63) Schapotschnikow, P.; van Huis, M. a; Zandbergen, H. W.; Vanmaekelbergh, D.; Vlugt, T. J. H. *Nano Lett.* **2010**, *10*, 3966–3971.

(64) Baumgardner, W. J.; Whitham, K.; Hanrath, T. *Nano Lett.* **2013**.

(65) Evers, W. H.; Goris, B.; Bals, S.; Casavola, M.; de Graaf, J.; van Roij, R.; Dijkstra, M.; Vanmaekelbergh, D. *Nano Lett.* **2013**, *13*, 2317–2323.

(66) Moreels, I.; Lambert, K.; Muynck, D. De. *Chem. Mater.* **2007**, *19*, 6101–6106.

(67) Moreels, I.; Fritzinger, B.; Martins, J. C.; Hens, Z. *J. Am. Chem. Soc.* **2008**, *130*, 15081–15086.

(68) Huynh, W. U.; Dittmer, J. J.; Alivisatos, a P. *Science* **2002**, *295*, 2425–2427.

(69) Kim, B. S.; Avila, L.; Brus, L. E.; Herman, I. P. *Appl. Phys. Lett.* **2000**, *76*, 3715.

(70) Oertel, D. C.; Bawendi, M. G.; Arango, A. C.; Bulović, V. *Appl. Phys. Lett.* **2005**, *87*, 213505.

(71) Dissanayake, D. M. N. M.; Hatton, R. a; Lutz, T.; Curry, R. J.; Silva, S. R. P. *Nanotechnology* **2009**, *20*, 245202.

(72) Luther, J. M.; Law, M.; Song, Q.; Perkins, C. L.; Beard, M. C.; Nozik, A. J. *ACS Nano* **2008**, *2*, 271–280.

(73) Luther, J. M.; Law, M.; Beard, M. C.; Song, Q.; Reese, M. O.; Ellingson, R. J.; Nozik, A. J. *Nano Lett.* **2008**, *8*, 3488–3492.

(74) Tang, J.; Brzozowski, L.; Barkhouse, D. A. R.; Wang, X.; Debnath, R.; Wolowiec, R.; Palmiano, E.; Levina, L.; Pattantyus-Abraham, A. G.; Jamakosmanovic, D.; Sargent, E. H. *ACS Nano* **2010**, *4*, 869–878.

(75) Ip, A. H.; Thon, S. M.; Hoogland, S.; Voznyy, O.; Zhitomirsky, D.; Debnath, R.; Levina, L.; Rollny, L. R.; Carey, G. H.; Fischer, A.; Kemp, K. W.; Kramer, I. J.; Ning, Z.; Labelle, A. J.; Chou, K. W.; Amassian, A.; Sargent, E. H. *Nat. Nanotechnol.* **2012**, *7*, 577–582.

(76) Law, M.; Luther, J. M.; Song, Q.; Hughes, B. K.; Perkins, C. L.; Nozik, A. J. *J. Am. Chem. Soc.* **2008**, *130*, 5974–5985.

(77) Kovalenko, M. V; Scheele, M.; Talapin, D. V. *Science* **2009**, *324*, 1417–1420.

(78) Lee, J.; Kovalenko, M.; Huang, J. *Nanotechnol.* **2011**, *6*, 348–352.

(79) Fafarman, A.; Koh, W.; Diroll, B. *J. Am. Chem. Soc.* **2011**, *133*, 15753–15761.

(80) Koh, W.; Saudari, S. R.; Fafarman, A. T.; Kagan, C. R.; Murray, C. B. *Nano Lett.* **2011**, *11*, 4764–4767.

(81) Choi, J.-H.; Fafarman, A. T.; Oh, S. J.; Ko, D.-K.; Kim, D. K.; Diroll, B. T.; Muramoto, S.; Gillen, J. G.; Murray, C. B.; Kagan, C. R. *Nano Lett.* **2012**, *12*, 2631–2638.

(82) Oh, S. J.; Berry, N. E.; Choi, J.-H.; Gaulding, E. A.; Lin, H.; Paik, T.; Diroll, B. T.; Muramoto, S.; Murray, C. B.; Kagan, C. R. *Nano Lett.* **2014**, *14*, 1559–1566.

(83) Zhitomirsky, D.; Furukawa, M.; Tang, J.; Stadler, P.; Hoogland, S.; Voznyy, O.; Liu, H.; Sargent, E. H. *Adv. Mater.* **2012**, 1–5.

(84) Tang, J.; Kemp, K.; Hoogland, S.; Jeong, K. *Nat. Mater.* **2011**, *10*, 765–771.

(85) Rhoderick, E. H. *Metal-Semiconductor Contacts*; 2nd ed.; Claredon Press: Oxford, 1988.

(86) Sze, S. M.; Ng, K. K. *Physics of Semiconductor Devices*; 3rd ed.; John Wiley & Sons: New Jersey, 2007.

(87) Collier, C. P.; Vossmeyer, T.; Heath, J. R. *Annu. Rev. Phys. Chem.* **1998**, *49*, 371–404.

(88) Orton, J. W. *Story of Semiconductors*; Oxford University Press, 2009.

(89) Talapin, D. V; Lee, J.-S.; Kovalenko, M. V; Shevchenko, E. V. *Chem. Rev.* **2010**, *110*, 389–458.

(90) Kang, M. S.; Sahu, A.; Norris, D. J.; Frisbie, C. D. *Nano Lett.* **2011**, *11*, 3887–3892.

(91) Romero, H.; Drndic, M. *Phys. Rev. Lett.* **2005**, *95*, 156801.

(92) Efros, A.; Shklovskii, B. *J. Phys. C Solid State Phys.* **1975**, *49*, 1–4

CHAPTER 2 Stoichiometric Control of Lead Chalcogenide Nanocrystal Solids to Enhance Their Electronic and Optoelectronic Device Performance

This work was published in ACS Nano, entitled "Stoichiometric Control of Lead Chalcogenide Nanocrystal Solids to Enhance Their Electronic and Optoelectronic Device Performance" S. J. Oh, N. E. Berry, J.-H. Choi, E. A. Gaulding, T. Paik, S.-H. Hong, C. B. Murray, and C. R. Kagan, ACS Nano, 2012, 6 (5) 4328.

We investigate the effects of stoichiometric imbalance on the electronic properties of lead chalcogenide nanocrystal films by introducing excess lead (Pb) or selenium (Se) through thermal evaporation. Hall-effect and capacitance-voltage measurements show that the carrier type, concentration, and Fermi level in nanocrystal solids may be precisely controlled through their stoichiometry. By manipulating only the stoichiometry of the nanocrystal solids, we engineer the characteristics of electronic and optoelectronic devices. Lead chalcogenide nanocrystal field-effect transistors (FETs) are fabricated at room temperature to form ambipolar, unipolar n-type, and unipolar p-type semiconducting channels as-prepared and with excess Pb and Se, respectively. Introducing excess Pb forms nanocrystal FETs with electron mobilities of 10 cm^2/Vs, which is an order of magnitude higher than previously reported in lead chalcogenide nanocrystal devices. Adding excess Se to semiconductor nanocrystal solids in PbSe Schottky solar cells, enhances the power conversion efficiency.

2.1 Introduction

Nanocrystals (NCs) of the lead chalcogenides have been shown to be promising candidates for applications in electronics,[1,2] thermoelectrics,[3] and optoelectronics.[4–7] This family of materials has high carrier mobilities, low lattice thermal conductivities, and is infrared absorbing. In the geometry of NCs, the electronic energy levels of this material may be tuned, and upon organization into NC solids the transport of charge and heat can be tailored.[8] They also have the unique ability to switch the polarity of charge transport between ambipolar, n-type and p-type, depending on the chemistry of surface ligating compounds,[1] the presence of surface oxygen,[9] and the surrounding gas.[10] Stoichiometric imbalance is also known to change the polarity of transport in bulk and thin film lead chalcogenides of PbS, PbSe, and PbTe.[11] Pb-rich or X(X=Se, S, Te)-rich PbS,[12] PbSe,[13] and PbTe[14] were shown to become n-type or p-type, respectively. However, little is understood about the effects of stoichiometric imbalance on the electronic behavior of nanoscale lead chalcogenides and its influence on their devices. Stoichiometric imbalance may arise unintentionally during NC synthesis[15,16] or may be introduced intentionally during or after synthesis to manipulate the electronic properties of NC-based electronic materials.

Here, we directly study the effect of stoichiometric imbalance on the polarity of charge transport in PbS and PbSe NC thin film solids and utilize stoichiometric control to design electronic and optoelectronic devices. We tailor the stoichiometry of NC lead chalcogenide thin films by introducing excess Pb and Se through thermal evaporation and transform NC thin film device behavior from ambipolar to n-type and p-type,

respectively [Figure 1A]. Using this method, we fabricate unipolar n-type and p-type lead chalcogenide NC field effect transistors (FETs) with high performance at room temperature. Quantitative analysis is performed by combining FET characteristics with Hall-effect measurements and capacitance-voltage (C-V) measurements. The carrier type, concentration and Fermi level of as-synthesized and ligand-exchanged lead chalcogenide NC films show large variations that originate from unintentional doping during NC synthesis and device fabrication. We show that the carrier statistics can be precisely controlled by stoichiometric imbalance. As NC thin films become Pb-rich, the electron concentration increases and the Fermi level shifts toward the conduction band. As NC thin films become Se-rich, the hole concentration increases and the Fermi level drops toward the valence band [Figure 2.1B]. Finally, we utilize stoichiometric control to engineer carrier type and concentration to optimize PbSe NC Schottky solar cells to realize increased power conversion efficiency.

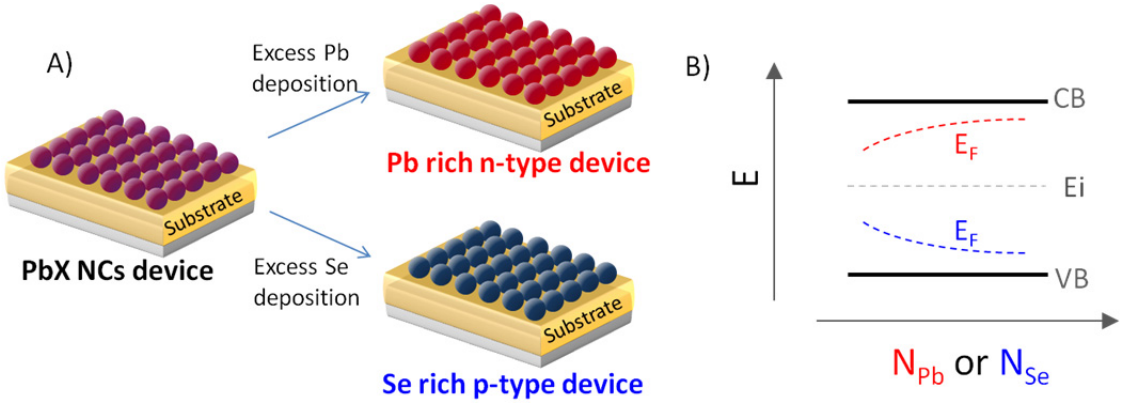

Figure 2.1 (A) Schematic of stoichiometric control of PbX NC thin films by Pb or Se deposition (B) Fermi energy of PbX NCs as a function of the concentration of Pb (red) or Se (blue) atoms added to NC thin films

2.2 Experimental Details

PbX (X=S and Se) NCs capped with oleic acid are deposited by spin-coating to form NC thin film solids on substrates and in device geometries for structural, optical, electrical, and optoelectronic characterization. The long-chain oleic acid ligands capping the NCs, known to be insulating, are exchanged by treating the NC thin films with the compact ligands ammonium thiocyanate (NH_4SCN),[17,18] ethanedithiol (EDT),[9,19–22] hydrazine (N_2H_4),[1,22–24] and benzenedithiol (BDT)[25,26] to decrease interparticle spacing and increase interparticle coupling. For example, in the case of SCN-exchanged PbSe NCs, small angle x-ray scattering shows reduced interparticle distance and optical absorption data shows red shifts and broadening, signatures of enhanced electronic coupling.[18,27] Thermal evaporation of small amounts of Pb (range: 1 to 10 Å) and Se (range: 0.1 to 10 Å) are deposited to introduce a controlled stoichoimetric imbalance in the NC thin films. No significant change in the absorption spectra of the NC thin films is observed upon Pb or Se deposition.

NC FETs are fabricated on heavily n-doped silicon wafers with 250 nm of thermally grown SiO_2 which serve as the back gate and part of the gate dielectric stack, respectively [Figure 2.2A]. Additionally, a 20 nm layer of Al_2O_3 is deposited by atomic layer deposition (ALD) on top of the SiO_2,[28] and the Al_2O_3 surface is derivatized with octadecylphosphonic acid (ODPA) to further reduce hysteresis and complete the dielectric stack.[29] Oleic acid capped PbX NCs are spincoated onto the substrate and soaked in a compact ligand solution. The spincoating and ligand exchange procedure are repeated twice to achieve a film thickness of ~30 nm. 40 nm Au source and drain top

contacts separated by 50 to 150 μm are defined by thermal evaporation through a shadow mask.

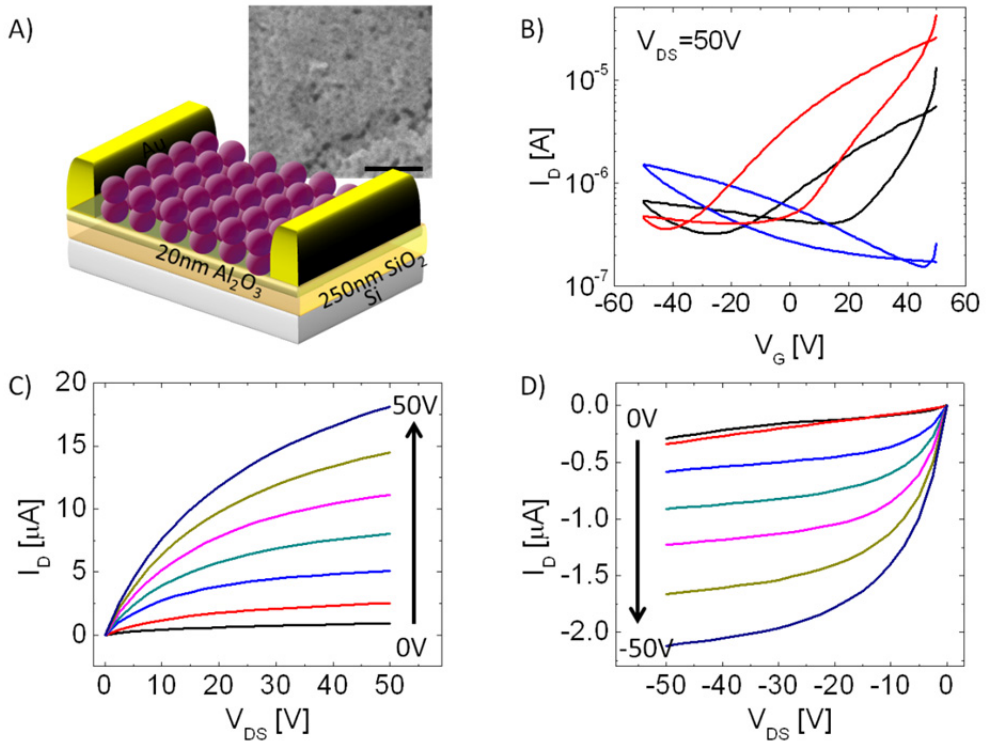

Figure 2.2 (A) Schematic of a PbX NC FET device and (inset) SEM image of a SCN-treated 6 nm PbSe NC thin film solid (scale bar : 100nm), (B) transfer characteristics of (black) as-synthesized and exchanged, (red) 1 Å excess Pb and (blue) 0.1 Å excess Se PbSe NC FETs and output characteristics of the (C) Pb-rich NC FETs with varying V_G from 0V to 50V and (D) Se-rich PbSe NC FETs with varying V_G from 0V to -50V.

2.3 Results and Discussions

2.3.1 Stoichiometric Control of PbSe NCs to Enhance the Electronic Properties

We fabricate as-synthesized, SCN-exchanged PbSe NC FETs which show ambipolar behavior [Figure 2.2B]. This is expected because PbSe has similar electron and hole mobilities,[12] PbX NCs are small bandgap materials providing a small barrier to both electron and hole injection, and the NCs are handled using air-free techniques preventing oxygen exposure which may cause significant p-doping.[10,28] We note that from sample-to-sample predominantly n- or p-type ambipolar behavior may be observed. This can be attributed to a combination of unintentional non-stoichiometry in NC composition, which is known to give rise to slightly Pb-rich PbX NCs[15,16,30] that favor predominantly n-type behavior, and unintentional surface oxygen p-type doping, which occurs even at the <0.1 ppm levels of oxygen in nitrogen filled glove boxes.[10,26,28,31] We denote this unintentional change in carrier concentration by Δn_{un}, and when it is on the order of the intrinsic carrier concentration, where n_e (electron concentration) is equal to n_h (hole concentration), the electron and hole currents and mobilities vary unexpectedly. As-prepared, SCN-exchanged PbSe NC FETs show an electron mobility of 0.02(±0.005) cm^2/V-s in predominantly n-type ambipolar devices and a hole mobility of 0.01(±0.004) cm^2/V-s in predominantly p-type ambipolar devices with I_{ON}/I_{OFF} ~10^2. The electron mobility in predominantly p-type devices and hole mobility in predominantly n-type devices are smaller than 10^{-4} cm^2/V-s.

While an as-prepared FET shows ambipolar characteristics, the transfer characteristics [Figure 2.2B] show that deposition of 1 Å of Pb makes the film n-type in all cases, suppressing the hole current and increasing the electron current and mobility. Similarly, the deposition of 0.2 Å of Se makes the film p-type, decreasing the electron current and enhancing the hole current and mobility. Figure 2.2 (C and D) shows the output characteristics of n-type Pb rich and p-type Se rich PbSe NC FETs, respectively. We conducted control experiments in which 10 Å of Pb and 10 Å Se were deposited between the source and drain electrodes in device structures without NCs and confirmed that these configurations are insulating, showing no current above the 5 pA noise level of the measurement.

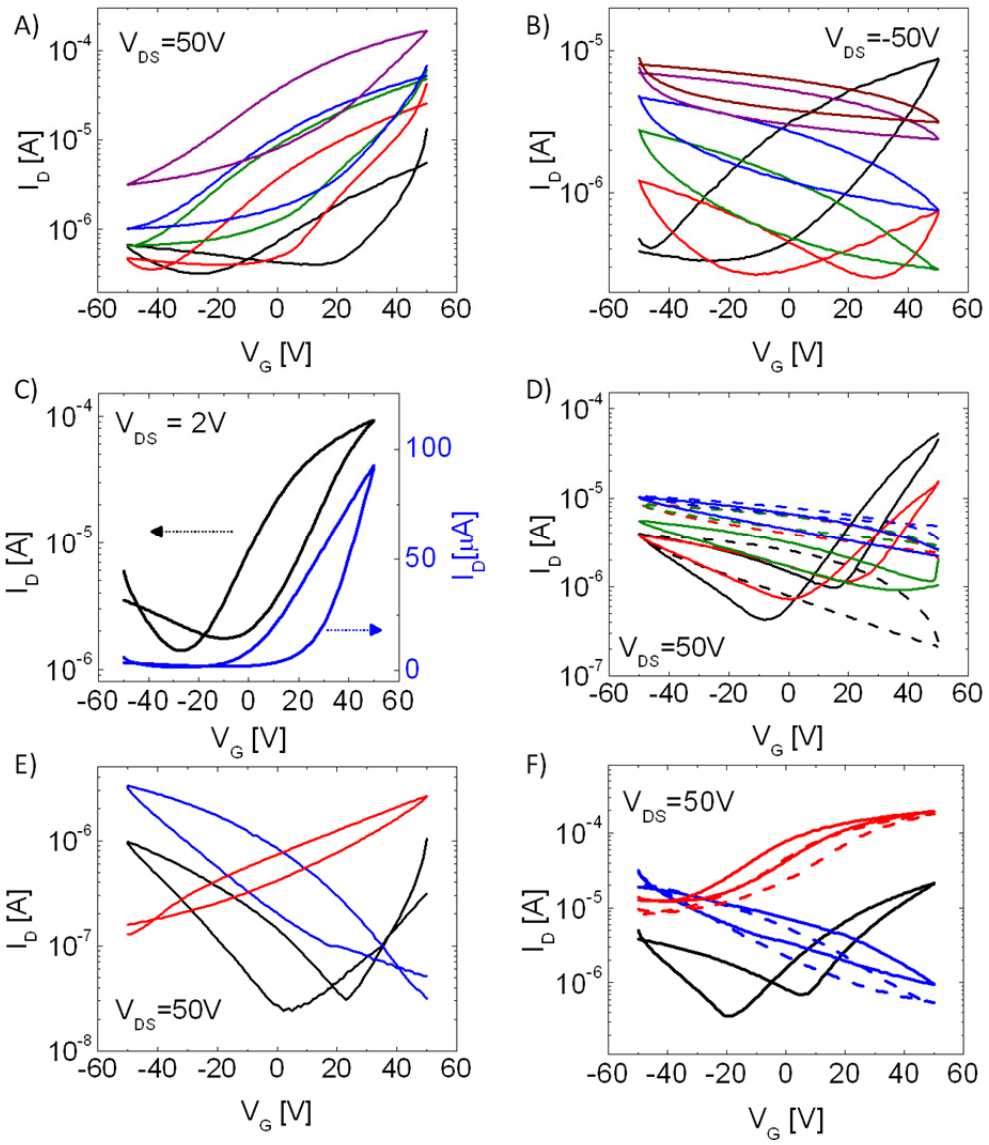

Figure 2.3 (A) Transfer characteristics of PbSe NC FETs in the saturation regime (black) before and after (red) 1 Å, (green) 2 Å, (blue) 3 Å, and (purple) 4 Å of Pb deposition. (B) Transfer characteristics of PbSe NC FET devices in the saturation regime (black) before and after (red) 0.1 Å, (green) 0.2 Å, (blue) 0.3 Å, (purple) 0.4 Å and 0.5 Å (brown) of Se deposition (C) Transfer characteristics of a PbSe NC FET in the linear regime after 3 Å

of Pb deposition (D) Transfer characteristics of PbSe NC FETs in the saturation regime with NC channel thickness' of (black) 35 nm, (red) 70 nm, (green) 105 nm, (blue) 140 nm. Dashed line and solid line indicate before and after deposition of 1 Å of Pb, respectively. (E) Transfer characteristics in the saturation regime of SCN treated PbS NC FETs (black) before and after (red) 2 Å excess Pb and (blue) 0.2 Å excess Se deposition. (F) Transfer characteristics in the saturation regime of (black) before and after (red) 2 Å excess Pb and (blue) 0.2 Å excess Se PbSe NC FETs. Solid and dashed lines indicate before and after 12 hours of under vacuum of 10^{-7} Torr.

Thermal evaporation of different thicknesses of Pb, ranging from 1 to 4 Å, and Se, ranging from 0.1 to 0.4 Å, are deposited on top of the PbSe NC FETs. As the amount of Pb (Se) is increased, the hole (electron) current decreases and electron (hole) current increases [Figure 3A, B]. In addition, the threshold voltage shifts to negative (positive) voltages, indicating a shift in the Fermi level toward the conduction band (valence band) and thus making the film more n-type (p-type) [Figure 2.1B].[32] While as-prepared devices show large variations in their electrical properties due to $\Delta n_{un} \sim n_e$ or n_h, in Pb and Se rich devices the mobility and current level can be precisely controlled by the amount of material deposition. This is because Δn_{st} (change of carrier concentration by stoichiometric control) is much larger than Δn_{un}, as will be discussed in the Hall and C-V measurement sections.

In the range of V_G=-50 to 50 V, as Pb or Se are deposited, I_{ON}/I_{OFF} first increases up to a maximum value. As more material is deposited, I_{ON}/I_{OFF} decreases, the current level increases, and the devices eventually become metallic, characteristic of a heavily doped, degenerate semiconductor. When 8 Å of Pb or 1 Å of Se are deposited, the films show semi-metallic behavior. This trend, observed by introducing non-stoichiometry in NC thin films, generally agrees with bulk or thin film PbSe where a large deviation from stoichimetric balance results in degenerate characteristics.[13]

High performance semiconductor PbSe NC thin film FETs are fabricated entirely at room temperature with a linear electron mobility of 9.0(±2) cm^2/V-s [Figure 2.3C] and a saturation electron mobility of 11(±2) cm^2/V-s with I_{ON}/I_{OFF} of ~10^2, when 2 to 3 Å Pb are deposited, which is the highest reported mobility among the lead chalcogenide NC

FETs. It should be noted that our high mobilities are not the artificial results of hysteresis. When FETs display large hysteresis, they show two different mobilities coming from two very distinct transconductances (dI_D/dV_G)[33] depending on the scan directions. One mobility will be unrealistically high while the other will be very low, and neither has physical meaning when hysteresis is huge. Kang *et al.*[33] showed meaningful mobility could not be extracted at room temperature from PbSe NC FETs due to large hysteresis. However, our devices, as represented by the device characteristics in Figure 3C, show both a high linear mobility of 10 cm^2/V-s in the reverse scan, and a mobility of 5 cm^2/V-s in the forward scan direction. Our hysteresis is lower in part because we employ ODPA self-assembled on Al_2O_3 in the gate dielectric stack to reduce the trap density at the NC-dielectric interface.[29] Additionally, the hysteresis (ΔV_T) in FETs with excess Pb is greatly reduced (ΔV_T=25 V), as excess Pb passivates surface trap states, in comparison to as-prepared NC FETs (ΔV_T=60 V). When 0.2 to 0.3 Å Se are deposited, NC FETs show a linear hole mobility of 0.3(±0.05) cm^2/V-s and a saturation hole mobility of 0.5(±0.1) cm^2/V-s. The FETs have I_{ON}/I_{OFF} of 10^1 to 10^2 and slightly reduced hysteresis (ΔV_T=55 V). Depositing excess metal (Pb) consistently gives rise to higher current and higher mobility than the introduction of excess chalcogen (Se). Surface states within the bandgap of non-stoichiometric PbSe NCs have been theoretically studied, and are associated with dangling Se bonds above the valence band maximum and dangling Pb bonds below the conduction band minimum.[34] Further study is needed to investigate the energies and concentrations of electron and hole trap states introduced through non-

stoichiometry that give rise to the difference in the observed carrier mobilities and current levels in devices.

We investigate the diffusion length of thermally evaporated Pb and Se atoms in the NC thin film by studying the polarity of charge transport in bottom contact PbSe NC FETs[35] with channel thicknesses ranging from 10 to 150 nm. The region of the NC thin film channel for which the conductance may be modulated by the gate voltage is the layer within the Debye screening length from the interface with the bottom gate dielectric layer. The Debye length (L_D) in the NC thin film can be calculated as

$$L_D = \left(\frac{\varepsilon_S \varepsilon_0 k_B T}{e^2 n} \right)^{0.5} \tag{1}$$

where ε_s is the effective dielectric constant of the NC thin film, ε_0 is the vacuum permittivity, k_B is the Boltzmann constant, e is the electric charge, and n is the carrier concentration. We found ε_s to be 24 for a film composed of 6 nm PbSe NCs. Given that L_D varies inversely with n, for as-prepared PbSe NC films we calculate L_D ~20 nm, which corresponds to around three layers of 6 nm NCs. Therefore, NCs in the film beyond the first 20 nm from the semiconductor-gate dielectric interface will contribute relatively little to the conductance modulation of the majority carrier in the device. As seen in Figure 2.3D, 1 Å of Pb can switch the FET polarity to n-type when the film is thinner than 105 nm, but it cannot change the device polarity when the film is thicker than 105 nm, indicating that 1 Å of Pb can diffuse up to at least ~60-80 nm. Similarly, 0.2 Å of Se can diffuse up to at least 50-70 nm. This partial conduction type change promises

the fabrication of more complicated architectures such as p-n or p-i-n junctions by multiple deposition of Pb or Se at different thicknesses.

PbSe NC FETs treated with 1M hydrazine, [note: 1M hydrazine treatment for 5 min is insufficient to achieve unipolar n-type behavior and devices show predominantly n-type ambipolar behavior[6]] EDT, and BDT also show similar transformations when extra Pb or Se are deposited. Regardless of the composition of the ligand, PbSe NC FETs display n-type behavior when Pb-rich and p-type behavior when Se-rich. We find that this method of achieving n-type and p-type films can be applied to other lead chalcogenides. Pb-rich PbS and Se-rich PbS NC FET transfer curves are shown in comparison to as-prepared devices in Figure 2.3E. It should be noted that PbS NC devices show a larger increase in hole current than PbSe NC FETs when the same amount of Se is deposited.

The stability and reversibility of the polarity of these NC films are studied under vacuum. The n-type Pb-rich stoichiometry proves stable as FET characteristics are almost unchanged after 12 hours under 10^{-7} Torr vacuum [Figure 2.3F]. This is in direct contrast to the hydrazine treatment, the only other reported method in the literature to our knowledge capable of making lead chalcogenide NC FETs unipolar n-type with mobility higher than 1 $cm^2/V\text{-}s$. NC FETs treated with hydrazine are not stable under vacuum due to hydrazine desorption.[1] During the preparation of this paper, the Sargent group reported n-type lead chalcogenide NC thin films achieved through doping with iodine. While these NC thin films have not yet shown as high electron mobilities as ours, they provide another promising route to n-dope NC thin film materials.[36–38] The p-type effect of Se-

rich stoichiometry is similarly stable under vacuum [Figure 2.3F]. Vacuum stable NC doping is technologically important as vacuum deposition of metal contacts is commonly employed in the construction of NC solar cells, thermoelectrics, and FETs.

2.3.2 Carrier Statistics characterized by Hall and Capacitance-Voltage Measurement

To obtain more quantitative data on carrier type and concentration, we conduct Hall measurements using 70 nm spin-coated PbSe NC thin films. Table 2.1 compares the carrier type, Hall coefficients, carrier concentrations, and Hall mobilities of PbSe NC thin films as-prepared and for different introduced excesses of Pb and Se. As-synthesized, SCN-exchanged PbSe NC thin films are primarily p-type with a majority carrier hole concentration of $9\pm6\text{x}10^{16}$ holes/cm^3, but films may also be n-type, possessing majority carrier electrons. The large variation in carrier concentration and carrier type is consistent with FET measurements. Samples prepared by vacuum deposition with excess Pb and Se give rise to majority carrier electrons and holes, respectively. Larger electron or hole concentrations are clearly observed when greater excess Pb or Se are deposited, respectively.

	Intrinsic	Pb 3Å	Pb 10Å	Se 3Å	Se 10Å
Carrier type	Holes or electrons*	Electrons	Electrons	Holes	Holes
Hall coefficient (cm^3/C)	69±18	2.8±0.3	0.52±0.1	8.92±0.7	2.8±0.4
Carrier concentration (cm^{-3})	$9\pm6\times10^{16}$	$2.2\pm0.3\times10^{18}$	$1.2\pm0.2\times10^{19}$	$7\pm1\times10^{17}$	$2.2\pm0.2\times10^{18}$
Hall mobility (cm^2/Vs)	0.28±0.15	0.40±0.05	0.44±0.06	0.33±0.08	0.34±0.05

* Concentration type varies sample-to-sample, but predominantly shows the majority carriers to be holes.

Table 2.1. Hall measurement data

The data clearly show that carrier concentrations induced by intentional stoichiometric manipulation are much larger than unintentional or initial doping concentrations, or $\Delta n_{st} \approx \Delta n_{un} \approx \Delta n_e \approx \Delta n_h$. Quantitatively, films have ~2.9×10^{13} NCs/cm^2, assuming random packing of NCs as seen in SEM and SAXS data. Deposition of 3 Å of Pb provides ~9.8×10^{14} Pb atoms/cm^2, considering the cubic closed-packed structure of lead. Hall measurements reflect a majority carrier electron concentration of 2.2×10^{18} electrons/cm^3 or 1.5×10^{13} electrons/cm^2 in a 70 nm thick film. Therefore, on average, when 33 Pb atoms are added to one NC, 0.5 electrons/NC are generated. Similarly, when 47 Se atoms are added to one NC, 0.3 holes/NC are generated. However, the actual number of Pb or Se atoms needed to generate electrons or holes is anticipated to be smaller than the number of deposited atoms due to the following reasons: 1) not all of the vacuum deposited Pb or Se atoms are effectively bound, decreasing efficiency, 2) not all of the bound Pb or Se atoms are ionized to efficiently dope the NCs, and 3) some Pb (or Se) atoms are compensated by unintentional dopants or defect states, suppressing the electron (or hole) concentration. We note that the Hall mobility does not change dramatically when excess Pb or Se is deposited, unlike the mobility measured in the field-effect transistor geometry. This difference is attributed to filling of surface trap states in the field-effect transistor as the Fermi level shifts towards the conduction (valence) band upon application of a positive (negative) gate voltage.[39] However, there is no applied gate voltage to fill surface trap states in the Hall measurement.

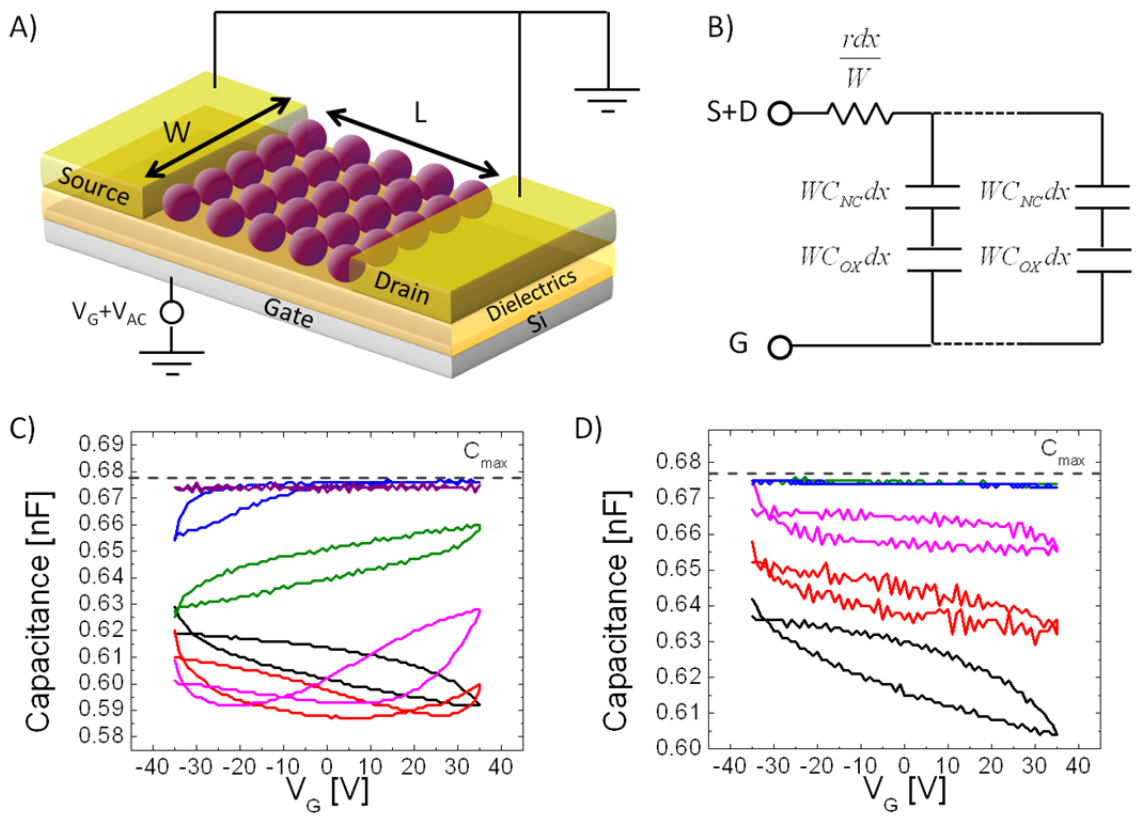

Figure 2.4 (A) Schematic of a metal-semiconductor (PbSe NC thin film)-insulator-metal (MSIM) structure for capacitance voltage (C-V) measurements, (B) equivalent circuit of the channel where r is the sheet resistance, dx is the elements of length in the channel, W is channel width, C_{NC} is capacitance of NC thin film, and C_{OX} is capacitance of oxide in the channel (C) C-V plot (black) before and after (red) 0.3 Å, (pink) 0.6 Å, (green) 0.9 Å, (blue) 1.2 Å, and (purple) 2 Å of Pb deposited (D) C-V plot (black) before and after (red) 0.3 Å, (pink) 0.6 Å, (green) 0.9 Å, and (blue) 1.2 Å of Se deposited.

We fabricate metal-semiconductor (PbSe NC film)-insulator-metal (MSIM) junctions [Figure 2.4A, B] to examine the carrier type, concentration and Fermi level by capacitance – voltage (C-V) measurements using the transmission line method (TLM).[40] The total capacitance (C_{TOT}) is the sum of the capacitances in the channel (C_{CH}) and the oxide capacitance ($C_{OX,SD}$) at the source and drain electrodes, or

$$C_{TOT} = C_{CH} + C_{OX,SD} = \left(1/C_{OX,CH} + 1/C_{NC}\right)^{-1} + C_{OX,SD} \quad (2)$$

where $C_{OX,SD}$ is the capacitance of the oxide in the source and drain region, $C_{OX,CH}$ is the capacitance of the oxide in the channel region and C_{NC} is the NC thin film capacitance.[41] The equivalent circuit of the channel is shown in Figure 4B. In the accumulation region, $C_{NC} \rightarrow \infty$ and therefore $C_{CH} \rightarrow Cox_{,CH}$, so $C_{TOT}=C_{max}=C_{OX,CH} + C_{OX,SD}$.[40,42] When fully depleted, $C_{NC} \rightarrow 0$ and C_{CH}~0, and thus $C_{TOT}=C_{min}=C_{OX,SD}$.[42]

C-V characteristics of as-synthesized, SCN-exchanged PbSe NC films [Figure 2.4 (C and D)] show p-type characteristics with a flatband voltage (V_{FB}) larger than 35 V. When Pb is deposited in increasing excess [Figure 2.4C], the curves show ambipolar behavior transitioning to unipolar n-type. V_{FB} shifts from positive through zero to negative voltages, which reflects the shift in the Fermi level from near the valence band to near the conduction band [Figure 2.1B].[41] As Pb is heavily deposited, V_{FB} shifts outside of the -35 V measurement window and the film has a high concentration of accumulated electrons with a constant capacitance of C_{max}. Complementary behavior is observed as excess Se is deposited [Figure 2.4D]. Initially p-type behavior in as-synthesized and exchanged PbSe NC films does not have high hole accumulation even at

-35 V, and thus the capacitance is smaller than C_{max}. As more Se is deposited [Figure 2.4D], the capacitance increases gradually and reaches C_{max}, indicating that more holes are accumulated, consistent with the Hall and FET measurements. V_{FB} shifts toward more positive values, as the Fermi level of the NC film approaches the valence band [Figure 2.1B]. When 1 to 2 Å of Se are deposited, V_{FB} shifts beyond the 35 V measurement window and the film has a high concentration of accumulated holes with a constant capacitance of C_{max}.

The accumulated mobile charges can be calculated by integrating the C-V characteristics according to $Q = \int_{V_{FB}}^{V} CdV$. We integrated the capacitance of as-synthesized and exchanged PbSe NC thin films from the extrapolated V_{FB} of V_G = 50V to V_G = 0V. The carrier concentration of the pristine NC thin film is calculated to be $6x10^{11}$ holes/cm^2. The carriers are accumulated within the Debye length (20 nm) of the NC film at the semiconductor-gate dielectric interface, which has $8.4x10^{12}$ NCs/cm^2. The carrier concentration corresponds to 0.07 holes/NC. When 0.9 Å of Pb are deposited, the film changes in behavior to n-type. Integrating the accumulated charge from the extrapolated V_{FB} of -140V to 0 V gives $3.6x10^{12}$ electrons/cm^2. The excess Pb corresponds to the addition of 34 atoms/NC and an increase of 0.6 electrons/NC. Similarly, when 0.3 Å of Se are deposited, integrating the accumulated charge from the extrapolated V_{FB} of 100V to 0 V gives $3.0x10^{12}$ holes/cm^2. The excess Se corresponds to an addition of 16 atoms/NC and an increase of 0.15 holes/NC. The Δn_{st} found by the C-V measurements upon introduction of excess Pb and Se atoms is consistent with the values found from samples probed by Hall measurements. Each atom of excess Pb or Se, within a factor of

two, provides the same number of additional electrons and holes. This supports the interpretation that the difference in the measured current levels in Pb- and Se-rich NC FETs arises from a difference, not in carrier concentration, but in carrier mobility.

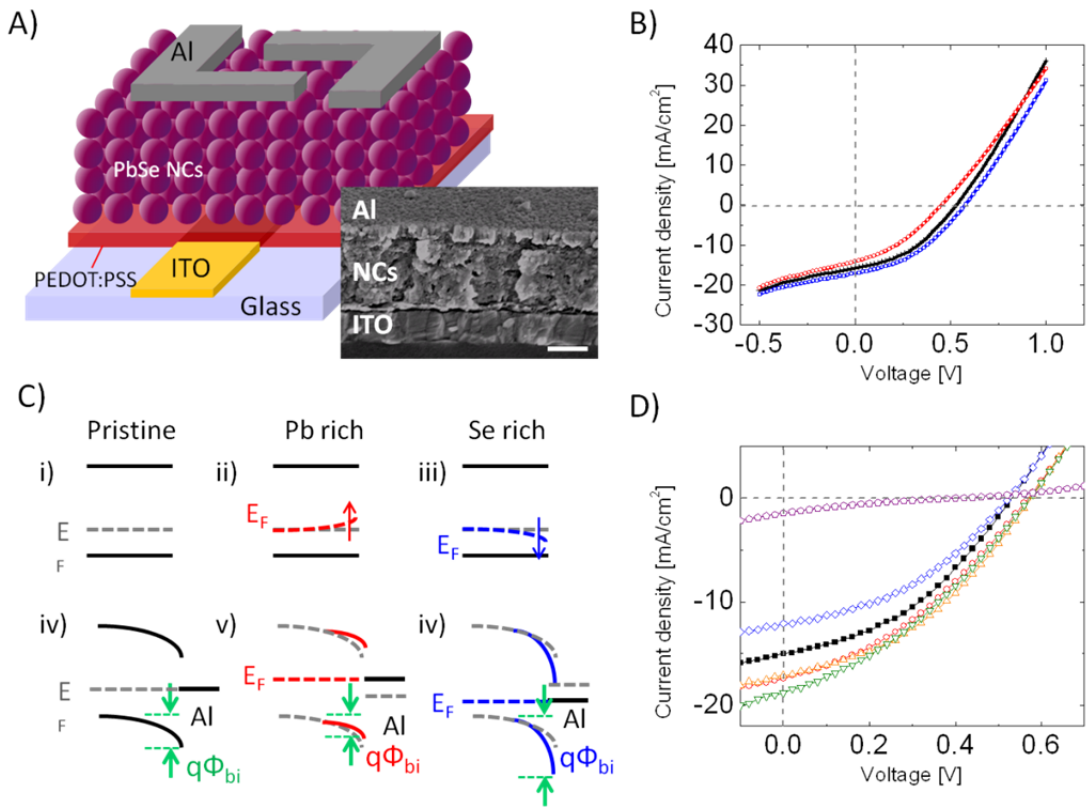

Figure 2.5 (A) Schematic of 2.5 nm PbSe NC Schottky solar cell and device cross sectional SEM image (scale bar : 100nm), (B) current density-voltage characteristics of (black) pristine, after deposition of (red) 0.2 Å excess Pb and (blue) 0.2 Å excess Se, (C) band diagrams for (black) pristine, (red) Pb-rich and (blue) Se-rich PbSe NC Schottky junctions with Al electrodes, and (D) current density-voltage characteristics of Se-rich solar cells (black) before and after (red) 0.1 Å, (orange) 0.2 Å, (green) 0.4 Å, (blue) 0.8 Å and (purple) 2 Å of Se deposited.

2.3.3 PbSe Schottky Solar cell enhanced by non-stoichiometry

We utilize non-stoichiometry to engineer the carrier concentration in PbSe NC solids integrated as the single photoactive layer in Schottky solar cells [Figure 2.5A].[43] PEDOT:PSS is spincoated onto patterned ITO substrates and the devices are annealed at 150˚C. For photovoltaics, small 2-3 nm diameter PbSe NCs with the first excitonic absorption resonance at 800-900 nm are used, as larger bandgap PbSe NCs are known to provide a higher open circuit voltage.[44] Multiple layers of PbSe NCs are spincoated and soaked in BDT in acetonitrile until the desired thickness (180 to 250 nm) is achieved. BDT is selected as it is a strongly bound bidentate linker known to enhance photovoltaic performance.[25,44] Solar cells with active layers thicker than 250 nm show a decrease in efficiency because light absorption in the PbSe NC thin film is limited by charge generation in the depletion region formed at the PbSe NC/Al junction.[44,45] We change the stoichiometry of the films by thermally evaporating 0.2 Å of Se or 2 Å of Pb to make the surface more p-type or n-type, respectively. Aluminum electrodes are thermally evaporated through a shadow mask to complete the cell fabrication, yielding an active region of ~9mm^2.

I-V curves of as-prepared, Pb-rich, and Se-rich PbSe NC Schottky cells are shown in Figure 2.5B. While excess Pb reduces the open circuit voltage (V_{OC}) and efficiency, excess Se increases the V_{OC} and efficiency. Schematic band diagrams of as-prepared, Pb-rich and Se-rich NC solids are shown in Figure 2.5C. As the NC surface becomes n-type (p-type) due to the deposition of excess Pb (Se), the Fermi level moves closer to the conduction (valence) band. When the semiconductor-metal contact is formed, band

bending occurs to align the Fermi level between the metal and semiconductor.[46] While excess Pb reduces the band-bending at the interface, the more strongly p-type interface with excess Se desirably increases band-bending. We note that while the Fermi-level moves closer to the conduction (valence) band with excess Pb (Se), the electron (hole) mobility in the solar cell is more appropriately represented by Hall measurements than by FET measurements. In solar cells low level injection does not shift the quasi-Fermi level sufficiently toward the conduction (valence) band to fill trap states within the energy gap.

We vary the excess Se from 0 to 2 Å to manipulate the band-bending at the metal-semiconductor interface in NC Schottky solar cells [Figure 2.5D]. Initially as the amount of Se is increased, the V_{OC} and efficiency increase, but after some critical point the efficiency begins to decrease. The decrease in solar cell efficiency at higher levels of excess Se may arise from 1) heavily degenerate doping of the interface[47] and/or 2) reduced carrier lifetime due to increased impurities.[48] Maximum power conversion efficiencies of up to 3.85% are realized by introducing 0.2 Å of excess Se, enhanced in comparison to efficiencies of 3.5% in reference as-prepared NC thin film devices.

2.4 Conclusions

In summary, we show that the carrier statistics in lead chalcogenide NC thin films can be precisely controlled by stoichiometric imbalance. We have studied the relationship between excess Pb and Se and the carrier type, concentration and Fermi level in lead chalcogenide NC thin film solids. We applied this method to build robust and high

performance unipolar n- and p-type NC field effect transistors at room temperature as well as solar cells with increased power conversion efficiency. This study contributes to the fundamental understanding of the electronic properties of lead chalcogenide nanostructures and the role of stoichiometric imbalance in engineering this family of materials for various applications such as thermoelectrics, electronics and optoelectronics.

2.5 References

(1) Talapin, D. V.; Murray, C. B. *Science* **2005**, *310*, 86–89.

(2) Koh, W.; Saudari, S. R.; Fafarman, A. T.; Kagan, C. R.; Murray, C. B. *Nano Lett.* **2011**, *11*, 4764–4767.

(3) Wang, R. Y.; Feser, J. P.; Lee, J.-S.; Talapin, D. V.; Segalman, R.; Majumdar, A. *Nano Lett.* **2008**, *8*, 2283–2288.

(4) Ip, A. H.; Thon, S. M.; Hoogland, S.; Voznyy, O.; Zhitomirsky, D.; Debnath, R.; Levina, L.; Rollny, L. R.; Carey, G. H.; Fischer, A.; *et al.,* **2012**, *7*, 577–582.

(5) Sukhovatkin, V.; Hinds, S.; Brzozowski, L.; Sargent, E. H. *Science* **2009**, *324*, 1542–1544.

(6) Semonin, O. E.; Luther, J. M.; Choi, S.; Chen, H.-Y.; Gao, J.; Nozik, A. J.; Beard, M. C. *Science* **2011**, *334*, 1530–1533.

(7) Tang, J.; Kemp, K. W.; Hoogland, S.; Jeong, K. S.; Liu, H.;Levina, L.; Furukawa, M.; Wang, X.; Debnath, R.; Cha, D.; *et al., Nat. Mater.* **2011**, *10*, 765–771.

(8) Efros, A. L.; Efros, A. L. *Sov. Phys. Semicond.* **1982**, *16*, 772-775.

(9) Luther, J. M.; Law, M.; Song, Q.; Perkins, C. L.; Beard, M. C.; Nozik, A. J. *ACS Nano* **2008**, *2*, 271–280.

(10) Leschkies, K. S.; Kang, M. S.; Aydil, E. S.; Norris, D. J. *J. Phys. Chem. C* **2010**, *525*, 9988–9996.

(11) Ravich, U. I. *Semiconducting Lead Chalcogenides*; Plenum Press: New York, 1970.

(12) Allgaier, R. S.; Scanlon, W. W. *Phys. Rev.* **1958**, *111*, 1029-1037.

(13) Schlichting, U.; Gobrecht, K. *J. Phys. Chem. Solids* **1973**, *34*, 753–758.

(14) Logothetis, E.; Holloway, H. **1970**, *8*, 1937–1940.

(15) Moreels, I.; Lambert, K.; Muynck, D. D. *Chem. Mater.* **2007**, *19*, 6101–6106.

(16) Moreels, I.; Fritzinger, B.; Martins, J. C.; Hens, Z. Surface Chemistry of Colloidal PbSe Nanocrystals. *J. Am. Chem. Soc.* **2008**, *130*, 15081–15086.

(17) Fafarman, A. T.; Koh, W.-K.; Diroll, B. T.; Kim, D. K.; Ko, D.-K.; Oh, S. J.; Ye X.; Doan-Nguyen, V; Crump, M. R; Reifsnyder, D. C. *et al.*, *J. Am. Chem. Soc.* **2011**, *133*, 15753–15761.

(18) Choi, J.-H.; Fafarman, A. T.; Oh, S. J.; Ko, D.-K.; Kim, D. K.; Diroll, B. T.; Muramoto, S.; Gillen, J. G.; Murray, C. B.; Kagan, C. R. *Nano Lett.* **2012**, *12*, 2631–2638.

(19) Liu, Y.; Gibbs, M.; Puthussery, J.; Gaik, S.; Ihly, R.;Hillhouse, H. W.; Law, M. *Nano Lett.* **2010**, *10*, 1960–1969.

(20) Talgorn, E.; Gao, Y.; Aerts, M.; Kunneman, L. T.; Schins, J. M.; Savenije, T. J.; van Huis, M.; van der Zant, H. S. J.; Houtepen, A. J.; Siebbeles, L. D. *Nat. Nanotechnol.* **2011**, *6*, 733–739.

(21) Law, M.; Beard, M. C.; Choi, S.; Luther, J. M.; Hanna, M. C.; Nozik, A. J. *Nano Lett.* **2008**, *8*, 3904–3910.

(22) Beard, M. C.; Midgett, A. G.; Law, M.; Semonin, O. E.; Ellingson, R. J.; Nozik, A. J. *Nano Lett.* **2009**, *9*, 836–845.

(23) Kang, M.; Lee, J.; Norris, D.; Frisbie, C. *Nano Lett.* **2009**, *9*, 3848–3852.

(24) Law, M.; Luther, J. M.; Song, Q.; Hughes, B. K.; Perkins, C. L.; Nozik, A. J. *J. Am. Chem. Soc.* **2008**, *130*, 5974–5985.

(25) Koleilat, G.; Levina, L.; Shukla, H.; Myrskog, S. *ACS Nano* **2008**, *2*, 833–840.

(26) Liu, Y.; Gibbs, M.; Perkins, C. L.; Tolentino, J.; Zarghami, M. H.; Bustamante, J.; Law, M. *Nano Lett.* **2011**, *11*, 5349–5355.

(27) Koole, R.; Liljeroth, P. *J. Am. Chem. Soc.* **2006**, *128*, 10436–10441.

(28) Oh, S. J.; Kim, D. K.; Kagan, C. R. *ACS Nano* **2012**, *6*, 4328–4334.

(29) Kim, D. K.; Lai, Y. L.; Vemulkar, T. R.; Kagan, C. R. *ACS Nano* **2011**, *5*, 10074-10083.

(30) Petkov, V.; Moreels, I.; Hens, Z.; Ren, Y. *Phys. Rev. B* **2010**, *81*, 241304(1-4).

(31) Kim, D. K.; Vemulkar, T. R.; Oh, S. J.; Koh, W.-K.; Murray, C. B.; Kagan, C. R. *ACS Nano* **2011**, *5*, 3230–3236.

(32) Moon, S.; Lee, S.-G.; Song, W.; Lee, J. S.; Kim, N.; Kim, J.; Park, N. *Appl. Phys. Lett.* **2007**, *90*, 092113(1-3).

(33) Kang, M. S.; Sahu, A.; Norris, D. J.; Frisbie, C. D. *Nano Lett.* **2011**, *11*, 3887–3892.

(34) Gai, Y.; Peng, H.; Li, J. *J. Phys. Chem. C* **2009**, *113*, 21506–21511.

(35) While all other FET measurements were conducted in top contact configuration, as top contact structures form higher mobility devices, diffusion length studies as a function of film thickness were carried out using bottom contact structures. When the film is thick in top contact devices, resistance between the electrode and the channel, known as "access resistance," increases. This phenomenon can be avoided in the case of bottom contact devices as the metal electrode is in direct contact with the NC thin film channel.

(36) Tang, J.; Liu, H.; Zhitomirsky, D.; Hoogland, S.; Wang, X.; Furukawa, M.; Levina, L.; Sargent, E. H. *Nano Lett.* **2012**, *12*, 4889–4894.

(37) Zhitomirsky, D.; Furukawa, M.; Tang, J.; Stadler, P.; Hoogland, S.; Voznyy, O.; Liu, H.; Sargent, E. H. *Adv. Mater.* **2012**, 24, 6181-6185.

(38) Ning, Z.; Ren, Y.; Hoogland, S.; Voznyy, O.; Levina, L.; Stadler, P.; Lan, X.; Zhitomirsky, D.; Sargent, E. H. *Adv. Mater.* **2012**, 24, 6295-6299.

(39) Shur, M; Hack, M. *J. Appl. Phys.* **1984**, 55, 3831-3842

(40) Greve, D. W.; Hay, V. R. *J. Appl. Phys.* **1987**, *61*, 1176-1180.

(41) Sze, S. M.; Ng, K. K. *Physics of Semiconductor Devices*; 3rd ed.; John Wiley & Sons: New Jersey, 2007.

(42) Hamadani, B. H.; Richter, C. A.; Suehle, J. S.; Gundlach, D. J. *Appl. Phys. Lett.* **2008**, *92*, 203303(1-3).

(43) Luther, J. M.; Law, M.; Beard, M. C.; Song, Q.; Reese, M. O.; Ellingson, R. J.; Nozik, A. J. *Nano Lett.* **2008**, *8*, 3488–3492.

(44) Ma, W.; Swisher, S.; Ewers, T.; Engel, J.; Ferry, V. E.; Atwater, H. A.; Alivisatos, A. P. *ACS Nano* **2011**, *5*, 8140–8147.

(45) Pattantyus-Abraham, A.; Kramer, I. *ACS Nano* **2010**, *4*, 3374–3380.

(46) Rhoderick, E. H. *Metal-Semiconductor Contacts*; 2nd ed.; Claredon Press: Oxford, 1988.

(47) Nelsons, J. *The Physics of Solar Cells*; Imperial College Press, 2003.

(48) Zogg, H.; Vogt, W.; Baumgartner, W. *Solid-State Electron.* **1982**, *25*, 1147–1155

(49) Yu, W. W.; Falkner, J. C.; Shih, B. S.; Colvin, V. L. *Chem. Mater.* **2004**, *35*, 3318–3322.

(50) Hines, M. a.; Scholes, G. D. *Adv. Mater.* **2003**, *15*, 1844–1849.

CHAPTER 3 Designing High-Performance PbS and PbSe Nanocrystal Electronic Devices through Stepwise, Post-Synthesis, Colloidal Atomic Layer Deposition

This work was published in Nano Letters, entitled "Designing High-Performance PbS and PbSe Nanocrystal Electronic Devices through Stepwise, Post-Synthesis, Colloidal Atomic Layer Deposition" S. J. Oh, N. E. Berry, J.-H. Choi, E. A. Gaulding, Hangfei Lin, T. Paik, B. T. Diroll, A. T. Fafarman, S. Muramoto, C. B. Murray, and C. R. Kagan, Nano Letters, (2014) *14*, 1559–1566

We report a simple, solution-based, post-synthetic colloidal, atomic layer deposition (PS-cALD) process to engineer stepwise the surface stoichiometry and therefore the electronic properties of lead chalcogenide nanocrystal (NC) thin films integrated in devices. We found that unlike chalcogen-enriched NC surfaces that are structurally, optically and electronically unstable, lead chloride treatment creates a well-passivated shell that stabilizes the NCs. Using PS-cALD of lead chalcogenide NC thin films we demonstrate high electron field-effect mobilities of ~4.5 cm^2/Vs.

3.1 Introduction

Colloidal semiconductor nanocrystals (NCs) have been shown to be promising materials for electronic,[1] optoelectronic[2–4] and thermoelectric[5] applications, because of their tunable electronic and optical properties and the low-cost and simple solution-based processing techniques available to integrate NCs as thin film solids into devices. To engineer the properties of NC thin films and the behavior of NC devices for applications, the type, concentration, and mobility of charge carriers and the density and energy of surface states in semiconductor NCs must be precisely controlled; akin to bulk semiconductor device design. However, thin films constructed from assemblies of NC building blocks are unlike bulk semiconductors. NC building blocks have a high surface-to-volume ratio presenting both a greater challenge and an opportunity to tailor NC thin film electronic properties, as large surface areas may create undesirable trap states and may be manipulated to control carrier statistics. Recent reports[6] have introduced a number of methods to influence carrier and trap concentrations in NC thin films by doping NCs, through control over stoichiometry,[6–8] incorporation of novel ligands[1,9] or foreign atoms[4,10,11] and employing electrochemical treatments,[12,13] and by passivating the NC surface.[2,3,14,15] NC assemblies require unique control over interparticle distance and organization. Recent introduction of compact ligand chemistries has greatly reduced interparticle spacing and increased interparticle coupling, with demonstrations of carrier mobilities >10 cm^2/Vs.[8,10,16,17] Solution-based techniques enable the deposition of ordered NC solids,[18–22] that promise enhanced charge transport,[23] through the Anderson transition.[24]

In bulk lead chalcogenides small deviations in compound stoichiometry, enriching the material in lead or chalcogen have been exploited since the 1950s to n- and p- dope the semiconductor, respectively. In lead chalcogenide NC analogs, stoichiometric control has begun to gain much attention as a route to engineer the materials properties and construct higher performance devices.[6–8,25,26] NC stoichiometry has been tailored 1) during synthesis *via* the Successive Ionic Layer Adsorption and Reaction (SILAR) method that introduces non-stoichiometry at the NC surface by building on a stoichiometric core,[26,27,28] or 2) after NC synthesis through exchange of surface ligands with chalcogen containing compounds, namely thiols,[14,29,30] or as we reported, through thermal evaporation of elemental Pb or Se.[8] However, methods that control charge carrier concentration during synthesis by surface modification (case 1), such as stoichiometric control *via* the SILAR method, cannot guarantee that during device fabrication the surface remains unchanged and therefore the properties introduced are retained. During the solution-based deposition and ligand exchange processes used to realize conductive NC solids in devices, the surface of NCs are typically altered dramatically due to interactions of the NC surface with ligands and solvent.[31] This complexity prevents the prediction of NC thin film properties. Therefore, employing post-deposition charge carrier control (case 2), in particular stoichiometric control, has gained great interest as a pathway to design NC materials with tailored electronic and optoelectronic properties.[6,7] Developing a solution-based method for stoichiometric control of NC thin films would provide a powerful tool for low cost materials design.

Solution-based deposition of lead chalcogenide NC thin films, even by rapid spin-coating and dip-coating techniques, shows degrees of order unlike other semiconductor NCs. However, the order seen in NC assemblies bearing the original long ligands used in synthesis, has often been lost upon ligand exchange with the more compact chemistries employed to transform these materials into conductive solids. Liquid surface ligand exchange[20] or chemical treatments that strip the ligands used in synthesis have been reported to form ordered and/or interconnected lead chalcogenide NC superlattices, through proposed mechanisms such as oriented attachment[32–34] and selective ligand displacement.[21,22] Despite synthetic success in preparing these ordered, nanostructured architectures, there are no reports that control the NC carrier and trap statistics and integrate these materials into state-of-the art devices.

Here we report a simple and systematic, solution-based method to control the stoichiometry of lead chalcogenide NC thin films after deposition and achieve short-range ordered, conductive NC superlattices. Post-synthesis, colloidal atomic layer deposition (PS-cALD) is used sequentially: first, by employing a chalcogenide salt to reduce the interparticle distance and form short-range ordered, fused NC structures bearing a chalcogen shell. Next, we introduce the salt, $PbCl_2$ to form a Pb shell. We explore the chemical, structural, electronic and optical properties of chalcogen-rich and Pb-rich NC thin films and show that the composition of surface adatoms dominates the thin film properties. Enriching the NC surface in chalcogen creates high energy surfaces that drive NC fusion into ordered thin film solids. These chalcogen-terminated solids possess a high density of trap states, are oxygen sensitive, and have poor, heavily p-type

charge transport. Subsequent treatment of these NC solids with $PbCl_2$ renders the NC surfaces Pb-rich, stabilizing the NC surface toward oxygen and passivating the surface electronically, giving rise to enhanced electron transport. We carry out PS-cALD in the platform of field-effect transistors (FETs) to transform as-synthesized NCs into Pb-enriched, ordered and interconnected, but still quantum-confined NC solids, and demonstrate high-performance n-type behavior with electron mobilities rivaling the highest previously reported for lead chalcogenide NC FETs.

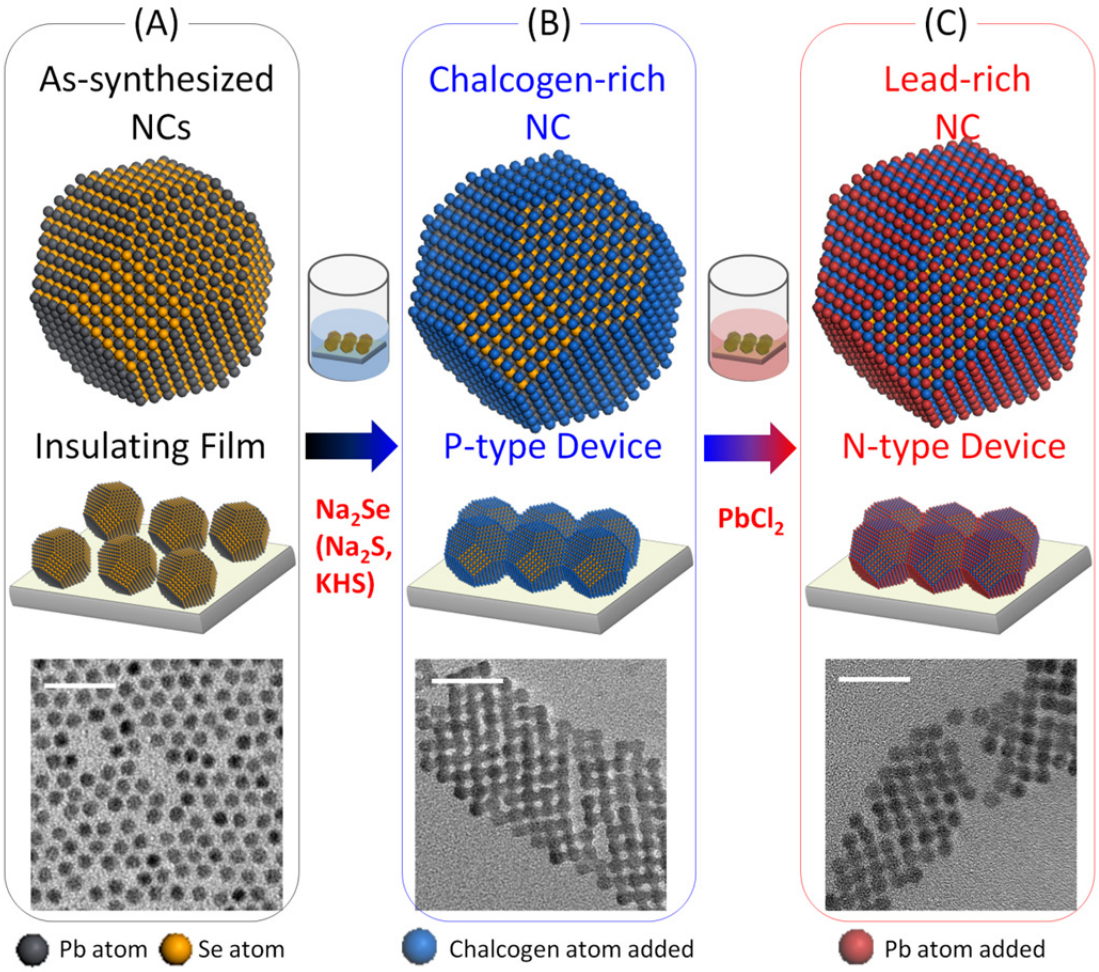

Figure 3.1 Post-Synthetic, colloidal Atomic Layer Deposition (PS-cALD) of lead chalcogenide NC thin films. Schematic of NC assemblies, detailed illustration of the interface between NCs and TEM images exemplified by 5.9 nm PbSe NCs. (A) As-synthesized, spincast NC thin films, are treated in solutions of either Na_2Se, Na_2S, or KHS (B) to exchange the long-insulating ligands introduced during synthesis and to chalcogen enrich the NC surface. Further treatment with $PbCl_2$ (C) enriches the NC film in Pb. For the simplified picture, the organic and inorganic ligands are omitted and the atoms at the interface may reconstruct to minimize energy. (scale bar : 20nm)

3.2 Experimental Details

3.2.1 Post-Synthtic-Colloidal Atomic Layer Deposition Method

6.0 nm PbS and 5.9 nm PbSe NCs capped with oleic acid ligands are synthesized as previously reported.[35,36] NCs are deposited onto substrates by spincasting to form 20-30 nm NC thin films. We employ PS-cALD to treat the NC thin films sequentially in chalcogenide and lead salts to control NC stoichiometry. Figure 3.1(A) shows as-synthesized and deposited NC solids. The thin films are comprised of hexagonally ordered domains of NCs that are well-separated (~1.5 nm) by the long and bulky oleic acid ligands. The substrates are immersed in a methanolic solution containing a chalcogenide from the salts of Na_2Se, Na_2S or KHS.[15,37] The surface of synthesized lead chalcogenide NCs is Pb-rich,[38] providing many binding sites for chalcogenide adsorption. The chalcogenide (Se^{2-} or S^{2-}) replaces the original oleic acid ligands, and creates a chalcogen shell,[15,37,39] greatly reducing to completely eliminating the interparticle spacing [Figure 3.1(B)]. HRTEM and TEM images [Figure 3.1(B)] show individual NCs with evidence of fusion along the {100} NC facets, similar to the recent report of "confined, but connected" NCs by Hanrath.[21] Oleic acid ligands on {100} lead chalcogenide NCs are reported to have a low binding energy and therefore to detach from the NC surface more readily.[21,22,40–42] Upon exchange with the chalcogenide salt, chalcogenides replace oleic acid on {100} facets first. The facile chalcogenide exchange and the higher energy of the {100} chalcogen terminated surface is consistent with driving fusion in the {100} direction as chalcogen atoms on the {100} facets bridge two NCs. As fusion along the {100} energetically stabilizes the structure, it forms a square ordered network connecting

{100} facets of nearest neighbors, changing the lattice from a hexagonally packed structure to a cubical structure. As exchange proceeds, chalcogenides will replace the more strongly bound oleic acid ligands on {111} facets.

As this chalcogen-terminated surface is unstable,[41–43] we dip the NC thin film solids in an oleylamine solution containing $PbCl_2$. Available surface Se or S atoms react with the Pb precursor to adsorb and enrich the surface in Pb, forming PbSe or PbS shells [Figure 3.1(C)]. The temperature of the solution is kept at 65 ºC, unless otherwise specified, which is high enough to dissolve the $PbCl_2$ in oleylamine and promote the reaction, but low enough to prevent severe NC sintering or growth. This reaction is similar to the synthesis of PbS or PbSe NCs and to the SILAR method used in core-shell NC synthesis. After $PbCl_2$ treatment, the NC thin films still maintain a square ordered structure. Small amounts of oleylamine are observed to remain in the NC thin film after treatment. Sodium or other elements are not detected, as reported for Na_2S treatment of PbSe NC thin films.[15] This indicates that Pb-rich NCs are ligated by a mixture of chloride and oleylamine.

3.3 Results and Discussions

3.3.1 Non-Stoichiometry, Optical, Structural Properties of Chalcogen-rich and Pb-rich Lead chalcogenide NCs

We compare the nature of the structural transformation for different chalcogenide treatments, enriching the NC surface in Se *versus* S. Square ordered NC networks form

through fusion of {100} facets [Figure 3.1(B)], but it is more substantial for Se-rich PbSe NCs than S-rich PbS NCs, as the latter shows less severe fusion. We attribute the increased fusion of Se-rich PbSe NCs to the more unstable and high surface energy of Se. In the case of S-rich PbSe NCs, a similar transformation was observed, but with a slightly random or tilted {100} fusion. We attribute the more random fusion of the S-rich PbSe NCs additionally to a larger lattice mismatch due to the smaller size of the S atom.

We characterize the change in stoichiometry upon PS-cALD, using both Na_2Se and Na_2S salts to introduce surface chalcogens and $PbCl_2$ to add surface Pb for 5.9 nm PbSe NC thin films, by Inductively Coupled Plasma Optical Emission Spectroscopy (ICP-OES) and Energy Dispersive X-ray (EDX) spectroscopy, as summarized in Table 1. ICP-OES shows that the initial oleic acid capped PbSe NCs have a Pb:Se ratio of 1.15:1, in accordance with literature values and reports of a Pb-rich NC surface.[15,38,40,44] Upon Na_2Se treatment, the amount of Se increases and the ratio decreases to 0.84:1. After $PbCl_2$ treatment, the ratio reverts back to a higher ratio of Pb of 1.07. When PbSe NCs are treated with Na_2S, the Pb:Se ratio does not change significantly because only S ions bind to the NCs by replacing oleic acid ligands.[15] After the $PbCl_2$ treatment, however, the ratio increases to 1.46:1, while the amount of S change is small as confirmed by SIMS measurements. ICP-OES measurements are consistent with the addition of chalcogenides to the NCs upon Na_2Se or Na_2S treatment,[15] and the addition of Pb ions to surface chalcogen atoms after the $PbCl_2$ treatment. This trend is similarly observed in our EDX data, but a slightly higher Pb:Se ratio is consistently measured.

We correlate the change in stoichiometry with the NC thin film morphology, as the number of sites to which ions can be added depends on the evolution in its structure during treatment. We model the 5.9 nm PbSe NCs as truncated octahedra[40] terminated with eight {111} and six {100} facets [Figure 3.1] and composed of 2190 Pb atoms and 1925 Se atoms. While the exact structure of the NC surface has yet to be determined experimentally and many different models have been proposed,[22,40–44] here, we assume that all {100} facets are stoichiometric and equally Pb and Se terminated, and all {111} facets are non-stoichiometric and Pb-terminated.[22,41] This model is consistent with a Pb:Se ratio greater than one. Our model shows that all of the parameters such as shape, diameter, stoichiometry, number of atoms, and net charge are in reasonable ranges compared to literature data.[22,32,40–44]

Pb:Se	Oleic Acid capped PbSe NCs	Na_2Se treated PbSe NCs	Na_2Se, $PbCl_2$ treated PbSe NCs	Na_2S treated PbSe NCs	Na_2S, $PbCl_2$ treated PbSe NCs
ICP	1.15 ± 0.05	0.84 ± 0.04	1.07 ± 0.05	1.20 ± 0.06	1.46 ± 0.07
EDX	1.30 ± 0.07	1.01 ± 0.06	1.20 ± 0.07	1.33 ± 0.08	1.59 ± 0.1
Model	1.14	0.85	1.07	1.14	1.45

Table 3.1 Stoichiometry changes of PbSe NC thin films during Post-Synthetic, colloidal Atomic Layer deposition monitored by ICP-OES and EDX

As we treat the NCs with chalcogenides, chalcogenides replace oleic acid ligands and the NCs start to fuse along the {100} by sharing common chalcogen atoms. Upon Na_2Se treatment, 64 Se atoms can sit on each of the 8 {111} facets, and 50 atoms can sit on the 6 {100} facets, though only half of the Se on the {100} facets will contribute. After this process, the calculated stoichiometry of the NC thin film is 0.85:1. After $PbCl_2$ treatment, the sites to which Pb ions can attach are limited to only the available surface Se atoms on the {111} facets, as Se introduced on the {100} facets of NCs are fully bonded. The stoichiometry of the NC thin film would be 1.07:1. Using the same structural model upon chemical treatment for the case of Na_2S and $PbCl_2$ salts, the final stoichiometry of Pb:Se is calculated to be 1.45:1. This model is in good agreement with our ICP-OES data and the trend measured by EDX [Table 3.1]. It should be mentioned that, as presented in electron microscopy images, not all NCs fuse together upon chalcogenide treatment. This may arise from initial disorder and incomplete structural transformation upon chalcogenide treatment to order and orient the NCs. Therefore for NCs that do not fuse, Se atoms on those {100} facets are not shared between two NCs. This would result in a slightly lower Pb:Se ratio for chalcogenide treated NCs. Additionally, those {100} facets will allow more Pb ions to be attached, resulting in a slightly higher Pb:Se ratio upon $PbCl_2$ treatment.

We monitor the changes in the Pb:Se ratio over the time of each treatment through EDX measurements. As the chalcogenide treatment occurs in seconds, it is difficult to observe the time dependence of the chalcogenide exchanges. For $PbCl_2$ treatment at 65 ºC, the number of Pb atoms increases rapidly in the first hour and then saturates.

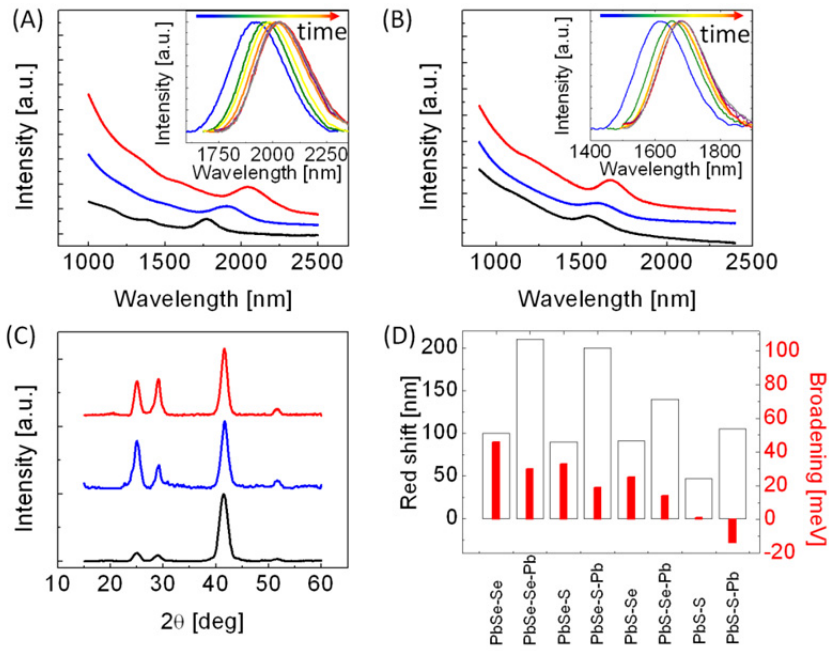

Figure 3.2 (A) Absorption spectra of as-synthesized 5.9 nm PbSe NC thin films (black) and upon Se (blue) and Pb (red) enrichment. Inset : The first excitonic peak of Se-rich PbSe NCs before (blue) and after 10 s (green), 1 min (yellow), 1 h (orange), 12 h (red), and 24 h (purple) of $PbCl_2$ treatment at 65 ºC, or 10 min of $PbCl_2$ treatment at 95 ºC (grey). (B) Absorption spectra of as-synthesized 6 nm PbS NC thin films (black) and upon S (blue) and Pb (red) enrichment. Inset : The first excitonic peak of S-rich PbS NCs before (blue) and after 10 s (green), 1 min (yellow), 1 h (orange), 12 h (red), 24 h (purple) of $PbCl_2$ treatment at 65 ºC, or 10 min of $PbCl_2$ treatment at 95 ºC (grey). (C) Wide angle X-ray scattering for as-synthesized (black), Na_2Se (blue) and both $PbCl_2$ and Na_2Se (red) treated PbSe NC thin films. (D) The red shift and broadening of the first excitonic peak of PbSe and PbS NCs with different chalcogenide exchange chemistries and after $PbCl_2$ treatment.

We measure the optical absorption spectra of PbSe and PbS NC thin films treated with Na_2Se and Na_2S, respectively, followed by $PbCl_2$ treatment [Figure 3.2 (A,B)]. For PbSe NCs, as-synthesized 5.9 nm oleic acid capped NC thin films show the first excitonic peak at ~1800 nm. After Na_2Se treatment, a noticeable red shift of ~35 meV and increased broadening of ~45 meV are observed. Wide angle X-ray scattering (WAXS) measurements reveal significant 18% line narrowing of the diffraction peaks, consistent with NC fusion and growth [Figure 3.2(C)]. Our model [Figure 3.1(B)] suggests chalcogen shell growth gives rise to an effective increase in NC diameter from 5.9 nm to 6.2 nm. Given the effective increase in NC size, we attribute the red-shift in the optical absorption spectrum to arise from a combination of NC fusion (~20 meV) and shell growth (~15 meV). After $PbCl_2$ treatment, there is a further red-shift (35 meV) of the first excitonic peak in the absorption spectrum and ~5% line narrowing in the WAXS patterning, which we mostly ascribe to an effective increase in NC diameter of 6.5 nm after Pb shell formation [Figure 3.1(C)]. However, the excitonic peak width becomes narrower by 16 meV, rather than broader. PbS NC thin films show a similar spectral evolution upon treatment with Na_2S and $PbCl_2$ [Figure 3.2(B)]. The absorption spectra of chalcogen-rich NC thin films are consistently broader than as-synthesized, oleic acid capped NC thin films or chalcogen-enriched and subsequently Pb-enriched NC thin films, which will be discussed below. It should be noted that even though some fusion was observed, the NC thin films still show strong quantum confinement effects due to the large Bohr radii (~46nm for PbSe and 18nm for PbS) of the lead chalcogenides.

While the transformation upon chalcogenide treatment is very fast, we use the first excitonic transition from absorption measurements to monitor the evolution of shell formation as a function of $PbCl_2$ treatment time [inset of Figure 3.2(A,B)]. For reaction temperatures of 65 ºC, most of the shell forms within 1 h, in good agreement with our EDX results, and remains unchanged beyond 12 h, consistent with self-limited shell growth. At higher temperatures of 95 ºC, the total reaction time is reduced to 10 min.

The red shift and broadening of the first excitonic peak for PbSe and PbS NC thin films with different combinations of Na_2Se and Na_2S treatments and subsequent $PbCl_2$ treatment are compared and summarized in Figure 3.2(D). Treatment of the PbSe NC surface with S anions, in contrast to Se anions, shows a similar but slightly smaller red-shift, consistent with the reduced NC fusion seen in TEM images and smaller line narrowing of 8% measured in WAXS reflections. After $PbCl_2$ treatment, the first excitonic peak for the S-enriched PbSe NC thin films show further red-shifts, but not as significantly as for Se-enriched surfaces. Generally it is observed that Se-treatment shows a greater red-shift and broadening than S-treatment. In the case of PbS NCs treated with both Na_2S and $PbCl_2$, the first excitonic peak is even narrower than as-deposited and oleic acid capped PbS NCs.

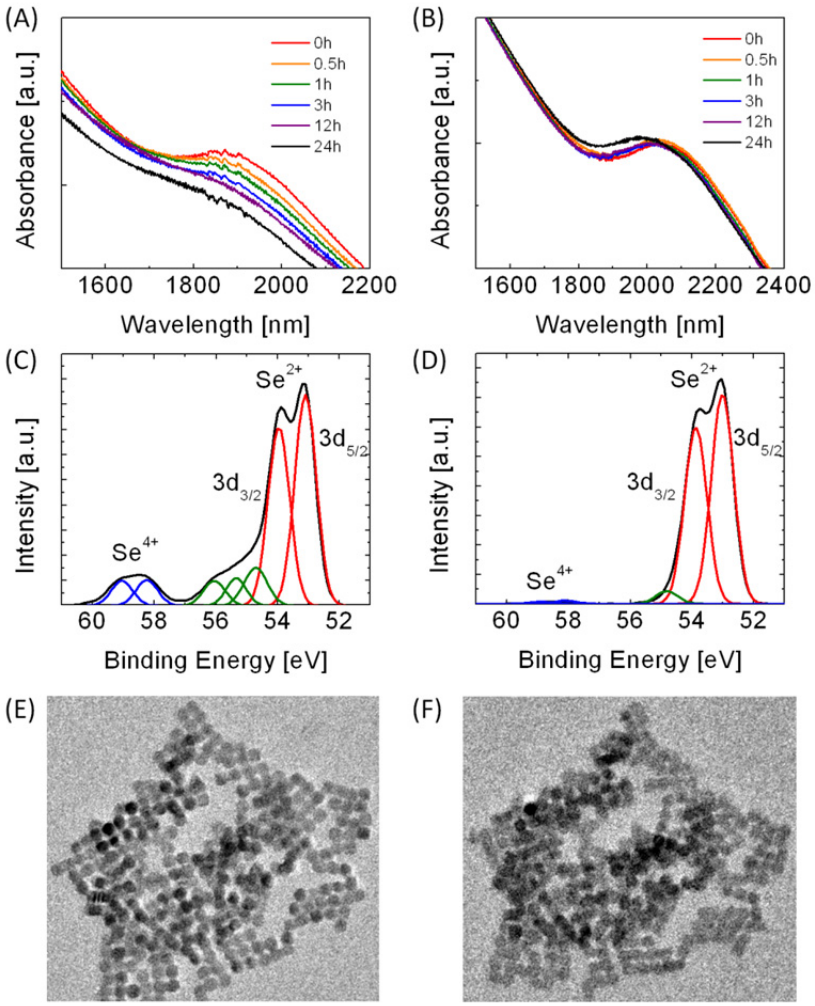

Figure 3.3 Absorption spectra of (A) Na_2Se treated and (B) subsequently $PbCl_2$ treated PbSe NC thin films as a function of exposure time to air. X-ray photoelectron spectroscopy of the Se 3d peak for (C) Na_2Se and (D) and subsequently $PbCl_2$ treated PbSe NC thin films. TEM images of Se-rich PbSe NC assemblies treated with Na_2Se, followed by air exposure for (E) 1min and (F) several days. Note these TEM images (E, F) are collected from the same region of the NC sample.

We expose chalcogen-rich and Pb-rich NC thin films to air and monitor the change in the first excitonic peak as a function of time to test their relative stability. In PbSe NC thin films, the first excitonic peak for Se-rich NCs becomes broader over time and disappears within 24 h [Figure 3.3(A)]. However Pb-rich NC thin films show much greater air stability, showing little change over time [Figure 3.3(B)]. The broadening upon chalcogenide treatment could have several explanations. First, the broader peak of chalcogen-rich NC thin films could be attributed to an Urbach tail that results from bare or oxidized chalcogen surfaces. Surface chalcogen atoms in non-stoichiometric NCs are known to create a number of midgap states.[25] When lead chalcogenide NCs are exposed to oxygen, surface Se is known to readily oxidize in comparison to surface S, generating trap states.[1,45] The combination of chalcogenide and $PbCl_2$ treatments creates a well-passivated NC surface, even in comparison to as-synthesized NCs, reducing chalcogen midgap states and sites for oxidation. Second, the broad first excitonic peak of chalcogen-rich NC surfaces, which further broadens and eventually disappears upon oxidation, could result from structural changes driven by the high energy and high oxygen sensitivity of the unligated, chalcogen-terminated NC surface. While oxygen prevents the fusion of NCs when NCs are passivated by oleic acid,[21] bare Se-terminated NCs without any capping ligands will oxidize and promote NC fusion to reduce surface energy.

We carry out XPS measurements to analyze the NC surface chemistry at each stage of treatment. While as-prepared NC samples show mostly Se $3d_{3/2}$ and $3d_{5/2}$ peaks with a very small amount of Se^{4+} peak, a substantial Se^{4+} peak is observed around 59 eV after Na_2Se treatment [Figure 3.3(C)]. This Se^{4+} peak is mainly ascribed to SeO_2 or

SeO_3^{2-}, suggesting a significant degree of surface oxidation.[29] A shoulder around the Se $3d_{3/2}$ peak also increases after Na_2Se treatment, consistent with bare Se atoms. However, after $PbCl_2$ treatment, both the Se^{4+} peak and the significant shoulder are not observed, resembling the spectra for oleic acid capped NCs [Figure 3.3(D)]. It should be noted that when transferring samples into the chamber for measurement, the samples are exposed to air for tens of minutes. Given the absence of capping ligands, NCs are oxidized significantly under air. However when $PbCl_2$ treatment is conducted right after Na_2Se treatment, the NCs are protected from oxygen by the Pb-rich surface and introduced oleylamine and chloride capping ligands.[46] Similarly, a significant shoulder around the Pb 4f peak due to PbO and $Pb(OH)_2$[29] is observed only for unligated, Se-rich PbSe NCs, further supporting the vulnerability to oxygen of chalcogen-terminated NCs.

Structural changes are observed in NC thin films over time upon air exposure and investigated using TEM and SAXS. The morphology of Se-rich NCs is seen to evolve in TEM images over several days, from more discrete to severely fused NC thin films [Figure 3.3 (E,F)]. SAXS patterns of air exposed, Se-rich NC thin film show a weak shoulder around $2\theta=1.25^{o}$, in contrast to subsequently $PbCl_2$ treated samples which show substantially sharper, distinct reflections at the same angle, indicative of individual NCs. S-rich PbSe NCs show a similar trend, but with a smaller loss in the reflection. Using the combination of XPS, TEM, SAXS and absorption measurements, we provide strong evidence that fusion of chalcogen-rich NC thin films occurs to reduce their high surface energy and is promoted by surface oxidation. However, we show $PbCl_2$ treatment

introduces a self-limiting, ligated Pb shell that protects the NC thin films from oxidation, stabilizing their structural, optical and (as shown below) electronic properties.

Carrier Density	Na_2Se treated Before $PbCl_2$	1h $PbCl_2$ treatment	6h $PbCl_2$ treatment	12h $PbCl_2$ treatment
C-V [cm^{-3}]	10^{18} to 10^{19} holes	3.3×10^{17} holes	4.2×10^{16} holes 1.0×10^{16} electrons	2.5×10^{17} electrons
Hall [cm^{-3}]	$4.0 \pm 1.2 \times 10^{18}$ holes	$4.8 \pm 1.5 \times 10^{16}$ holes	$1.6 \pm 0.3 \times 10^{16}$ holes	$3.0 \pm 0.8 \times 10^{15}$ holes $4.0 \pm 1.0 \times 10^{15}$ electrons

Table 3.2 Carrier concentration of Se-rich PbSe NC thin films before and as a function of the time of $PbCl_2$ treatment as measured by Capacitance-Voltage and Hall techniques.

3.3.2 Electronic Properties of Chalcogen-rich and Pb-rich Lead chalcogenide NCs.

The carrier statistics of lead chalcogenide NC thin films[8,25] are directly related to their stoichiometry as has been seen in polycrystalline thin films[47] and single crystals.[48] We measure the carrier densities for chalcogen-enriched and, as a function of $PbCl_2$ treatment time, Pb-enriched PbSe NC thin films using Capacitance-Voltage (C-V) and Hall measurements, as summarized in the Table II. Using C-V measurements, we calculate the carrier density by integrating the capacitance according to $Q = \int_{V_{TH}}^{V} C \, \mathrm{dV}$.[8,49,50] Se-rich or S-rich PbSe NC thin films show heavily doped and degenerate p-type behavior with very small gate modulation and threshold voltages exceeding 100 V, making it difficult to quantify the carrier density. Given the degenerate character, we assume thin film hole densities of 10^{18} to 10^{19} /cm^3. The high hole density is attributed to Se excess and oxidized surface Se atoms,[51–53] which have been shown experimentally[8] and theoretically[25] to introduce midgap[54,55] or Urbach tail states.[2,15,56,57] After 1 h of $PbCl_2$ treatment, there is a drastic change in carrier concentration. The heavily doped and degenerate p-type characteristics change to lightly doped p-type characteristics, and as treatment progresses in time and Pb ions are bound to surface Se atoms, the polarity changes from p-type *via* ambipolar to slightly n-type. It should be noted that most of the outer Pb shell is formed in one hour at 65 ºC and only a slight increase in the number of Pb atoms can change the polarity as they donate more electrons to the NCs through vacancy compensation.[48,58] Extra Pb (chalcogen) ions can be understood as introducing a chalcogen (Pb) vacancy, creating states near the conduction (valence) bands, raising (lowering) the Fermi Level.[48] Hall effect measurements show chalcogen-rich PbSe NC

thin film hole densities of 4.0 x $10^{18}/cm^3$. After the $PbCl_2$ treatment, the hole density decreases and the electron density increases, as seen by C-V measurement. We note that while the Hall and C-V data show the same trend with chalcogen and Pb enrichment, as the samples are enriched in Pb and their resistivity drops, the carrier densities differ quantitatively and the accuracy of the Hall data is limited.

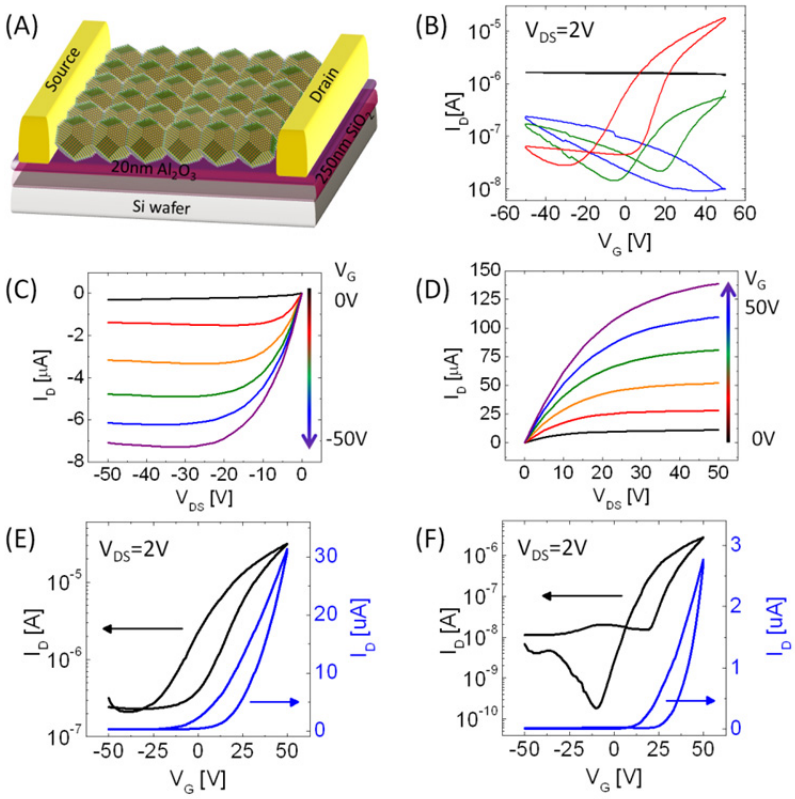

Figure 3.4 (A) Schematic of a PbE (E = S or Se) NC thin-film field effect transistor. (Note: The figure is not drawn to scale and the NC thin films comprise small ordered domains.) (B) Transfer curves of Na_2Se treated PbSe NCs before (black) and after $PbCl_2$ treatment for 1 h (blue), 6 h (green), and 12 h (red) at 65 ºC. (C) p-type output characteristics of a PbSe NC thin film FET treated with Na_2Se followed by 1 h of 10 mM $PbCl_2$ at 65 ºC. (D) n-type output characteristics of a PbSe NC thin film FET treated with Na_2Se followed by 12 h of $PbCl_2$ at 65 ºC. Output characteristics in the linear regime of (E) a PbSe NC FET treated with Na_2Se followed by 10 min with $PbCl_2$ at 95 ºC and (F) a PbS NC FET treated with Na_2S followed by 10 min with $PbCl_2$ at 95 ºC.

To understand the physics of charge transport and take advantage of the solution-based PS-cALD technique, we fabricate FETs. A heavily doped n-type Si wafer with a gate dielectric stack of SiO_2 and Al_2O_3 is coated by MPTS to reduce hysteresis[8] and improve NC adhesion [Figure 3.4(A)]. NCs are spincoated, followed by chalcogenide treatment or in combination with Pb-salt treatment, and metal electrodes are deposited. As seen in the transfer curves, Se-rich [Figure 3.4(B)] or S-rich PbSe NC thin films show degenerate p-type characteristics with almost no gate modulation and high conductivity, in agreement with the C-V measurements and a previous report studying Na_2S treated PbSe NC thin films by Law.[15] As Pb ions binds to surface Se atoms [or S atoms], the device characteristics dramatically change from heavily p-type, to lightly doped p-type, to ambipolar and finally to n-type. Similar to C-V measurements, the threshold voltage drastically shifts from large, positive through zero to negative potentials consistent with the Fermi energy shifting from very close to the valence band to midgap and towards the conduction band.[8] For example, in Figure 3.4(B), initially Na_2Se treated PbSe NC FETs show semi-metallic p-type behavior with a hole mobility of 7.5×10^{-3} cm^2/Vs [black curve]. After 1 h of $PbCl_2$ treatment [blue curve], the device shows p-type behavior with a hole mobility of 2.2×10^{-3} cm^2/Vs. Upon 6 h of $PbCl_2$ treatment [green curve], devices show ambipolar behavior with a hole mobility of 2.0×10^{-3} cm^2/Vs and an electron mobility of 1.4×10^{-1} cm^2/Vs. Longer 12 h $PbCl_2$ treatment yields n-type NC FETs with an electron mobility of 2.4 cm^2/Vs [red curve]. Devices treated with $PbCl_2$ for 12 h show a high electron mobility of 3.0 ± 1.5 cm^2/Vs, with best mobilities of 4.5 cm^2/Vs and I_{ON}/I_{OFF} of 10^2 to 10^3. We study the effects of the $PbCl_2$ reaction conditions of temperature, time and concentration on the device behavior. Similar n-type behavior and electron mobilities

of up to ~4.7 cm^2/Vs [Figure 3.4(E)] are achieved at higher temperatures and significantly shorter times such as 85 ^oC for 1 h or 95 ^oC for 10 min.

A series of control experiments are carried out to confirm the origin of the change in device polarity from p-type to n-type arises from Pb-enrichment and not from thermal history or ions introduced in the reaction. S and Se-rich PbSe NC FETs are (1) dipped in an oleylamine solution without $PbCl_2$ at 65 ºC for the same time, and result in unchanged, degenerate p-type FET behavior, characteristic of the chalcogen-rich NC thin films, (2) annealed under N_2 in the glove box overnight at 65 ºC, and similarly the NC FETs remain strongly p-type devices, and (3) as-synthesized NC FETs are exchanged with an alternate chloride using tetra butyl ammonium chloride (TBAC) to test the role of Cl^- passivation, reported to act as an n-type dopant.[11] TBAC treated PbSe NC FETs show ambipolar characteristics with electron mobilities < 0.1 cm^2/Vs, excluding significantly enhanced n-type characteristics originating from chloride passivation. While analytically the Pb-enriched NC thin films are more stable, electronic characterization in FET measurements show that they become increasingly p-doped upon air exposure.

We also measured the device behavior for Se-enriched PbSe NC FETs treated with $PbCl_2$ and varied the $PbCl_2$ concentration from 0.01 mM to 20 mM. The devices showed more p-type character at lower $PbCl_2$ concentrations, but at concentrations higher than 1 mM the n-type device behavior saturated. Note, all of the $PbCl_2$ treatments in our paper are at 10-20 mM concentrations, well above the saturation point. As the reaction is a function of temperature, time and concentration, we are able to control the carrier type,

concentration, mobility, density of states and Fermi level precisely by changing the reaction parameters.

Devices treated analogously with Na_2S or KHS and $PbCl_2$ show similar performance, with mobilities of 1.5±1cm^2/Vs. PbS NC FETs treated with Na_2S and $PbCl_2$ show electron mobilities of 0.5±0.3cm^2/Vs [Figure 3.4(F)]. It should be mentioned that this high mobility for PbS NC FETs is achieved while the first excitonic peak gets narrowed, not broadened, resulting from well-passivated NC surfaces. We attribute this enhanced charge transport to the formation of a passivating shell as well as strong electronic coupling. The core/shell NC structure is typically introduced to protect the NC core,[27,28,59] but post ligand exchange employed in device integration unavoidably creates defect states on the NC surface.[31] In PS-cALD process, however, we introduce the self-limited shell after NC deposition and ligand exchange, creating the well-passivated NC surface.

Our recent report[8] and the Law group's report[15] of lead chalcogenide NC FETs with electron mobilities above 5 cm^2/Vs highlight the great potential of lead chalcogenide NC thin films for applications. However, these high performance devices are realized through the use of more expensive vacuum deposition techniques of metal evaporation and oxide atomic layer deposition, respectively. Here, in this work, we introduce a wet-chemical route to realize similarly high-performance devices from quantum-confined, NC-based thin films compatible with desirable low-cost, solution-based processing.

3.4 Conclusions

In conclusion, we introduce a low-cost, solution-based PS-cALD technique, consisting of stepwise chalcogenide and $PbCl_2$ treatments, to tailor the stoichiometry and therefore the electronic properties of lead chalcogenide NC thin films. We carry out PS-cALD for NC thin films integrated in solid state device structures and directly relate NC thin film structure and stoichiometry to device performance. Chalcogen-rich NC surfaces have high surface energy and are unstable, driving structural transformation of the NC thin films into ordered and interconnected assemblies, but electronically forming p-type materials with an unfavorable density of trap states. These disadvantages are overcome by $PbCl_2$ treatment. The Pb-rich and ligated surface structurally and oxidatively stabilizes the NC thin films, reducing the density of trap states and n-doping the films, dramatically enhancing electron transport. This PS-cALD method is a general technique that can be extended to other NC, nanowire or thin film compositions and the use of different treatments to chemically design materials properties for a wide range of applications.

3.5 References

(1) Talapin, D.; Murray, C. B. *Science* **2005**, *310*, 86–89.

(2) Tang, J.; Kemp, K. W.; Hoogland, S.; Jeong, K. S.; Liu, H.;Levina, L.; Furukawa, M.; Wang, X.; Debnath, R.; Cha, D.; *et al., Nat. Mater.* **2011**, *10*, 765–771.

(3) Ip, A. H.; Thon, S. M.; Hoogland, S.; Voznyy, O.; Zhitomirsky, D.; Debnath, R.; Levina, L.; Rollny, L. R.; Carey, G. H.; Fischer, A.; *et al., Nat. Nanotechnol.* **2012**, *7*, 577–582.

(4) Tang, J.; Liu, H.; Zhitomirsky, D.; Hoogland, S.; Wang, X.; Furukawa, M.; Levina, L.; Sargent, E. H. *Nano Lett.* **2012**, *12*, 4889–4894.

(5) Wang, R. Y.; Feser, J. P.; Lee, J.-S.; Talapin, D. V.; Segalman, R.; Majumdar, A. *Nano Lett.* **2008**, *8*, 2283–2288.

(6) Engel, J. H.; Alivisatos, A. P. **2013**. *Chem. Mater.* **2014**, 26, 153-162.

(7) Luther, J. M.; Pietryga, J. M. *ACS nano* **2013**, *7*, 1845–1849.

(8) Oh, S. J.; Berry, N. E.; Choi, J.-H.; Gaulding, E. A.; Paik, T.; Hong, S.-H.; Murray, C. B.; Kagan, C. R. *ACS nano* **2013**, *7*, 2413–2421.

(9) Mocatta, D.; Cohen, G.; Schattner, J.; Millo, O.; Rabani, E.; Banin, U. *Science* **2011**, *332*, 77–81.

(10) Choi, J.-H.; Fafarman, A. T.; Oh, S. J.; Ko, D.-K.; Kim, D. K.; Diroll, B. T.; Muramoto, S.; Gillen, J. G.; Murray, C. B.; Kagan, C. R. *Nano Lett.* **2012**, *12*, 2631–2638.

(11) Zhitomirsky, D.; Furukawa, M.; Tang, J.; Stadler, P.; Hoogland, S.; Voznyy, O.; Liu, H.; Sargent, E. H. *Adv. Mater.* **2012**, 24, 6181-6185.

(12) Yu, D.; Wang, C.; Guyot-Sionnest, P. *Science* **2003**, *300*, 1277–1280.

(13) Koh, W.; Koposov, A. Y.; Stewart, J. T.; Pal, B. N.; Robel, I.; Pietryga, J. M.; Klimov, V. I. *Sci. Rep.* **2013**, *3*, 2004.

(14) Liu, Y.; Gibbs, M.; Perkins, C. L.; Tolentino, J.; Zarghami, M. H.; Bustamante, J.; Law, M. *Nano Lett.* **2011**, *11*, 5349–5355.

(15) Liu, Y.; Tolentino, J.; Gibbs, M.; Ihly, R.; Perkins, C. L.; Liu, Y.; Crawford, N.; Hemminger, J. C.; Law, M. *Nano Lett.* **2013**, *13*, 1578–1587.

(16) Lee, J.; Kovalenko, M.; Huang, J.; Chung, D. S.; Talapin, D. V. *Nat. Nanotechnol.* **2011**, *6*, 348–352.

(17) Choi, J.; Oh, S. J.; Lai, Y.; Kim, D.; Zhao, T.; Fafarman, A.T.; Diroll, B. T.; Murray, C. B; Kagan, C. R. *ACS nano* **2013**, 8275–8283.

(18) Murray, C.; Kagan, C.; Bawendi, M. *Science* **1995**, *270*, 1335–1338.

(19) Dong, A.; Chen, J.; Oh, S. J.; Koh, W.; Xiu, F.; Ye, X.; Ko, D.; Wang, K. L.; Kagan, C. R.; Murray, C. B. *Nano lett.* **2011**, *11*, 841–846.

(20) Dong, A.; Jiao, Y.; Milliron, D. J. *ACS nano* **2013**. 7, 10978-10984

(21) Baumgardner, W. J.; Whitham, K.; Hanrath, T. *Nano Lett.* **2013**. *13*, 3225–3231

(22) Evers, W. H.; Goris, B.; Bals, S.; Casavola, M.; de Graaf, J.; van Roij, R.; Dijkstra, M.; Vanmaekelbergh, D. *Nano Lett.* **2013**, *13*, 2317–2323.

(23) Urban, J. J.; Talapin, D. V.; Shevchenko, E. V.; Kagan, C. R.; Murray, C. B. *Nat. Mater.* **2007**, *6*, 115–121.

(24) Shabaev, A.; Efros, A. L.; Efros, A. L. *Nano Lett.* **2013**. *13*, 5454–5461

(25) Kim, D.; Kim, D.-H.; Lee, J.-H.; Grossman, J. C. *Phys. Rev. Lett.* **2013**, *110*, 196802

(26) Hughes, B. K.; Ruddy, D. a; Blackburn, J. L.; Smith, D. K.; Bergren, M. R.; Nozik, A. J.; Johnson, J. C.; Beard, M. C. *ACS Nano* **2012**, *6*, 5498–5506.(27) Li, J.; Wang, Y.; Guo, W. *J. Am. Chem. Soc.* **2003**, *125*, 12567–12575

(28) Jasieniak, J.; Mulvaney, P. *J. Am. Chem. Soc.* **2007**, *129*, 2841–2848.

(29) Luther, J. M.; Law, M.; Song, Q.; Perkins, C. L.; Beard, M. C.; Nozik, A. J. *ACS nano* **2008**, *2*, 271–280.

(30) Ma, W.; Luther, J.; Zheng, H.; Wu, Y.; Alivisatos, A. *Nano Lett.* **2009**, *9*, 1699–1703.

(31) Thon, S.; Ip, A.; Voznyy, O.; Levina, L. Role of Bond Adaptability in the Passivation of Colloidal Quantum Dot Solids. *ACS nano* **2013**, *7*, 7680–7688.

(32) Cho, K.-S.; Talapin, D. V.; Gaschler, W.; Murray, C. B. *J. Am. Chem. Soc.* **2005**, *127*, 7140–7147.

(33) Schliehe, C.; Juarez, B. H.; Pelletier, M.; Jander, S.; Greshnykh, D.; Nagel, M.; Meyer, A.; Foerster, S.; Kornowski, A.; Klinke, C.; Weller, H. *Science* **2010**, *329*, 550–553.

(34) Koh, W.; Bartnik, A. C.; Wise, F. W.; Murray, C. B. *J. Am. Chem. Soc.* **2010**, *132*, 3909–3913.

(35) Yu, W. W.; Falkner, J. C.; Shih, B. S.; Colvin, V. L. *Chem. Mater.* **2004**, *35*, 3318–3322.

(36) Hines, M. a.; Scholes, G. D. *Adv. Mater.* **2003**, *15*, 1844–1849.

(37) Nag, A.; Kovalenko, M.; Lee, J. *J. Am. Chem. Soc.* **2011**, *133*, 10612–10620.

(38) Moreels, I.; Lambert, K.; Muynck, D. D. *Chem. Mater.* **2007**, *19*, 6101–6106.

(39) Zhang, H.; Hu, B.; Sun, L.; Hovden, R.; Wise, F. W.; Muller, D. a; Robinson, R. D. *Nano Lett.* **2011**, *11*, 5356–5361.

(40) Bealing, C. R.; Baumgardner, W. J.; Choi, J. J.; Hanrath, T.; Hennig, R. G. *ACS nano* **2012**, *6*, 2118–2127.

(41) Argeri, M.; Fraccarollo, A. *J. Phys. Chem. C* **2011**, *115*, 11382–11389.

(42) Choi, J. J.; Bealing, C. R.; Bian, K.; Hughes, K. J.; Zhang, W.; Smilgies, D.-M.; Hennig, R. G.; Engstrom, J. R.; Hanrath, T. *J. Am. Chem. Soc.* **2011**, *133*, 3131–8.

(43) Fang, C.; van Huis, M. a; Vanmaekelbergh, D.; Zandbergen, H. W. *ACS nano* **2010**, *4*, 211–218.

(44) Moreels, I.; Fritzinger, B.; Martins, J. C.; Hens, Z. *J. Am. Chem. Soc.* **2008**, *130*, 15081–15086.

(45) Steckel, J. S.; Coe-Sullivan, S.; Bulović, V.; Bawendi, M. G. *Adv. Mater.* **2003**, *15*, 1862–1866.

(46) Bae, W. K.; Joo, J.; Padilha, L. a; Won, J.; Lee, D. C.; Lin, Q.; Koh, W.; Luo, H.; Klimov, V. I.; Pietryga, J. M. *J. Am. Chem. Soc.* **2012**, *134*, 20160–20168.

(47) Maier, H.; Daniel, D. R.; Preier, H. *J. Cryst. Growth* **1976**, *35*, 121–126.

(48) Allgaier, R. S.; Scanlon, W. W. *Phys. Rev.* **1958**, *111*, 1029.

(49) Kang, M. S.; Sahu, A.; Norris, D. J.; Frisbie, C. D. *Nano Lett.* **2011**, *11*, 3887–3892.

(50) Goldberger, J.; Sirbuly, D. Yan, H.; Yang, P. *J. Phys. Chem. B* **2005**, *109*, 9–14.

(51) Leschkies, K. S.; Kang, M. S.; Aydil, E. S.; Norris, D. J. *J. Phys. Chem. C* **2010**, *114*, 9988–9996.

(52) Oh, S. J.; Kim, D. K.; Kagan, C. R. *ACS nano* **2012**, *6*, 4328–4334.

(53) Kim, D. K.; Vemulkar, T. R.; Oh, S. J.; Koh, W.-K.; Murray, C. B.; Kagan, C. R. *ACS nano* **2011**, *5*, 3230–3236.

(54) Nagpal, P.; Klimov, V. I. *Nat. commun.***2011**, *2*, 486.

(55) Tang, J.; Sargent, E. *Adv. Mater.* **2011**, *23*, 12–29.

(56) Gao, J.; Johnson, J. *ACS nano* **2012**, *6*, 3292–3303.

(57) Erslev, P.; Chen, H.; Gao, J.; Beard, M. *Phys. Rev. B* **2012**. *86*, 155313-1

(58) Kim, D. K.; Fafarman, A. T.; Diroll, B. T.; Chan, S. H.; Gordon, T. R.; Murray, C. B.; Kagan, C. R. *ACS nano* **2013**, *7*, 8760–8770.

(59) Ithurria, S.; Talapin, D. *J. Am. Chem. Soc.* **2012**, *134*, 18585–18589

CHAPTER 4 Charge Injection and Transport in PbSe Nanocrystal Thin Film Solids

4.1 Introduction

Lead chalcogenide nanocrystals (NCs) have been shown to be promising candidates for optoelectronic,[1,2] electronic[3] and thermoelectric[4] applications, due to their unique size-dependent properties and solution processability. While these three applications have different physical mechanisms and may require different approaches to enhance device performance, the one common and important mechanism to be investigated is charge transport. Indeed, the actual charge or current flowing in devices arises from charge injection and charge transport. The term, charge transport, is often vaguely used to indicate the total charge current flow. In this Chapter, we distinctively define charge injection and charge transport as the charge flow between metal-NC and within NC thin films, respectively. Understanding charge injection and transport in NC thin films and devices allows us to design the materials and devices for different applications.

Charge transport in lead chalcogenide NC thin film electronic devices has been extensively studied for both scientific interest and technological application.[3,5–11] However, there have been few studies probing the mechanism of charge injection. This is largely because conductive NC thin films with high mobility charge transport had not been achieved until recently,[8,9,12] and because barriers to charge injection are not as evident in low bandgap, lead chalcogenide materials. Here, we probe charge injection and

transport in lead chalcogenide NC thin film devices by using the field-effect transistor (FET) geometry [Figure 4.1]. We engineer the NC-metal interface as well as the NC surface and achieve the highest conductivity among semiconducting NC devices. Fermi level pinning effect is observed, consistent with previous literature reports,[13,14] and can dominate the charge carrier behavior. We reveal that both charge injection and transport play important roles in fabricating high performance NC electronic devices.

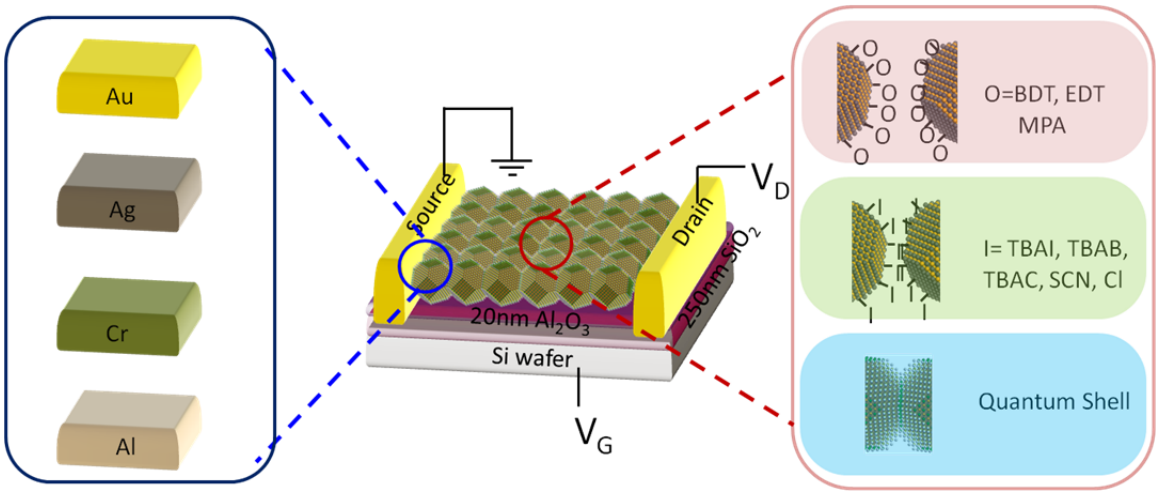

Figure 4.1 Schematic of PbSe NC field-effect transistors with different contact metallurgy (left) and different ligand chemistries (right).

We vary the NC ligand chemistry and the contact metallurgy to separate the mechanisms of charge transport and charge injection in NC devices. Ligands on the surface of NCs have mainly two roles in influencing the electronic properties of NCs and their thin films: 1) Ligands may affect the NCs by creating or passivating midgap and shallow trap states or by donating or accepting electrons or holes.[3,15,16] 2) Ligands also alter the electronic properties of NC thin films as the ligand length determines the interparticle distance between adjacent NCs and therefore affects the film conductivity.[6]

Metal electrodes introduced in constructing devices control the charge injection mechanism. The work function of the metal defines the barrier height for electron and hole injection. In ideal Mott-Schottky theory, the barrier height for electron injection is assumed to be the difference between the metal work function and the semiconductor electron affinity.[17] If Fermi level pinning occurs, the barrier for electron injection becomes completely or relatively independent of metal work function. In cases of Mott-Schottky and relative Fermi level pinning, a low (high) work function metal is favorable for electron (hole) injection as it presents a low barrier for electron (hole) injection.[18]

4.2 Experiment details

6 nm PbSe NCs are synthesized as previously reported.[8] To construct FETs, heavily n-doped silicon wafers with 20 nm of Al_2O_3 deposited by atomic layer deposition on top of thermally grown 250 nm SiO_2 are used as substrates. For two-terminal conductivity measurements, quartz discs are used. NCs are deposited by spincoating to

form 20 -30 nm thin films on FET and conductivity substrates. All the substrates are treated with mercaptopropyl trimethoxysilane (MPTS) to improve the NC adhesion and reduce device hysteresis.[8] After NC film deposition, the substrates are immersed in a solution containing the following investigated ligands: 10 mM ethanedithiol (EDT) in acetonitrile for 2 min, 10 mM mercaptopropionic acid (MPA) in methanol for 30 sec, 1 mM ammonium thiocyanate (NH_4SCN) in methanol for 10 s, 10 mM tetrabutyl ammonium iodine (TBAI) in methanol for 10 s. Devices are washed three times after treatment with the parent solvent used in the exchange. To investigate source and drain electrodes varying in their work function, Au (5.1 eV), Ag (4.7 eV), Cr (4.5e V) and Al (4.2e V) are deposited by thermal evaporation. Top contact devices are formed by depositing the metal after NC film deposition and ligand exchange, whereas bottom contact devices are fabricated by depositing metal electrodes just prior to spincoating the NCs.

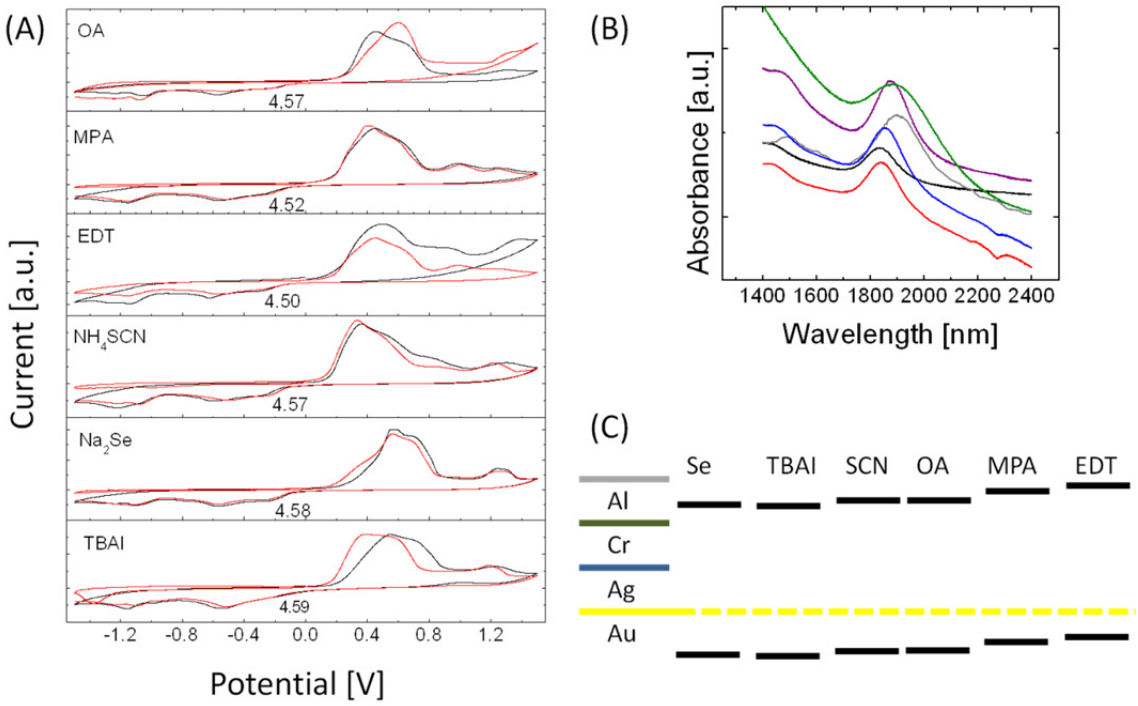

Figure 4.2 (A) Cyclic voltammetry measurements (red : forward scan, black : reverse scan) and (B) absorption spectra for 6 nm PbSe NCs exchanged with (black) oleic acid, (red) MPA, (blue) EDT, (purple), SCN (grey), Na_2Se (green). (C) Band diagrams constructed from cyclic voltammetry and absorption measurements for a few representative ligand-exchanged PbSe NC thin films in comparison to the work function for Au (Ag, Cr, and Al are also shown on the left side).

4.3 Results and Discussions

4.3.1 Band diagram of PbSe NC FETs

Cyclic voltammetry (CV) in combination with absorption spectroscopy are used to characterize the electronic structure of PbSe NC thin films. Figure 4.2 (A) shows CV data for 6 representative ligands. Ferrocene is used as a reference sample and forward and reverse scanning are collected to rule out the possibility of hysteresis. The first peak found around ~-0.2eV (around ~ 4.6eV from the vacuum level) corresponds to the conduction band (CB), in good agreement with literature report.[19] We hypothesize that the second and third peaks found correspond to the second and third CB levels. The peak found at +0.3-0.6 eV is assumed to be the valence band (VB).[19]

One noticeable phenomenon is that the peak position of valence band strongly depends on the NC film exposure, especially to O_2. When the sample is measured 30 min after sample fabrication in the glovebox with an oxygen level of ~10 ppm, the peak shifts to more positive potentials, i.e. suggesting the VB position changes from ~5 eV to as much as ~5.5eV. When the sample is exposed to air, it shows a more dramatic change in the same direction. A significant band formation below the VB is explicitly shown, while there is little change in the CB (data not shown here). PbSe NCs are known to be affected by even the low oxygen partial pressures found in a nitrogen glove box, as surface oxygen creates acceptor states and thereby dopes the NCs p-type. Larger oxygen exposure in air creates states both near and below the valence band, degenerately doping the semiconductor.[20,21]

As the position of the VB is unstable and strongly affected by the NC environment, we calculate the energy of the VB by subtracting the optical bandgap measured using absorption spectroscopy from the energy of the CB evaluated from cyclic voltammetry.[19] Figure 4.2 (B) shows the optical bandgap of PbSe NC thin films measured for 6 representative ligands. All the ligand exchange processes show a red-shift, mostly resulting from increased electronic coupling.[3,8,9,22–24] NC thin films with different ligands show some variation in both CV and absorption spectroscopy, but no significant differences are seen in the position of the CB and VB [Figure 4.3 (C)]

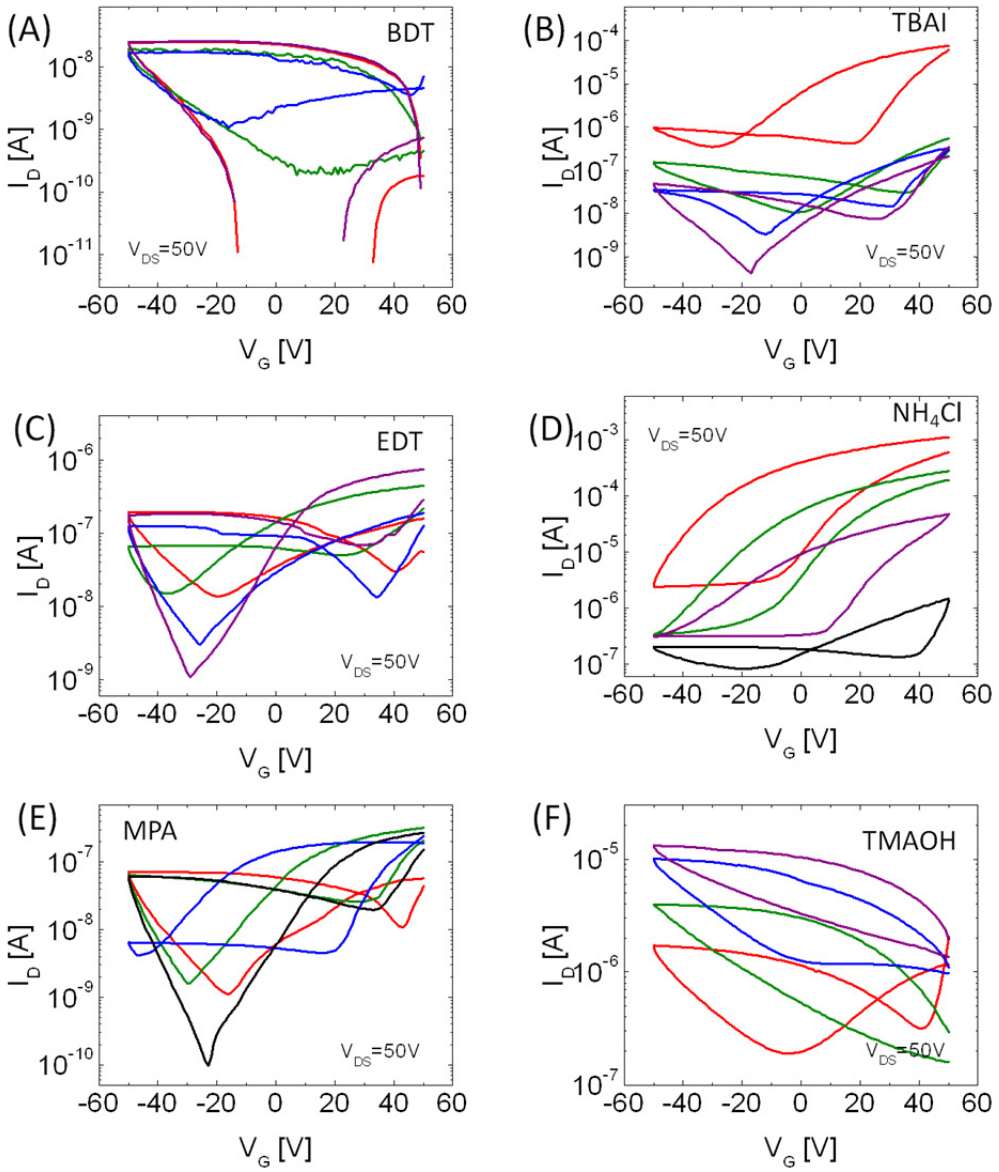

Figure 4.3 PbSe NCs FETs treated with (A) BDT, (B) TBAI, (C) EDT, (D), NH_4Cl, (E) MPA and (F) TMAOH, with (red) Al, (green) Cr, (blue) Ag, (purple) Au.

4.3.2 Charge injection and transport at room temperature

Representative transfer characteristics for PbSe NC thin film FETs with various ligands are shown in Figure 4.3. All the electrical measurement are carried out 1 h after metal deposition, unless specified, as will be described later. One noticeable phenomenon is that for relatively long organic ligands such as EDT,[13,24,25] BDT,[26,27] and MPA,[1,28] the FET characteristics show low current levels and are not significantly affected by the selection of contact metal. These NC FETs also show ambipolar characteristics with large hysteresis. The FET with BDT shows the lowest conductivity, the FET with and MPA and EDT show slightly higher and similar conductivity.

For short inorganic halide ligands such as tetrabutyl ammonium iodine (TBAI),[16] ammonium chloride (NH_4Cl), and tetra methyl ammonium hydroxide (TMAOH),[29] FET characteristic show a strong dependence on metal work function. As reported, the halides TBAI, TBAB, and TBAC bind to surface lead atoms and donate an electron to the NC surface. As expected, low work function metals shows high electron currents for halogen-doped NC thin films. As the contact metal changes from Al to Cr, Ag and Au, the current decreases. This current and effective mobility decrease results from limited charge injection.

As reported, TMAOH acts as a p-dopant.[29] TMAOH treated PbSe NC thin film FETs shows p-type behavior, and as expected, Au contacts show strong p-type with high current, but as we lower the work function by changing the metal electrodes to Ag, Cr, and Al, the current level decreases. The device with Al electrodes shows ambipolar behavior. In the ambipolar device, electrons can be easily injected with the Al contact,

but mobile electron densities are small in p-type TMAOH treated PbSe NC thin film. Even if there are many mobile holes in the NC thin film channel, the hole current is limited by a large barrier to injection due to the low work function of the contact. These result in both electron and hole limited, ambipolar behavior of TMAOH treated PbSe NC FETs with Al contacts.

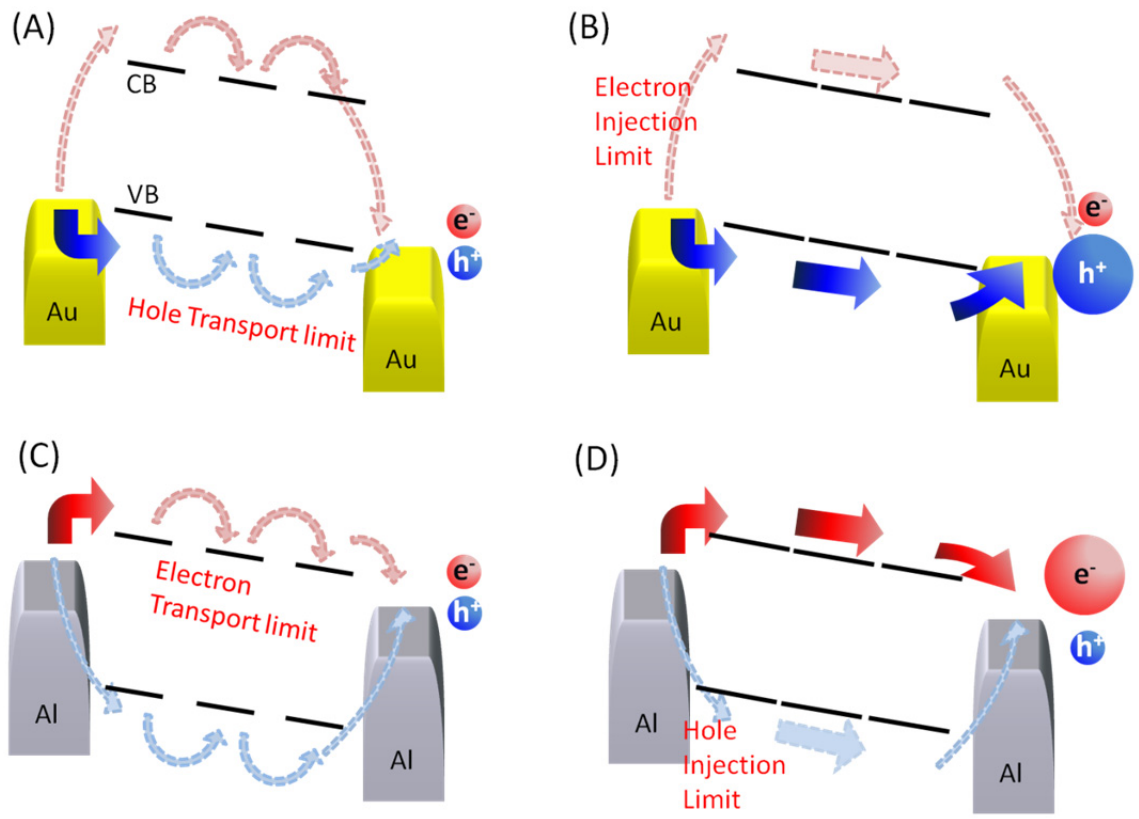

Figure 4.4 Band diagram depicting charge injection and transport in PbSe NC thin films with (A) long and (B) short ligands for FETs fabricated with high work function Au contacts and with (C) long and (D) short ligands for FETs fabricated with low work function Al contacts.

From our observations, we conclude that for PbSe NC thin films with long organic ligands, charge transport limits the device current due to the relatively large interparticle distance [Figure 4.4 (A, C)]. Carrier hopping rates from NC to NC are a function of interparticle spacing.[30] Even if electrons (holes) can be readily injected from low (high) work function electrodes, the mobility of charge carriers is limited.

However, in short inorganic ligands, the hopping rate is high due to the reduced or nearly removed interparticle spacing. This can even lead to a metal-to-insulator transition, as will be discussed. From this point, an inappropriately chosen metal can limit the device current. For example, the electron current is limited by injection at the semiconductor-metal contact for n-type PbSe NC thin films with Au metal contact, while hole current is limited in the channel [Figure 4.4 (B, D)].

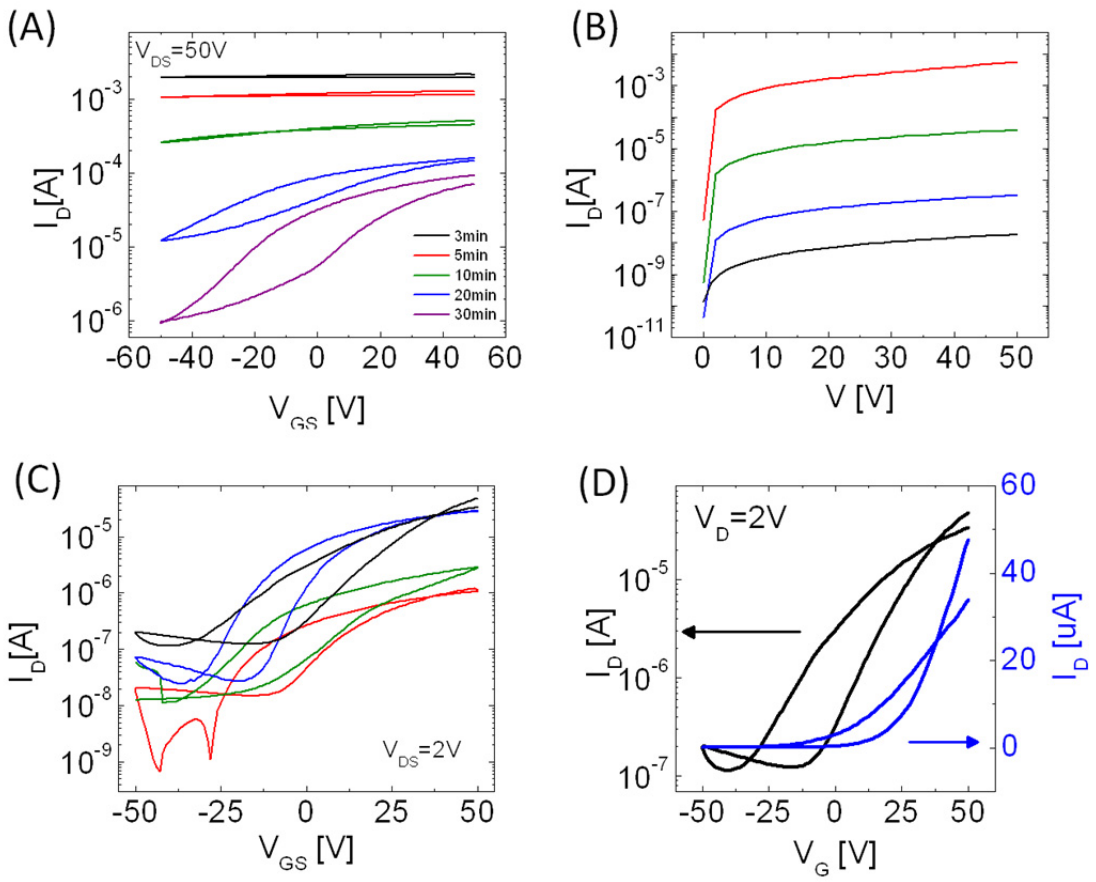

Figure 4.5 (A) PbSe NC FETs treated with TBAI with bottom contact Al electrodes as a function of time in the nitrogen glovebox with an oxygen level of ~1ppm. (B) Conductivity of PbSe NC thin films with (black) MPA and (blue) SCN, (green) SCN followed by $PbCl_2$ with Au contact, (red) SCN followed by $PbCl_2$ with Al contact,. (C) PbSe NC FETs with (red) TBAI, (green) NH_4Cl, (blue) Na_2Se and $PbCl_2$, (black) SCN and $PbCl_2$ with Au contact. (D) PbSe NC FETs with SCN and $PbCl_2$ with Au contact.

4.3.3 Conductivity and mobility of PbSe NC thin film solids

It should be noted here that the short-ligand treated NC thin film with low work function metals show unstable characteristics. It initially shows very high conductance, but degrades within an hour in the nitrogen glovebox [Figure 4.5 (A)]. The FET characteristics change from semi-metallic, degenerately doped, n-type behavior to semiconducting n-type behavior. However, the long-ligand treated NC thin films with low Φ metals do not show this behavior, as they do not show the metal dependent characteristics. Therefore, we attribute this effect to the degradation of the interface between metal and semiconductor. This is supported by the previous studies reporting that Al contacts to PbS NC thin films shows dramatic degradation. We believe that small amounts of oxygen can affect the interface of Al and PbSe NCs as both Al and PbSe are highly oxygen sensitive. We hypothesize that this interfacial change can modify the effective work function and induce by Fermi level pinning (described further below). The mechanistic study to demonstrate Fermi level pinning is ongoing in our group.[13,14]

We plot the conductivity of PbSe NC thin films for different metals and ligands. The combination of n-type FETs first SCN treated and then $PbCl_2$ treated with a low workfunction metal, namely Al, shows unusually high conductance of ~10 S/cm [Figure 4.5 (B)]. The conductance is close to or one order lower than the conductivity of bulk single crystalline n-type PbSe of 70~1000 S/cm.[31] This conductivity is ~6 orders higher than MPA-treated PbSe NC thin films which are known to be 5-8 orders higher in conductivity than OA capped PbSe NC thin films. When SCN and $PbCl_2$ treated PbSe NC thin films are combined with Au metals, the conductivity decreases by two orders. It

should be emphasized that the FET characteristics and conductivity of these NC thin films are significantly affected by metal work function, similar to nanowire, CNT, graphene or many other conventional semiconductors. The recent developments of ligand exchange chemistries and surface engineering of NC thin films enable transport in NC thin films to be comparable to the charge injection process at the metal-NCs junction properties.

While the n-type NC thin films with Al contacts show degenerate behavior, they show n-type semiconducting properties with high I_{ON}/I_{OFF} and mobility, when they are contacted by Au electrodes. This behavior is further achieved by gate-induced Schottky barrier modulation.[36] In addition, Au contact devices show significantly more stable operation, further indicating the important role of the metal-semiconductor junction. We plot the transfer characteristics of NC thin film FETs for various n-type ligands and for Au contacts in Figure 4.5 (C). The mobility of SCN or Se followed by $PbCl_2$ treated NC device, which is solely fabricated by solution based techniques, shows up to electron mobilities of 7 cm^2/Vs [Figure 4.5 (D)] or 3 cm^2/Vs, respectively, comparable to the highest reported mobility. We can control the electronic properties of NC thin film devices from that of highly conductivity metals to that of high mobility semiconductors, using desirable metals and ligands.

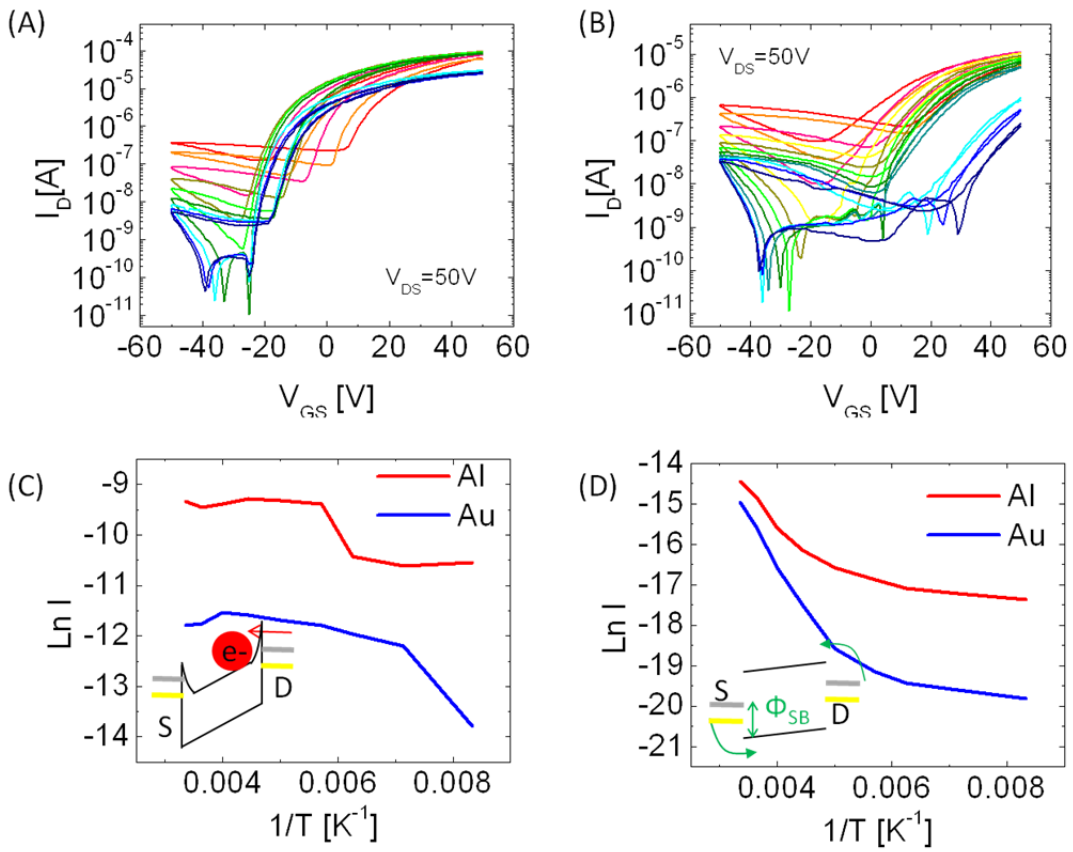

Figure 4.6. Temperature dependent FET measurements of PbSe NC thin films treated with TBAI and contacted by (A) Al and (B) Au electrodes. Temperature dependent electrical measurement of current (C) in the electron accumulation regime with V_G=50V, and (D) in the off-state with VG~-20V.

4.3.4 Variable temperature charge injection study

We conduct temperature dependent FET measurements to explore the carrier behavior at the metal-NC interface and within the NC thin films. Representative transfer characteristics between 77 K and 298 K for PbSe NC thin film FETs treated with TBAI are shown in Figure 4.6. As we mentioned, FETs with Al contacts show high electron currents and low hole currents due to the small barrier to electron injection [Figure 4.6 (B)]. In comparison, FETs with Au contacts show relatively lower electron currents and higher hole currents [Figure 4.6 (A)]. With the Al contact, the I_{ON}/I_{OFF} increases from 10^3 at room temperature to ~10^6-10^7 at low temperature. The electron current [Figure 4.6 (C)], off-current [Figure 4.6 (D)], and hole current (not shown here) are plotted as a function of temperature for FETs with Al and Au contacts. While charge transport and injection are both a function of temperature, the different slope between the Al and Au contacted devices with the same TBAI treatment enables us to extract the effective metal work function difference. Electron current is measured at $V_G = 50$ V where the strong gate bias pulls down the band and thins the barriers to allow electron tunneling and accumulation. Therefore the different amount of charge injection between Au and Al contacts can be understood as the different tunneling height. The barrier height for tunneling is calculated as ~35meV between Au and Al contacted FETs. The off current is defined as the minimum current in gate voltage between V_G=-50V-50V. At the off current, with the absence of strong bias, the electrons are injected by thermionic emission. In this regime, the effective metal work function difference of Au and Al are extracted as 90 meV, indicating the relative Fermi level pinning. Note that the actual

work function difference between gold and aluminum is 900 meV. The small difference of 90 meV is attributed to the Fermi level pinning. Fermi level pinning has been found in lead chalcogenide nanostructures with metal contacts, and is consistent the results for lead chalcogenide NC thin films showing the effective work function difference between Ca and Au was found to be 150meV while the actual difference is ~2.3eV.[13]

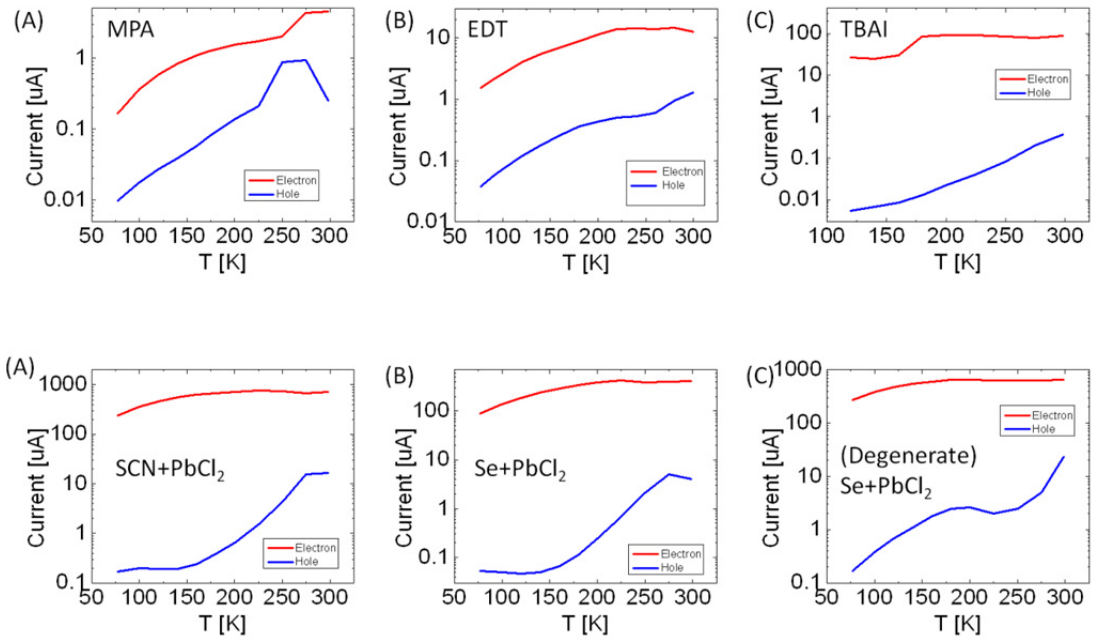

Figure 4.7. Temperature-dependent electron and hole currents for PbSe NC FETs with Au contacts treated with (A) MPA, (B) EDT, and with Al contacts treated with (C) TBAI, (D) SCN and $PbCl_2$ and Se and $PbCl_2$ for (E) short and (F) long treatment times.

4.3.5 Variable temperautre charge transport study

Last, the temperature-dependent charge transport characteristics are investigated. The electron and hole currents of NC thin films with different ligands are plotted [Figure 4.7]. For EDT and MPA, Au electrodes are used. For the n-type ligands of TBAI, SCN and PbCl2, Se and PbCl2, Al electrodes are used. In MPA and EDT treated NC thin films [Figure 4.7 (A,B)], the electron and hole conductance decreases as temperature decreases. The temperature dependent conductance follows general thermally activated or nearest neighbor hopping (NNH) mechanisms with the form:[5,30]

$$\sigma = \sigma_0 exp\left[(-\mathrm{E_a}/\mathrm{k_B T})^{\mathrm{b}}\right]$$

where b=1 (for NNH) and E_a = 25 meV. This agrees well with the previous studies[5] of PbSe NC FETs at temperatures between 225 K and 77 K.

However, for n-type ligands [Figure 4.7 (C, D, E, and F)], the electron conductance is rather constant over large temperature ranges, indicative of a transition from hopping to band-like transport. These NCs are actually touching together and in some cases fused together, but still show quantum confinement effects[12,32] However, this fused structure does not guarantee the negative temperature coefficient of conductance. For example, fused p-type NCs treated with chalcogens (S or Se) and contacted using Au,do not show this behavior. This is achieved by 1) strong electronic coupling by greatly reducing the interparticle distance and even fusing NC structures, 2) reduced Anderson localization achieved in short-range ordered NC films found for chalcogen and SCN treatments, 3) reduced surface trap states through $PbCl_2$ passivation, and 4) reduced

barrier height and increased charge injection by band alignment of the Fermi level of NC thin films and the work function of metal contacts. However, in the same structures, hole conductance decreases dramatically, mostly due to the lower hole density that cannot effectively fill the traps and high Schottky barriers.

4.4 Conclusion

In conclusion, we investigate the charge transport and charge injection of PbSe NC FETs, and reveal that both mechanisms play an important role in fabricating NC electronic devices. We demonstrate very high high conductance and high mobility PbSe NC thin film FETs using different contact metallurgy. Fermi level pinning is observed at the metal-semiconductor junction and it can also dominate the device performance. We emphasize that as recent developments in ligand chemistry enhances charge transport in NC thin films, the metal-semiconductor junction should also be carefully considered. This study provides important insight on the effect of ligand chemistry and metallurgy in the design of high performance electronic devices.

References

(1) Ip, A. H. et al., Amassian, A.; Sargent, E. H. *Nat. Nanotechnol.* **2012**, *7*, 577–582.

(2) Tang, J. et al., *Nat. Mater.* **2011**, *10*, 765–771.

(3) Talapin, D. V; Murray, C. B. *Science* **2005**, *310*, 86–89.

(4) Wang, R. Y.; Feser, J. P.; Lee, J.-S.; Talapin, D. V; Segalman, R.; Majumdar, A. *Nano Lett.* **2008**, *8*, 2283–2288.

(5) Kang, M. S.; Sahu, A.; Norris, D. J.; Frisbie, C. D. *Nano Lett.* **2011**, *11*, 3887–3892.

(6) Liu, Y.; Gibbs, M.; Puthussery, J.; Gaik, S. *Nano Lett.* **2010**, *10*, 1960–1969.

(7) Mentzel, T.; Porter, V.; Geyer, S.; MacLean, K.; Bawendi, M.; Kastner, M. *Phys. Rev. B* **2008**, *77*, 1–8.

(8) Oh, S. J.; Berry, N. E.; Choi, J.-H.; Gaulding, E. A.; Paik, T.; Hong, S.-H.; Murray, C. B.; Kagan, C. R. *ACS Nano* **2013**, *7*, 2413–2421.

(9) Liu, Y.; Tolentino, J.; Gibbs, M.; Ihly, R.; Perkins, C. L.; Liu, Y.; Crawford, N.; Hemminger, J. C.; Law, M. *Nano Lett.* **2013**, *13*, 1578–1587.

(10) Ocier, C. R.; Whitham, K.; Hanrath, T.; Robinson, R. D. *J. Phys. Chem. C* **2014**, *118*, 3377–3385.

(11) Otto, T.; Miller, C.; Tolentino, J.; Liu, Y.; Law, M.; Yu, D. *Nano Lett.* **2013**, *13*, 3463–3469.

(12) Oh, S. J.; Berry, N. E.; Choi, J.-H.; Gaulding, E. A.; Lin, H.; Paik, T.; Diroll, B. T.; Muramoto, S.; Murray, C. B.; Kagan, C. R. *Nano Lett.* **2014**, *14*, 1559–1566.

(13) Luther, J. M.; Law, M.; Beard, M. C.; Song, Q.; Reese, M. O.; Ellingson, R. J.; Nozik, A. J. *Nano Lett.* **2008**, *8*, 3488–3492.

(14) Oh, S. J.; Kim, D. K.; Kagan, C. R. *ACS Nano* **2012**, *6*, 4328–4334.

(15) Ning, Z.; Ren, Y.; Hoogland, S.; Voznyy, O.; Levina, L.; Stadler, P.; Lan, X.; Zhitomirsky, D.; Sargent, E. H. *Adv. Mater.* **2012** 24, 6295.

(16) Zhitomirsky, D.; Furukawa, M.; Tang, J.; Stadler, P.; Hoogland, S.; Voznyy, O.; Liu, H.; Sargent, E. H. *Adv. Mater.* **2012**, 24, 6181.

(17) Sze, S. M.; Ng, K. K. *Physics of Semiconductor Devices*; 3rd ed.; John Wiley & Sons: 2007.

(18) Rhoderick, E. H. *Metal-Semiconductor Contacts*; 2nd ed.; Claredon Press: Oxford, 1988.

(19) Jiang, X.; Schaller, R. *J. Mater. Res.* **2007**, *22*, 2204.

(20) Kim, D. K.; Vemulkar, T. R.; Oh, S. J.; Koh, W.-K.; Murray, C. B.; Kagan, C. R. *ACS Nano* **2011**, *5*, 3230–3236.

(21) Leschkies, K. S.; Kang, M. S.; Aydil, E. S.; Norris, D. J. *J. Phys. Chem. C* **2010**, *525*, 9988–9996.

(22) Kovalenko, M. V; Scheele, M.; Talapin, D. V. *Science* **2009**, *324*, 1417–1420.

(23) Law, M.; Luther, J. M.; Song, Q.; Hughes, B. K.; Perkins, C. L.; Nozik, A. J. *J. Am. Chem. Soc.* **2008**, *130*, 5974–5985.

(24) Luther, J. M.; Law, M.; Song, Q.; Perkins, C. L.; Beard, M. C.; Nozik, A. J. *ACS Nano* **2008**, *2*, 271–280.

(25) Liu, Y.; Gibbs, M.; Perkins, C. L.; Tolentino, J.; Zarghami, M. H.; Bustamante, J.; Law, M. *Nano Lett.* **2011**, *11*, 5349–5355.

(26) Ma, W.; Swisher, S.; Ewers, T.; Engel, J. *ACS Nano* **2011**, *5*, 8140–8147.

(27) Tang, J.; Brzozowski, L.; Barkhouse, D. A. R.; Wang, X.; Debnath, R.; Wolowiec, R.; Palmiano, E.; Levina, L.; Pattantyus-Abraham, A. G.; Jamakosmanovic, D.; Sargent, E. H. *ACS Nano* **2010**, *4*, 869–878.

(28) Maraghechi, P.; Labelle, A. J.; Kirmani, A. R.; Lan, X.; Adachi, M. M.; Thon, S. M.; Hoogland, S.; Lee, A.; Ning, Z.; Fischer, A.; Amassian, A.; Sargent, E. H. *ACS Nano* **2013**, *7*, 6111–6116.

(29) Tang, J.; Liu, H.; Zhitomirsky, D.; Hoogland, S.; Wang, X.; Furukawa, M.; Levina, L.; Sargent, E. H. *Nano Lett.* **2012**, *12*, 4889–4894.

(30) Talapin, D. V; Lee, J.-S.; Kovalenko, M. V; Shevchenko, E. V. *Chem. Rev.* **2010**, *110*, 389–458.

(31) Allgaier, R. S.; Scanlon, W. W. *Phys. Rev.* **1958**, *111*, 1029.

(32) Baumgardner, W. J.; Whitham, K.; Hanrath, T. *Nano Lett.* **2013**, *13,* 3225–3231

CHAPTER 5 Remote Doping and Schottky Barrier Formation in Strongly Quantum Confined Single PbSe Nanowire Field-Effect Transistors

This work was published in ACS Nano, entitled "Remote Doping and Schottky Barrier Formation in Strongly Quantum Confined Single PbSe Nanowire Field-Effect Transistors" S. J. Oh, D. K Kim, C. R. Kagan, ACS Nano, 2012, 6 (5) 4328.

We report studies of charge injection and transport in ambipolar, predominantly n-type, and unipolar p-type single, strongly quantum confined PbSe nanowire (NW) field effect transistors (FETs). The PbSe NW FETs operate as Schottky barrier FETs in which the Fermi level is pinned near midgap, consistent with the low ionicity of PbSe, and is nearly invariant with semiconductor doping. Electron and hole mobilities increase monotonically with decreasing temperature, dominated at high temperature by electron-phonon scattering with no evidence of scattering at low temperatures. Transport in NWs is consistent with their single crystalline nature. Surface oxygen used to dope the NWs acts remotely, providing a promising route to dope nanostructures.

5.1 Introduction

PbSe is a particularly interesting semiconductor to study in one-dimension. It has a large Bohr exciton radius (46nm) and large and equal electron and hole Bohr radii (23nm),[1] and therefore allows the regime of strong quantum confinement to be readily accessed in semiconducting nanowires (NWs). PbSe NWs are also technologically of great promise and have potential in field-effect transistors (FETs),[2] thermoelectrics,[3,4] and photodetectors[5] arising from large and similar carrier mobilities, reduced phonon scattering, and low thermal conductivity. In FETs, PbSe NWs have been shown to switch the polarity of charge transport between ambipolar, n-type and p-type characteristics depending on the chemistry of surface ligating compounds,[6] the presence of surface oxygen,[7] the surrounding gas[8] and stoichiometric imbalance,[9] but little is understood about the fundamental physics of charge injection and transport in these strongly quantum confined NWs and single PbSe NW FETs have been limitedly explored.

Here, we report temperature dependent electrical measurements used to uncover the physics of charge injection and charge transport in ambipolar, predominantly n-type ambipolar and unipolar p-type strongly quantum confined PbSe single nanowire (SNW) FETs. We demonstrate PbSe SNW FETs behave as Schottky Barrier (SB) FETs in which the *OFF* current is limited by the SB and decreases as temperature decreases, while the *ON* current is achieved by gate thinning of the SB and increases as temperature decreases. In the *OFF* state, the sum of the electron and hole SB heights is similar to the bandgap of PbSe NWs and the Fermi level is pinned consistent with the low ionicity of PbSe. In the *ON* states, we show that electron and hole mobilities increase monotonically as

temperature decreases consistent with the single crystalline nature of PbSe NWs and in contrast to most PbSe thin films[10,11] and PbSe nanocrystal (NC) arrays[12] which are dominated at low temperature by scattering at defects, dislocations, and grain boundaries, and by thermally activated hopping transport. Finally, we introduce surface oxygen and show that remote dopants form high mobility PbSe NWs. We suggest that remote dopants are a promising route to dope nanostructures without leading to Coulomb scattering.

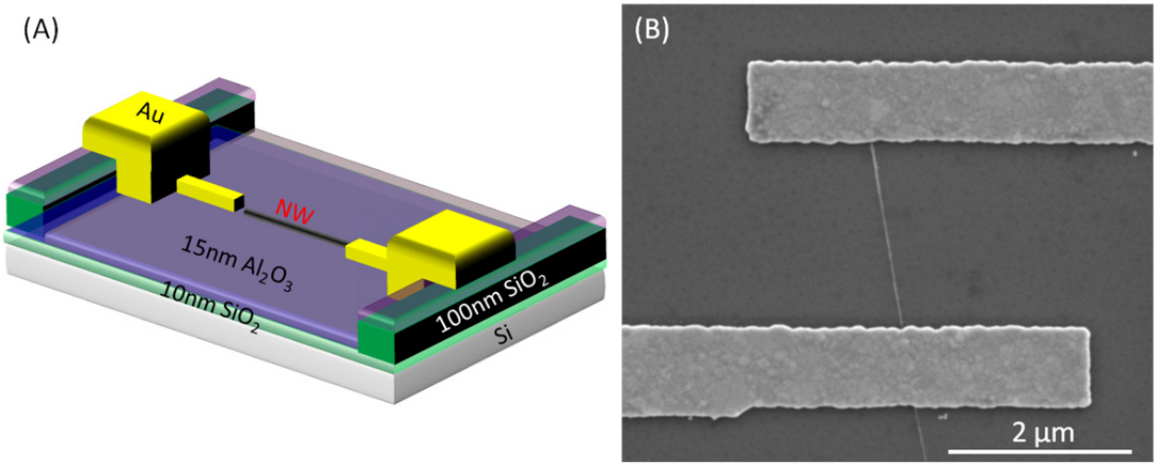

Figure 5.1 (A) Schematic of PbSe single nanowire (SNW) FET device and (B) SEM image of single NW device

5.2 Experimental Details

5.2.1 Fabrication and Measurement of Single PbSe NW FET

A single PbSe NW FET is depicted in Figure 5.1(A). FETs were fabricated on heavily n-doped silicon wafers with dielectric stacks of 10 nm thermally grown SiO_2 serving as the back gate and part of the gate dielectric stack, respectively. 100nm SiO_2 layer was patterned by photolithography to reduce gate leakage between subsequently deposited large area contact pads and the gate electrode and 15nm Al_2O_3 was deposited using atomic layer deposition to reduce further leakage and hysteresis. Photolithography and electron beam lithography were used to define metal pads. Single-crystalline, straight, 10nm diameter PbSe NWs were synthesized by wet-chemical methods, as reported previously.[7,13] A 5μL aliquot of the NW solution in octane/chloroform was dropcast between contacts and its location was recorded using optical microscopy. Top contact electrodes were defined by e-beam lithography and deposited by e-beam evaporation to contact the ends of the NWs with the bridging electrodes previously fabricated on the Si wafer. Rigorous air-free conditions were used from synthesis, device fabrication and characterization to prevent unintentional oxidation of the NWs.[7,15] These electrostatically well-scaled devices allow the study of SNW transport properties without short channel effects. An SEM image of the channel region of a representative PbSe SNW device is shown in Figure 5.1(B).

As-fabricated, PbSe SNW FETs are p-type with I_{ON}/I_{OFF} of 10^3 and hole saturation mobility of ~30 (±5) $cm^2/V\text{-}s$ [Figure S1]. The mobility was calculated in the saturation regime using the cylinder-on-plate model[14]

$$\mu = \left(\frac{d\left(I_D\right)^{0.5}}{dV_G} \right)^2 \frac{2L}{C_{OX}} \tag{1}$$

$$C_{ox} = \frac{2\pi\varepsilon\varepsilon_0 L}{\cosh\left(\frac{r + t_{ox}}{r} \right)} \tag{2}$$

where L is the length and r is the radius of the NW and ε is the dielectric constant and t_{ox} is the thickness of the oxide layer. Annealing the NW FETs at 180 ˚C for 5 min desorbs surface bound oxygen that acts to p-dope[15–18] the NWs and increases the electron current, forming FETs showing ambipolar behavior. Previously we have shown that annealing and evacuating PbSe NW FETs desorbs surface bound oxygen,[15] which creates acceptor states in PbSe,[7,15,19-21] resulting in polarity switching from p-type to ambipolar predominantly n-type behavior arising from a stoichiometric Pb excess introduced in synthesis.[15,22,23] It should be noted that devices annealed for longer times show predominant n-type conductivity, but if the device is not kept under vacuum the conductivity type again switched from predominantly n-type to ambipolar, and eventually to predominantly p-type again due to oxygen doping, even at the <1 ppm O_2 levels in the inert environment of a nitrogen glovebox. The SNW FET shows balanced electron and hole transport as seen in Figure 5.2 in the output characteristics in the (A) hole and B) electron accumulation regimes and in (C) the transfer characteristics. The device was

kept under vacuum after annealing. The threshold voltage shifted slightly further toward negative voltages, consistent with further oxygen desorption, and then the ambipolar behavior remained stable as studied for more than a few weeks under vacuum.

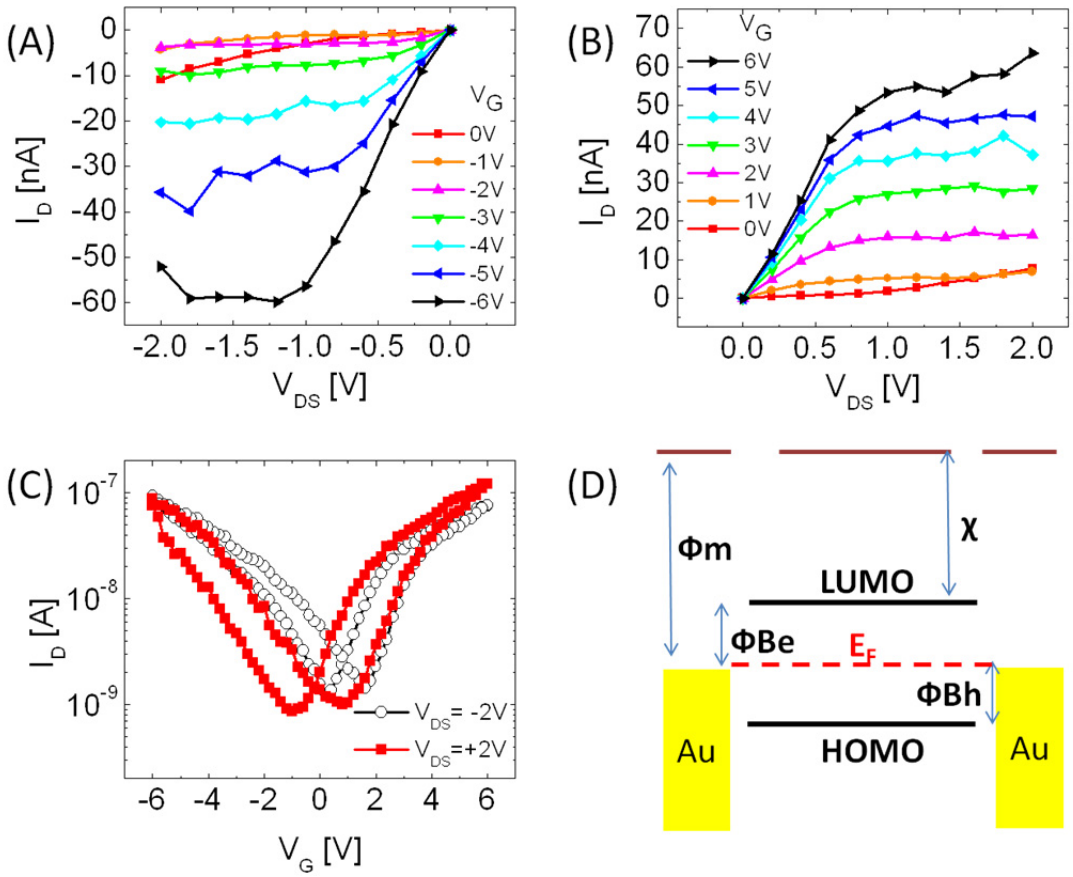

Figure 5.2 Output characteristics in the (A) hole and (B) electron accumulation regimes and (C) transfer characteristics at (black) V_{DS}=-2V and (red) V_{DS}=+2V of an ambipolar, PbSe SNW FET. (D) Schematic band diagram of an ambipolar SNW FET. LUMO is the lowest unoccupied molecular orbital, HOMO is the highest occupied molecular orbital, E_F is the Fermi energy, Φ_m is the work function of metal, Φ_{Be} is the electron barrier height, Φ_{Bh} is the hole barrier height, χ is the electron affinity of the PbSe NW.

There were noticeable changes observed before and after annealing. As the electron current increased with annealing, the hole current decreased, and the I_{ON}/I_{OFF} was limited to ~10^2. Statistics extracted from the I_D-V_G characteristics of tens of SNW FETs show electron and hole saturation mobilities of 6(±2) cm^2/V-s and 9(±2) cm^2/V-s, respectively. The change in electron and hole current levels are consistent with a shift in the Fermi energy towards mid-gap as oxygen acceptors are removed and the NW is de-doped.[15] Given the simplified electronic structure of PbSe and the similar bulk effective masses[24] and carrier mobilities, the ambipolar characteristics suggest the barriers to electron and hole injection are comparable [Figure 5.2(D)]. As the NW FETs are annealed to become ambipolar, the I_D-V_{DS} characteristics show greater non-linear behavior and are more closely spaced at low-voltages, consistent with current crowding and increased barriers to carrier injection.

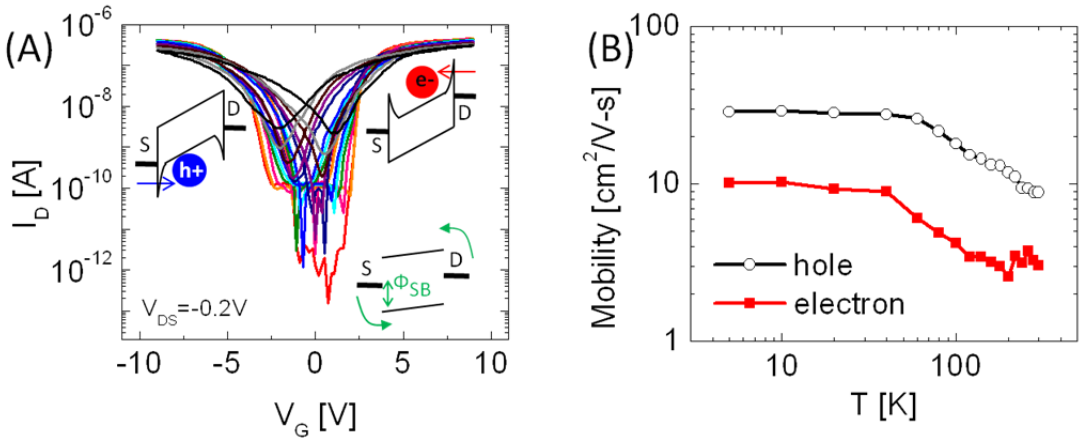

Figure 5.3 Ambipolar PbSe SNW FET (A) transfer characteristics at 4K (Red), 140K (Blue) and 298K (Black) and (inset) schematic band diagrams as a function of V_G and (B) electron mobility and hole mobility as a function of temperature.

5.3 Results and Discussions

5.3.1 Schottky Barrier FET Behavior revealed by Temperature Dependent Electrical Measurement

Representative temperature dependent transfer characteristics between 4K and 298K for ambipolar SNW FETs are shown for a subset of measured temperatures in Figure 5.3. At room temperature, the device I_{ON}/I_{OFF} is ~10^2-10^3 while at 4K I_{ON}/I_{OFF} is >10^6. A noticeable phenomenon is that the device shows a different dependence of current on temperature when the FET is in the "*ON* state" as opposed to in the "*OFF* state" [Figure 5.3(A)]. The current level increases as temperature decreases in the "*ON* state" (both at high positive V_G in electron accumulation and at high negative V_G in hole accumulation), while the current level decreases as temperature decreases in the "*OFF* state" at low $|V_G|$. We model the behavior by a SB FET[25] where the total current is controlled by charge injection, which is limited by the metal-semiconductor barrier, as well as charge transport through the NW. In the "*ON* state," particularly for FETs with thin gate dielectrics, high applied gate fields thin the SB at the metal-semiconductor interface, removing the barriers to charge injection. As seen in the inset of Figure 3(A), high negative (positive) gate voltage pulls the bands up (down), narrowing the barrier to allow tunneling of holes (electrons). In this "ON state", drain current is controlled by charge transport through the NW. The ON current increases as temperature decreases, which indicates band conduction transport where carrier scattering dominates, as commonly seen in inorganic semiconductors[26] and single crystalline PbSe.[10,27]

However, in the "*OFF* state" the current level at low temperature is lower than that at high temperature. The decrease in the current in the "*OFF* state" is attributed to limited charge injection from the SB.[28] In the absence of a high gate bias, the barrier is not thin enough for tunneling to occur and thus carrier injection is limited by the SB. For example, at low negative gate bias, the hole current is blocked by the SB at the source as shown in the inset of Figure 5.3(A). In this regime, thermionic emission over the barrier is the limiting step to reduce the drain current. The same behavior can be seen in earlier work by Liang *et al.*[4] although was not described in detail, and we propose that it is attributed to SB control. It should also be mentioned that the temperature dependent PbSe NW FET behavior is different from that of PbSe NC FETs.[12] In reported temperature dependent charge transport studies of ethanedithiol-treated PbSe NC thin films by Kang *et al.*, currents in both the "*ON* state" and "*OFF* state" decrease with decreasing temperature as conduction is controlled by thermally activated hopping between NCs. In the single crystalline PbSe NWs reported here, carriers are transported through the bands of the NWs and the role of SB can be easily separated. Since the SBs limit charge injection, linear electron and hole mobilities cannot be extracted. Therefore, electron and hole mobilities were calculated in the saturation regime ("ON state"). As temperature decreases from 298K to 4.5K, for ambipolar SNW PbSe FETs saturation mobilities of electrons and holes increase monotonically from 6(±2) cm^2/V-s to 15(±2) cm^2/V-s and from 9(±2) cm^2/V-s to 40(±4) cm^2/V-s, respectively [Figure 5.3(B)]. It should be noted that the carrier mobilities in PbSe NWs are lower than those found in Hall measurements of bulk PbSe. The measured and calculated PbSe NW carrier mobilities are effective mobilities rather than true mobilities since they may be limited by: (i) charge injection

due to the metal-semiconductor SB, and (ii) the cylinder-on plate model [Eq. (1)][29] which is reported to provide a lower bound in extracting carrier mobility. The mobilities may also be limited by (iii) surface scattering in these high surface-to-volume materials.

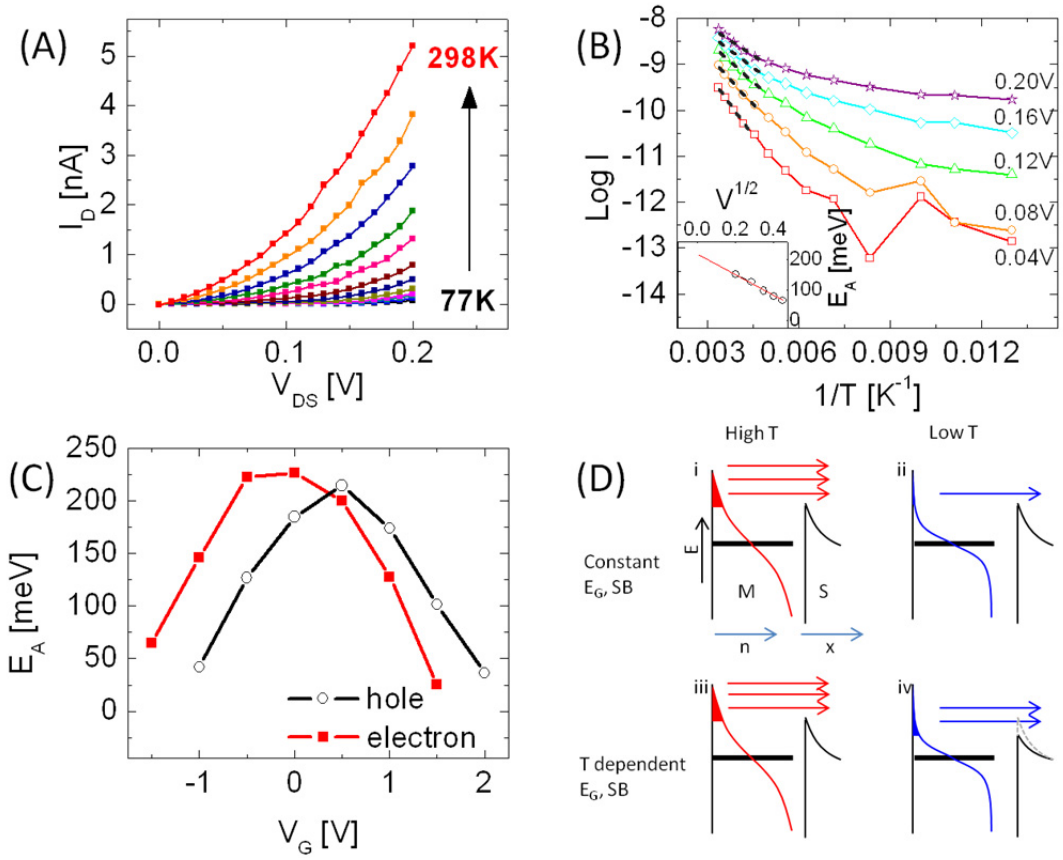

Figure 5.4 (A) I_D-V_{DS} curves at V_G=0.2V at temperatures between 77K and 298K (B) Arrhenius plot of I_D at different V_{DS} and (inset) the activation energy as a function of $V_{DS}^{1/2}$ (C) Calculated barrier heights as a function of V_G. (D) Schematic band diagrams of the metal-semiconductor interface representing charge injection for constant energy gap materials at (i) high and (ii) low temperature and for materials with a positive dE_G/dT at (iii) high and (iv) low temperature. M is metal, S is semiconductor, E is energy, n is number of electrons, and x is distance. Red and blue lines indicate the electron distribution[35)] *versus* energy at high temperature and low temperature, respectively, and the arrows indicate the amplitude of electron injection from metal to semiconductor.

The I_D-V_{DS} curves at different temperatures in the electron and hole accumulation regimes show the non-linear, Schottky behavior [Figure 5.4(A)]. The SB height can be extracted from the equation for thermionic emission[30]

$$I = A^{**}T^2 \exp\left[-q\left(\phi_B - \left(qE/4\pi\varepsilon_s\right)^{0.5}/k_B T\right)\right] \quad (3)$$

where A** is the effective Richardson's constant, k_B is Boltzmann's constant, q is electric charge, Φ_B is the Schottky barrier height, and E is the electric field. Figure 5.4(B) is the Arrhenius plot of the data obtained from Figure 5.4(A). The actual barrier height was calculated from the extrapolation of the plot inset in Figure 5.4(B) since activation energy, $E_{A,}$ is proportional to $V_{DS}^{1/2}$ due to image force lowering.[26,30] The electron and hole barrier heights depend on the gate bias, as the gate bias acts to pull down the barrier at the metal-semiconductor interface [Figure 5.4(C)]. The barrier height attains its maximum value around V_G=0. As the gate bias deviates from V_G=0, the effective barrier height decreases to zero and goes to negative values as it thins to where carrier tunneling through the barrier starts to dominate.[31] The electron and hole barrier heights, independently calculated from the data in the Arrhenius plots, were found to be 225meV and 215meV, respectively. The sum of the barrier heights is similar to the 0.44 eV bandgap of these 10 nm diameter PbSe NWs measured from their optical absorption spectrum[7], as we expect (E_g=Φ_{Be}+ Φ_{Bh})[26] and is illustrated in the schematic band diagram [Figure 5.2(D)]. The band alignment and SB formation is consistent with the balanced electron and hole current levels and similar carrier mobilities. We previously reported

cyclic voltammetry measurements to characterize the energies of the HOMO and LUMO levels of PbSe NWs. The HOMO and LUMO levels of predominantly p-type NWs, as-synthesized and washed with ethanol to remove surface bound ligands, are 4.62 eV and 4.17 eV, respectively; whereas surface treatment with hydrazine converts NW devices to predominantly n-type and shifts the energy levels to 5.01 eV and 4.56 eV, respectively.[7] The estimated 5.1 eV work function of Au for these top-contact single PbSe NW FETs is well below that of the energy levels of the NWs and suggests the origin of SB is Fermi level pinning. The Schottky barrier may arise from defects introduced by metal deposition in top contact devices.[26,32] In addition, for compound semiconductors with small electronegativity differences (where ΔX is the difference in electronegativities of the elements), as is the case for PbSe with ionicity $\Delta X = 0.22$ well lower than the characteristic $\Delta X < 1$,[26] barrier height is known to be weakly dependent on metal work function due to surface effects or pinning of the surface Fermi level. The observed SB is also consistent with the study of Luther *et al.*[33] on PbSe NCs which show weak dependence on metal work function and surface Fermi Level pinning that follows the Schottky model. In Figure 5.4(B), the slope of the Arrhenius plot decreases as temperature decreases, suggesting the SB height also decreases. It is accordant with the work of Boercker *et al.*[34] that the band gap of PbSe NWs decreases as temperature decreases. The temperature dependent slope can be understood by a thermionic emission model with a temperature dependent SB height. In materials with a temperature independent bandgap and SB height, as the temperature decreases from (i) high to (ii) low temperature [Fig. 5.4(D)], the amount of injected electrons only depends on the electron distribution according to the Fermi Dirac distribution,[35] resulting in a linear

slope in the Arrhenius plot. In contrast, PbSe NWs with a large positive dE_G/dT,[34] are expected to show a different behavior. As the temperature decreases from (iii) high to (iv) low temperature, [Fig. 5.4(D)] the SB height is reduced (iv) and therefore more carriers have sufficient energy to overcome the barrier, giving rise to the nonlinear slope in the Arrhenius plot. Despite the reduced SB height, however, current injection is limited at low temperature by the low carrier concentration.[35] While we report PbSe NWs shows SB behavior, it should be noted that SBs were not observed in bulk PbSe with Au contacts. We attribute this difference to the smaller bandgap and higher carrier concentration of bulk PbSe.[9,11]

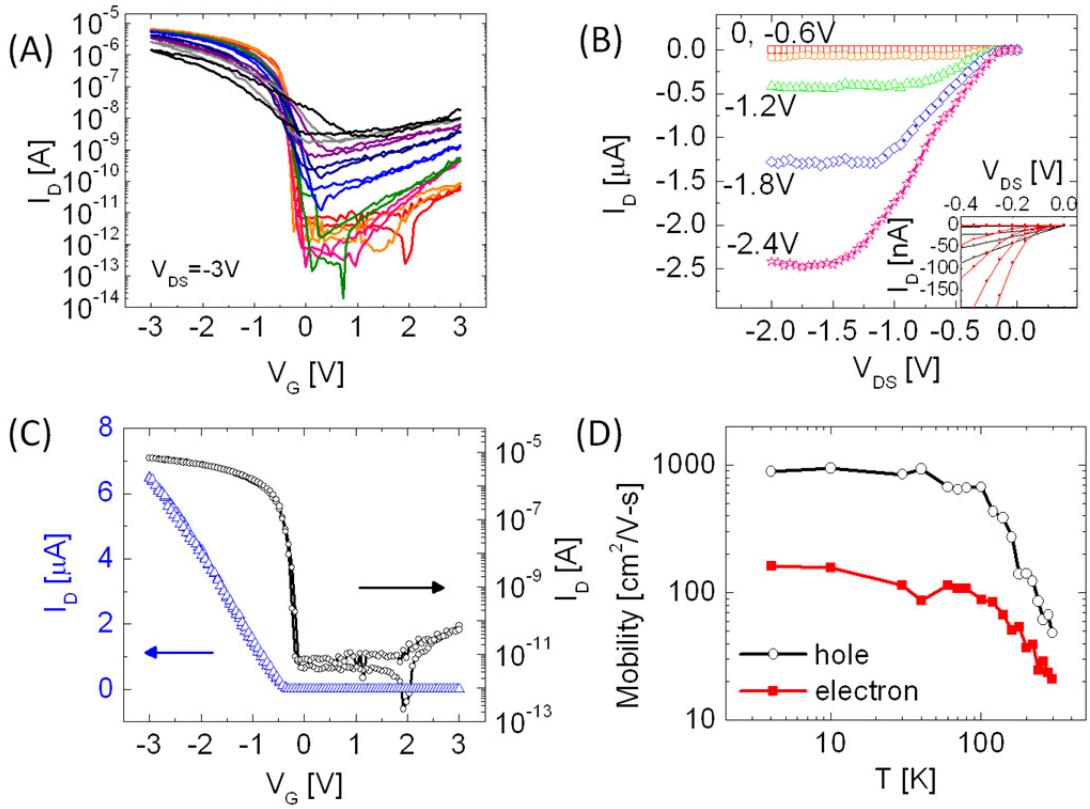

Figure 5.5 p-type PbSe SNW FET (A) Transfer characteristics at 4K (Red), 140K (Blue) and 298K (Black); (B) output characteristics at 4.5K. Inset magnifies the low voltage region of the I_D-V_{DS} characteristics at 4.5K (red) and 298K (black). (C) transfer characteristics at 4.5K (D) Saturation mobility as a function of temperature for holes in a unipolar p-type and electrons in a predominantly n-type PbSe SNW FET.

5.3.2 Charge Injection and Transport as a Function of Doping

Using this PbSe SNW FET platform, we explored charge injection and transport in the NWs as a function of doping. Figure 5.5(A) shows the temperature dependent transfer characteristics of a representative p-type PbSe SNW FET which was obtained by oxygen doping *via* 30s of UV-ozone exposure.[7,36] Similar to ambipolar NWs, p-type NWs also behave as SB FETs. The more severe "current crowding" behavior at low temperature [inset Figure 5.5(B)] reflects larger barriers to charge injection. Using temperature dependent I_D-V_{DS} characteristics, we extract the SB for holes as 185 meV, smaller than the SB for holes found for the ambipolar SNW FETs. At 4.5K a higher I_{ON}/I_{OFF} of ~10^7 and lower subthreshold swing of ~40 mV/dec than at room temperature [Figure 5.5(C)] are attributed to these SB FET characteristics and band conduction transport. At low temperature, the SB height limits the current at low V_G in the "OFF state" and as V_G increases the SB becomes thinned in the "ON state," allowing hole tunneling and giving rise to a dramatic increase in current. At low temperature (<100K), all hysteresis is eliminated, indicating trap sites[15] are frozen out. The maximum current for a single NW is ~10μA, corresponding to 1-2 orders higher current density of 10MA/cm^2 than previously reported for PbSe NWs.[3] The hole mobility of p-type PbSe NWs, calculated in the saturation regime, is plotted as a function of temperature in Figure 5.5(D). The hole mobility increased monotonically with decreasing temperature from 65(±10) cm^2/Vs at room temperature to 1000(±100) cm^2/Vs at 20K where it starts to saturate. The mobility increase between 200K and 300K shows a ~$T^{-2.2}$ power law dependence akin to the power law dependence of ~ $T^{-2.1\sim2.5}$ for bulk PbSe.[9,11] Similarly,

ambipolar predominantly n-type FETs are prepared by annealing the SNW PbSe FETs at 200 ˚C for 10 min and immediately transferring (see Method section) them to the vacuum chamber to avoid oxygen exposure. The electron mobility of predominantly n-type FETs as a function of temperature is shown in Figure 5.5 (D) and the SB height for the electrons and holes are extracted as 190meV and 230meV, respectively. The observed trend in SB height for p-type, ambipolar, and predominantly n-type PbSe NW FETs shows a weak decrease in barrier height for the majority carrier and corresponding increase in barrier height for the minority carrier height as the NW doping is tailored.

In ambipolar, predominantly n-type, and unipolar p-type PbSe SNW devices, electron and hole mobilities increased monotonically with decreasing temperature and saturated at temperatures less than ~20 K. There were no signatures of impurity scattering observed which commonly limits carrier mobilities at low temperatures in substitutionally doped NWs while other NWs[37,38] show higher impurity scattering at low temperature. While mobility decreases as temperature decreases in the case of most PbSe thin films and PbSe NCs mainly due to grain boundaries,[17,39] dislocations,[9] defects,[11,17] and thermally activated hopping mechanisms,[12] our data shows that the mobility of PbSe NWs increases monotonically as temperature decreases, which is limited at high temperatures by phonon scattering. To the best of our knowledge, this is the first report to show that nano-scale lead chalcogenides behave like single crystals without showing the effects of defects or grain boundaries. We also show that stoichiometric imbalance, which gives rise to the predominantly n-type characteristics, in which excess Pb acts as an ionized impurity,[15,27] does not contribute to scattering down to ~20K, in accordance

with bulk lead salts.[9] Moreover, we found that the introduction of surface oxygen which dopes PbSe NWs p-type[8,15] acts as a remote dopant, leaving the PbSe NW channel free of impurities with no evidence of scattering to limit carrier mobility. Remote doping by introducing surface species is akin to "modulation doping" in modulation doped FETs (MODFET)[26] where charge maybe transferred without introducing impurities.

5.4 Conclusions

In conclusion, we have studied the physics of charge injection and charge transport using p-type, predominantly n-type and ambipolar, 10nm diameter single PbSe NW FETs which is one of the most strongly confined systems that has been studied, particularly in 1D. Using temperature dependent electrical measurements of single NW FETs, we show for the first time that PbSe NW FETs operate as SB FETs. PbSe NWs behave as single crystals without defects which have not been reported previously in nanostructured lead chalcogenides. We show that remote doping in nanostructured lead chalcogenides promises an attractive route to apply more broadly in achieving high mobility n- and p-type materials without suffering from impurity scattering. Engineering the metal-semiconductor interface to lower the barriers to charge injection and reduced scattering through charge transport in remotely doped, single crystalline nanostructures are essential for the application of PbSe NWs in thermoelectrics and near-infrared photodetectors.

5.5 References

(1) Efros, A. L.; Efros, A. L. *Sov. Phys. Semicond.* **1982**, *16*, 772.

(2) Talapin, D. V.; Black, C. T.; Kagan, C. R.; Shevchenko, E. V.; Afzali, A.; Murray, C. B. *J. Phys. Chem. C* **2007**, *111*, 13244-13249.

(3) Liang, W.; Hochbaum, A. I.; Fardy, M.; Rabin, O.; Zhang, M.; Yang, P. *Nano Lett.* **2009**, *9*, 1689-93.

(4) Liang, W.; Rabin, O.; Hochbaum, A. I.; Fardy, M.; Zhang, M.; Yang, P. *Nano Research* **2009**, *2*, 394–399.

(5) Bierman, M. J.; Lau, Y. K. A.; Jin, S. *Nano Lett.* **2007**, *7*, 2907–2912.

(6) Talapin, D. V.; Murray, C. B. *Science* **2005**, *310*, 86-9.

(7) Kim, D. K.; Vemulkar, T. R.; Oh, S. J.; Koh, W.-K.; Murray, C. B.; Kagan, C. R. *ACS Nano* **2011**, *5*, 3230-6.

(8) Leschkies, K. S.; Kang, M. S.; Aydil, E. S.; Norris, D. J. *J. Phys. Chem. C* **2010**, *525*, 9988-9996.

(9) Allgaier, R. S.; Scanlon, W. W. *Phys. Rev.* **1958**, *111*, 1029.

(10) Silverman, S.; Levinstein, H. *Phys. Rev.* **1954**, *94*, 871.

(11) Ravich, U. I. *Semiconducting Lead Chalcogenides*; Plenum Press: New York, 1970.

(12) Kang, M. S.; Sahu, A.; Norris, D. J.; Frisbie, C. D. *Nano Lett.* **2011**, *11*, 3887-3892.

(13) Cho, K.-S.; Talapin, D. V.; Gaschler, W.; Murray, C. B. *J. Am. Chem. Soc.* **2005**, *127*, 7140-7.

(14) Cui, Y.; Duan, X.; Hu, J.; Lieber, C. M. *J. Phys. Chem. B* **2000**, *104*, 5213–5216.

(15) Kim, D. K.; Lai, Y. L.; Vemulkar, T. R.; Kagan, C. R. *ACS Nano* **2011**, *5*, 10074.

(16) Luther, J. M.; Law, M.; Song, Q.; Perkins, C. L.; Beard, M. C.; Nozik, A. J. *ACS Nano* **2008**, *2*, 271-80.

(17) Das, V. D.; Bhat, K. S. *Phys. Rev. B* **1989**, *40*, 7696.

(18) Bhat, K. S.; Das, V. D. *Phys. Rev. B* **1985**, *32*, 6713-6719.

(19) Harada, R.; Minden, H. *Phys. Rev.* **1956**, *102*, 1258.

(20) Jones, R. H. *Proc. Phys. Soc. London, Sect. B* **1957**, *70*, 1025-1032.

(21) Rogacheva, E. I. Tavrina, T. V. Grigorov, S. N. Nashchekina, O. N. Volobuev, V. V. Fedorov, A. G. Nasedkin, K. A.; Dresselhaus, M. S. *J. Electron. Mat.* **2002**, *31*, 298-303.

(22) Moreels, I.; Fritzinger, B.; Martins, J. C.; Hens, Z. *J. Am. Chem. Soc.* **2008**, *130*, 15081-6.

(23) Moreels, I.; Lambert, K.; Muynck, D. D. *Chem. Mater.* **2007**, *19*, 6101-6106.

(24) Kang, I.; Wise, F. W. *J. Opt. Soc. Am.* **1997**, *14*, 1632.

(25) Heinze, S.; Tersoff, J.; Martel, R.; Derycke, V.; Appenzeller, J.; Avouris, P. *Phys. Rev. Lett.* **2002**, *89*, 106801.

(26) Sze, S. M.; Ng, K. K. *Physics of Semiconductor Devices*; 3rd ed.; John Wiley & Sons: New Jersey, 2007.

(27) Schlichting, U.; Gobrecht, K. *J. Phys. Chem. Solids* **1973**, *34*, 753–758.

(28) Appenzeller, J.; Knoch, J.; Derycke, V.; Martel, R.; Wind, S.; Avouris, P. *Phys. Rev. Lett.* **2002**, *89*, 126801.

(29) Khanal, D.; Wu, J. *Nano Lett.* **2007**, *7*, 2778–2783.

(30) Rhoderick, E. H. *Metal-Semiconductor Contacts*; 2nd ed.; Claredon Press: Oxford, 1988.

(31) Appenzeller, J.; Radosavljević, M.; Knoch, J.; Avouris, P. *Phys. Rev. Lett.* **2004**, *92*, 048301.

(32) Dos Santos, O.; Mathet, V.; Fau, C.; Charar, S.; Averous, M. *Solid-State Electron.* **1996**, *39*, 813–819.

(33) Luther, J. M.; Law, M.; Beard, M. C.; Song, Q.; Reese, M. O.; Ellingson, R. J.; Nozik, A. J. *Nano Lett.* **2008**, *8*, 3488–3492.

(34) Boercker, J. E.; Clifton, E. M.; Tischler, J. G.; Foos, E. E.; Zega, T. J.; Twigg, M. E.; Stroud, R. M. *J. Phys. Chem. C* **2011**, *2*, 527-531.

(35) Density of electrons exponentially decreases above E_F and decreases as T decreases according to Fermi Dirac distribution.

$$f(E) = \frac{1}{1 + e^{\left(\frac{E - E_F}{k_B T}\right)}}$$

(36) Zhao, N.; Osedach, T. P.; Chang, L.-Y.; Geyer, S. M.; Wanger, D.; Binda, M. T.; Arango, A. C.; Bawendi, M. G.; Bulovic, V. *ACS Nano* **2010**, *4*, 3743-52.

(37) Park, T.-E.; Min, B.-C.; Kim, I.; Yang, J.-E.; Jo, M.-H.; Chang, J.; Choi, H.-J. *Nano Lett.* **2011**, *11*, 4730-5.

(38) Motayed, A.; Davydov, A. V.; Mohammad, S. N.; Melngailis, J. *J. Appl. Phys.* **2008**, *104*, 024302.

(39) Zemel, J.; Jensen, J. *Phys. Rev.* **1965**, *140*, A330.

Chapter 6 Strongly-coupled and In-doped CdSe NC thin film for air stable and high performance electronic and optoelectronic device

This work was published in part in "Thiocyanate Capped Nanocrystal Colloids: A Vibrational Reporter of Surface Chemistry and a Solution-based Route to Enhanced Coupling in Nanocrystal Solids"[1] A. T. Fafarman, W.-K. Koh, B. T. Diroll, D. K. Kim, D.-K. Ko, S. J. Oh, X. Ye, V. Doan-Nguyen, M. R. Crump, D. C. Reifsnyder, C. B. Murray, and C. R. Kagan JACS, 133 (39), 15753–15761, (2011); in "Bandlike Transport in Strongly Coupled and Doped Quantum Dot Solids: A Route to High-Performance Thin-Film Electronics,"[2] J.-H. Choi, A. T. Fafarman, S. J. Oh, D.-K. Ko, D. K. Kim, B. T. Diroll, S. Muramoto, J. G. Gillen, C. B. Murray, and C. R. Kagan, Nano Letters, 12 (5) 2631-2638 (2012); and in "In-situ Repair of High-Performance, Flexible Nanocrystal Electronics for Large-Area Fabrication and Operation in Air"[3] J.-H. Choi, S. J. Oh, Y. Lai, D. K. Kim, T. Zhao, A. T. Fafarman, B. T. Diroll, C. B. Murray, and C. R. Kagan, ACS Nano, 7(9) 8275–8283 (2013).

In Chapter 6, high performance electronic and optoelectronic CdSe NC thin films devices are fabricated through strong electronic coupling introduced by a combination of exchange of the NC surface ligands with the compact thiocyanate ligand and through surface passivation and doping introduced by thermal evaporation of indium. We show that indium diffusion allows the behavior of CdSe NC thin films to be recovered after air and solvent exposure, enabling the use of fabrication techniques such as photolithography and atomic layer deposition, for the preparation of large-area, flexible and air-stable NC devices.

6.1. CdSe NC thin film photodetector through strong electronic coupling with thiocyanate ligands

Similar to lead chalcogenide NCs, cadmium chalcogenide NCs are one of the most extensively studied NCs due to their unique properties and potential for visible-range optical and optoelectronic applications. While they show great potential for light emission[4–7] and biological applications,[8,9] there have been few studies for electronic applications. The lack of ligand exchange chemistries and processes that can enhance electronic coupling was the main hurdle. As similarly shown in Chapter 1, the long ligands used in NC synthesis are essential to assure high NC crystallinity and prevent the aggregation of their dispersions. However, they do not allow NCs to electronically communicate with each other, making NC thin films insulating.

In collaboration with Kagan and Murray group members and led by Prof. Aaron Fafarman, we introduce a short and inorganic ligand, ammonium thiocyanate (NH_4SCN) to exchange the long original NC ligands and still allow NC dispersion in solution.[1] The short ligands greatly reduce the interparticle distance between NCs and increase the conductivity of NC thin films. We apply this novel ligand exchange chemistry to CdSe NC thin films to enhance the electronic coupling between NCs and fabricate high performance optoelectronic and electronic devices.

CdSe NCs are synthesized by Ben Diroll using a modification of a literature synthesis.[10] Then, SCN ligand exchange is performed by Prof. Aaron Fafarman [Figure 6.1 (A)]. In detail, 0.5 mL of 130 mM NH_4SCN in acetone was added to 1 mL of a

dispersion of CdSe NCs in hexanes (the concentration was controlled by adjusting the optical density of the dispersion at the peak of the lowest energy excitonic absorption feature, e.g. 583 nm for 3.9 nm diameter NCs,[10] to a value of 10 to 20 per cm) and stirred with a vortex mixer at 3000 rpm for 2 min. Flocculation is clearly observed within a few seconds. The slurry was centrifuged at 2000 x *g* for 1 min and the supernatant discarded. 1 mL of tetrahydrofuran was added and the slurry stirred at 3000 rpm for 2 min, centrifuged at 2000 x *g* for 1 min and the supernatant discarded. 1 mL of toluene was added and the slurry stirred at 3000 rpm for 1 min, centrifuged at 2000 x *g* for 1 min and the supernatant discarded. 0.2 mL of dimethylformamide is added and the mixture is agitated gently, until the NCs were dispersed.

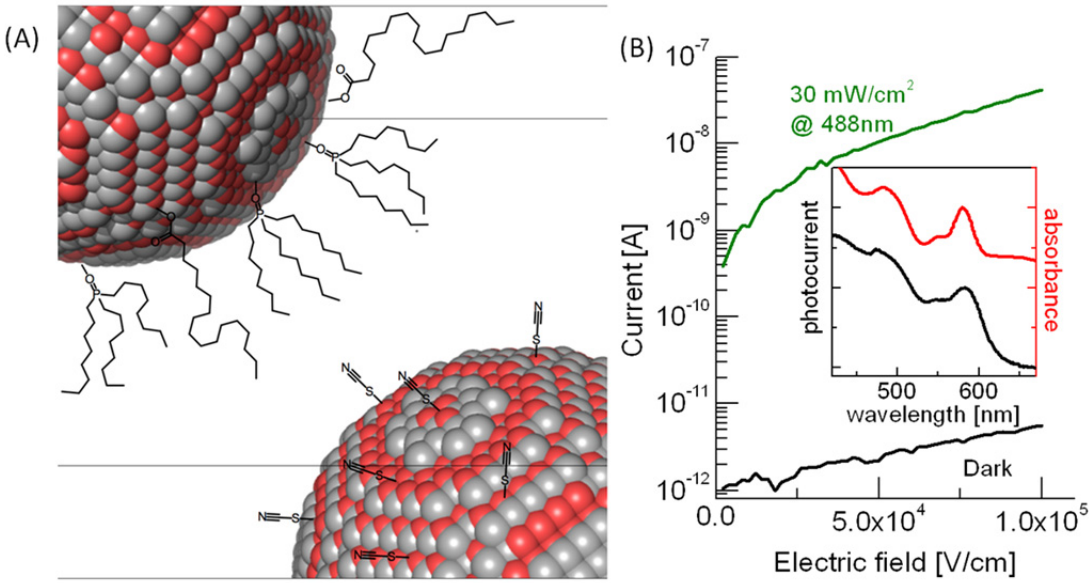

Figure 6.1 (A) Schematic of the ligand exchange process and (B) photoconductivity of a SCN-treated CdSe NC thin film on quartz. Dark current (black) and photo current for 488 nm illumination at 30 mW/cm^2 (green). (Inset : Spectral response and absorption spectra for the CdSe NC thin film) [Adapted from reference 1].

For the CdSe NC thin film photodetector fabrication, polished quartz windows are used as substrates. Gold electrodes (10 μm channel length, 150 μm channel width) are fabricated using standard photolithography processes. UV-ozone treatment is conducted to clean the substrate before deposition. CdSe NCs are then deposited after the solution exchange onto the substrate, and the device is shortly annealed at 50 °C. The active area is carefully sealed with epoxy (5 Minute™, ITW Devcon) under a glass coverslip in a nitrogen filled glove box. Samples are removed from the glovebox for measurement. The samples are illuminated with the 488nm line of an Innova 70C spectrum Ar:Kr laser (Coherent). Optical density filters are used to control the illumination power density. Photo- and dark conductivity are measured by an electrometer (Keithley, 6517B).

Figure 6.1 (B) shows the photoconductivity of SCN-treated CdSe NC thin films under 30 mW/cm^2 illumination. A photoconductivity of 10^{-5} Ω^{-1}cm^{-1} is extracted at an electric field of 100 kV/cm, which is 3 order higher than previously reported photoconductivity in butylamine-treated CdSe NC thin films under similar experimental conditions.[11] SCN-treated NC thin films show higher dark currents than other small ligand treated CdSe NCs. More importantly, the ratio of photo- to dark current was 10^3 - 10^4 at 100 V, as seen by comparing the black and green curves. This high photoconductive gain is also much higher than the previously reported butylamine-treated CdSe NC thin films.[12] The enhanced charge transport and favorable sensitivity are achieved without a loss of the spectral tunability. The inset of Figure 6.1 (B) shows that the spectral response for CdSe-SCN films resembles the optical absorption spectrum,

reflecting quantum confinement effects in NCs. It should be noted that the resolution of the spectral response data is limited by the instrument bandpass.

6.2. High performance CdSe NC FETs through the combination of strong electronic coupling and indium doping.

While we enhance the electronic coupling between NCs through thiocyanate ligand exchange, it does not guarantee the fabrication of high performance electronic devices. NC surface states and semiconductor-dielectric interface states in the geometry of the transistors introduce trap states lying within the NC thin film band gap. The trap states prevent the efficient transport. We show that by doping the NC thin films, we passivate midgap trap states and control the carrier concentration, raising the Fermi level close to conduction band. We achieve NC passivation and doping through thermal diffusion of indium, developed by Dr. Ji-Hyuk Choi. This work was led by Ji-Hyuk Choi and carried out in collaboration with Kagan and Murray group members and Dr. Shin Muramoto and Dr. J. Greg Gillen at NIST.[2]

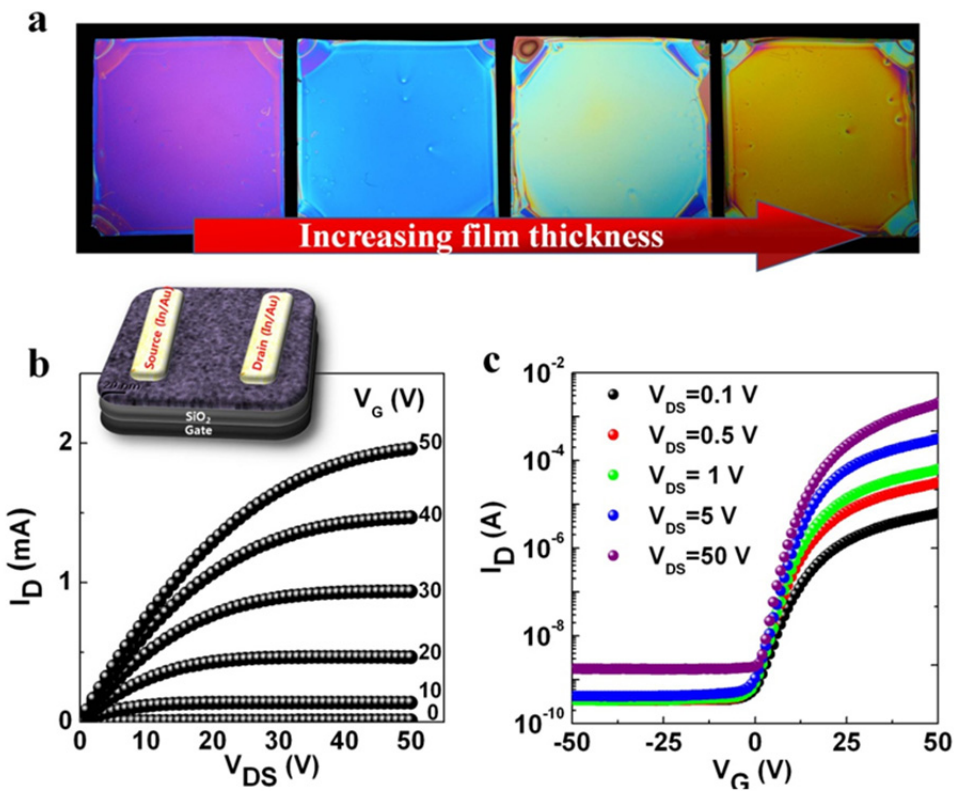

Figure 6.2 (A) Photograph of SCN-treated CdSe NC films on Si wafers with varying film thickness from 25 nm (left) to 130 nm (right). (B) Output and (C) transfer characteristics with various V_{DS} (0.1 V to 50 V) for a CdSe NC thin film FET annealed at 250 ˚C for 10 min. Inset in (B) is a schematic of the device structure. [Adapted from reference 2]

SCN-treated CdSe NC thin films are prepared using a similar method described in Chapter 6.1. NCs are deposited on heavily-doped silicon wafers with 250 nm of SiO_2, serving as the back gate and part of the gate dielectric stack, respectively. To examine the effect of the interface between NCs and dielectric stack, two different gate dielectric stacks are prepared - - with and without Al_2O_3. To prepare an Al_2O_3 interface, an additional 20 nm of Al_2O_3 was deposited by atomic layer deposition. Different CdSe NC film thickness can be deposited by controlling the NC concentration in solution, as seen in Figure 6.2 (A). The optimal thickness for the FET is found to be 2-30 nm. After NC thin film formation, top contact source and drain electrodes are deposited by thermal evaporation of In/Au through a shadow mask. The representative [Figure 6.2 (B)] output and [Figure 6.2 (C)] transfer curves of devices annealed at 250 ^{o}C for 10 min are shown. The current is very low in the *off*-state (V_G=-50-0V), but starts to increase dramatically as the gate bias is increased toward +50V. The device behavior is characteristic of electron accumulation, a signature of an n-type semiconductor. I_{on}/I_{off} ratio is found to be higher than 10^6 and the subthreshold swing is extracted as ~3 V/dec at V_{DS} = 5 V. It also shows a very low hysteresis and low contact resistance, indicating Ohmic contacts.

The saturation and linear mobility are extracted as 19 cm^2/Vs (at V_{DS}=50V) and 20 cm^2/Vs (at V_{DS}=0.1V), respectively. This field-independent and high mobility, larger than the Mott-Ioffe-Regal limit,[13] strongly suggest that electron transport in NC thin films occurs through extended states, rather than by hopping between localized states.[14-16]

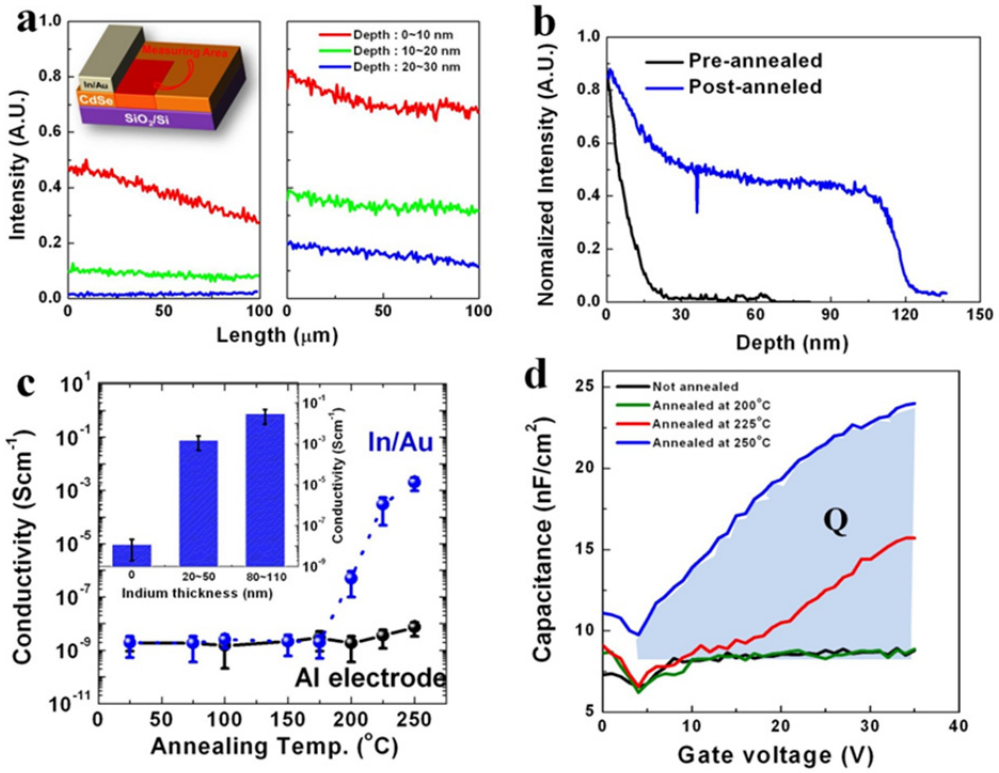

Figure 6.3 (A) Lateral distribution of $113In^+$ as a function of depth (left) pre-annealed and (right) post-annealed sample. (inset : a schematic of the measured 100 × 100 μm^2 sample area.) (B) Depth profile of the $113In^+$ distribution for pre-annealed and post-annealed samples. (C) Conductivity of CdSe NC thin films on quartz with In/Au and Al electrodes as a function of annealing temperature. (Inset : the conductivity of CdSe NC thin films annealed with different indium thickness) (D) Capacitance-Voltage characteristics of CdSe NC thin films as function of gate-voltage annealed at a temperature from 200 ^oC to 250 ^oC. [Adapted from Reference 2]

Using time-of-flight secondary ion mass spectrometry (ToF-SIMS) in collaboration with Dr. J. Greg Gillen and Dr. Shin Muramoto, we showed that indium readily diffuses through the CdSe NC thin film.[Figure 6.3 (A, B)]. Next, to confirm the effect of In doping, we compare a device with In/Au electrodes to a device with Al electrodes, noting that In and Al have almost the same work function. The electrical conductivity of CdSe NC films with In/Au and Al electrodes are shown in Figure 6.3 (C) as a function of annealing temperature. Both devices with Al and In/Au contacts shows the conductivity of 10^9 S/cm at low temperature, limited by the noise level in our measurement system. While devices with In/Au contacts show a significant increase in conductivity upon annealing at 200-250 ^{o}C, devices with Al contacts shows little change in conductivity using the same annealing conditions. By changing the In thickness, we can control the electrical properties of NC thin films from that characteristic of an insulator, to a semiconductor and to a degenerately doped semi-metallic behavior [inset of Figure 6.3 (C)].

To quantitatively analyze the carrier statistics, we conduct capacitance-voltage measurements [Figure 6.3 (D)]. Accumulated free carriers are calculated by $\mathrm{Q} = \int_{\mathrm{O}}^{\mathrm{V_G}} \mathrm{C}(V)\mathrm{d}V$, and extracted as 0.1 electrons per NC, assuming NCs are random close-packed with a density of 0.5.

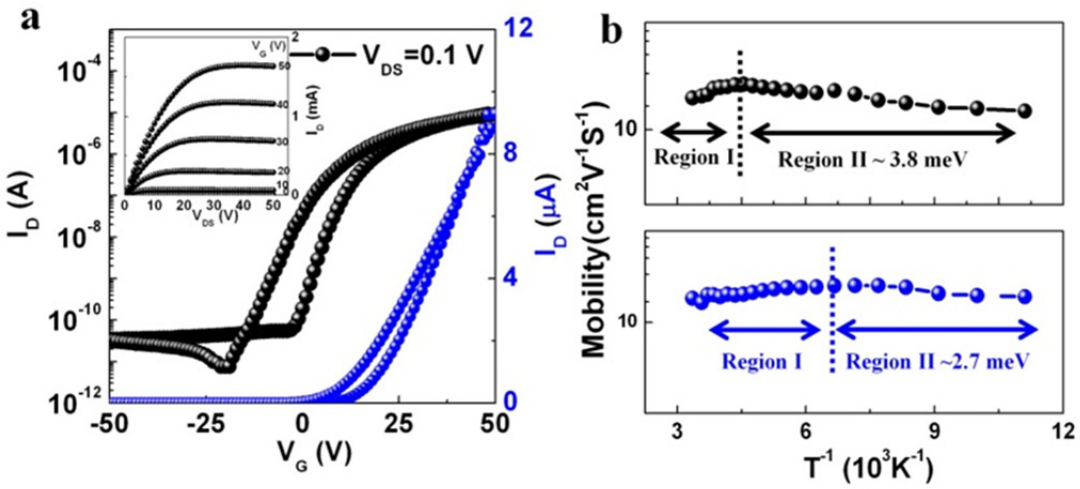

Figure 6.4 (A) Transfer characteristics of CdSe NC thin film FETs with an Al_2O_3/SiO_2 gate dielectric stack at V_{DS}=0.1 V (inset : device output characteristics) (B) Temperature dependent mobilities of CdSe NC FETs with SiO_2 and Al_2O_3/SiO_2 gate dielectric stacks. [Adapted from the Reference 2]

To investigate the effect of the NC-dielectric interface, we fabricate CdSe NC FETs on an Al_2O_3/SiO_2 gate dielectric stack. The transfer and output characteristics of CdSe NC FET with an Al_2O_3/SiO_2 gate layer are shown in Figure 6.4 (A). The device shows even higher mobility of ~27 cm^2/Vs and lower hysteresis, comparing to that for FETs fabricated using a SiO_2 dielectric layer. This is attributed to the reduction in trap density at the semiconductor-dielectric interface. We quantitatively calculate the density of trap states. The trap concentration is extracted as 8.97×10^{12} cm^{-2} for Al_2O_3 interface, and 1.36×10^{13} cm^{-2} with SiO_2 interface.

We carry out temperature dependent FET measurements to characterize the charge carrier transport behavior. Devices are loaded in a low-temperature probe station chamber and measured under high vacuum (10^{-6} Torr) as a function of temperature between 77 K and room temperature. We observe an increase in mobility with decreasing temperature for both Al_2O3/SiO_2 and SiO_2 gate dielectric stacks. This is direct evidence in support of band-like transport[17] through the extended states, in contrast to thermally activated hopping transport where the mobility decreases as temperature decreases. Band-like transport is achieved through the combination of 1) the strong electronic coupling through the use of compact thiocyanate ligands and of 2) doping by indium to passivate traps and increase the Fermi level to promote electrons in extended states.

At lower temperatures, the carrier transport is dominated by shallow trap states. We found an activation energy of 7.5 meV for the SiO_2 gate dielectric layer and 6.2 meV for the Al_2O_3/SiO_2 dielectric stack. It should be also noted that the transition temperature is 220 K for the SiO_2 and 140 K for the Al_2O_3/SiO_2 dielectric stack. This supports the larger trap density of SiO_2 layer and emphasizes the importance of the role of interface.

6.3. Air stable NC FETs though recovery by In diffusion and ALD passivation

While excellent electronic and optoelectronic NC devices are being demonstrated, there is another big challenge for the practical use of NC devices, that is, the air-sensitivity. Due to high surface-volume ratio, NCs are very sensitive to surroundings, such as air and solvents.[18-22] This limits the utilization of NCs in applications and has commonly restricted most device fabrication and measurement to be carried out in nitrogen filled gloveboxes. In collaboration with Kagan and Murray group members and led by Dr. Ji-Hyuk Choi, we demonstrated a novel, low-temperature process to recover device behavior after fabrication in air and with the use of solvents using common cleanroom tools and to encapsulate NC devices allowing their operation in ambient-air. Utilizing this recovering process and encapsulation method, we fabricate large-area, flexible, and air-stable NC devices.

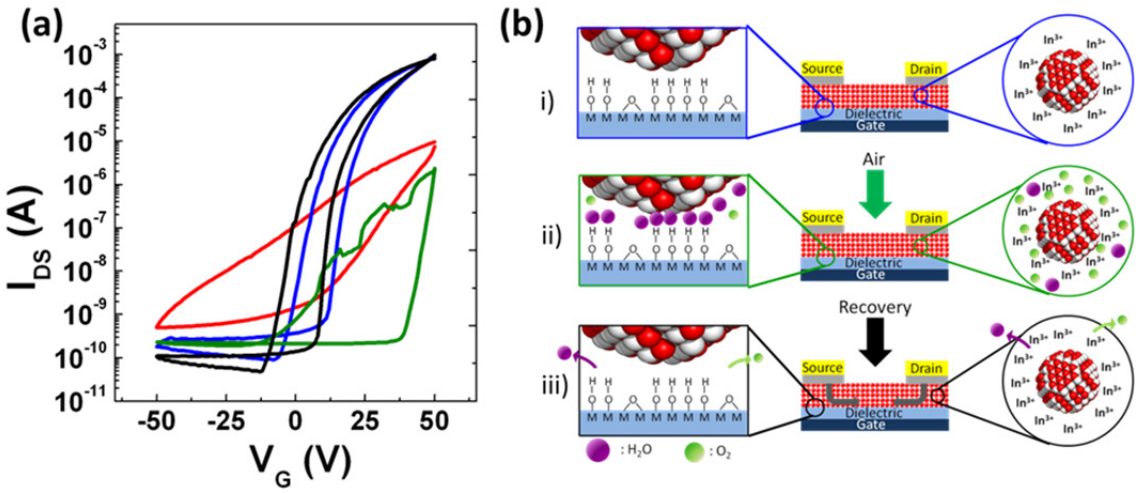

Figure 6.5 (A) I_D-V_G characteristics of CdSe NC thin films annealed at 250 ^oC for 10 min prior to In/Au electrode deposition (red) and then annealed at 250 ^oC for 10 min to allow indium diffusion and device doping (blue), exposed to air for 30 min (green), and re-annealed at 200 ^oC for 5 min (black). (B) Schematic of NC FET recovery after air exposure: (i) indium-doped CdSe NC devices, (ii) once exposed to air adsorb oxygen and water at the NC and gate oxide surfaces and (iii) are recovered upon annealing under nitrogen as oxygen and water desorbs and additional indium diffuses from the electrode reservoirs. [Adapted from reference 3]

Previously we found that the SCN-treated CdSe NC FETs are not stable under air and are readily attacked by O_2, H_2O and other chemicals. This sensitivity inhibits the use of conventional fabrication techniques such as photolithography that requires the use of deionized water and other solvents. What is worse is that the device performance is found to deteriorate in 24 hours even in the glove box with a small oxygen level of <10ppm. However, we find that the device recovers upon low temperature re-annealing. This motivated us to test the air-exposed devices after re-annealing. Pre-annealed CdSe NC FETs [Figure 6.5(A), red] are post-annealed at 250 ºC for 10 min to activate the In diffusion and achieve high performance device [Figure 6.5(A), blue]. Then samples are exposed to air degrading their performance [Figure 6.5 (A), green]. But the performance is recovered upon re-annealing at 200ºC for 5 min in the glovebox [Figure 6.5 (A) black]. We found that this recovery effect is attributed to the desorption of surface oxygen and water[41] and indium re-diffusion [Figure 6.5 (B)].

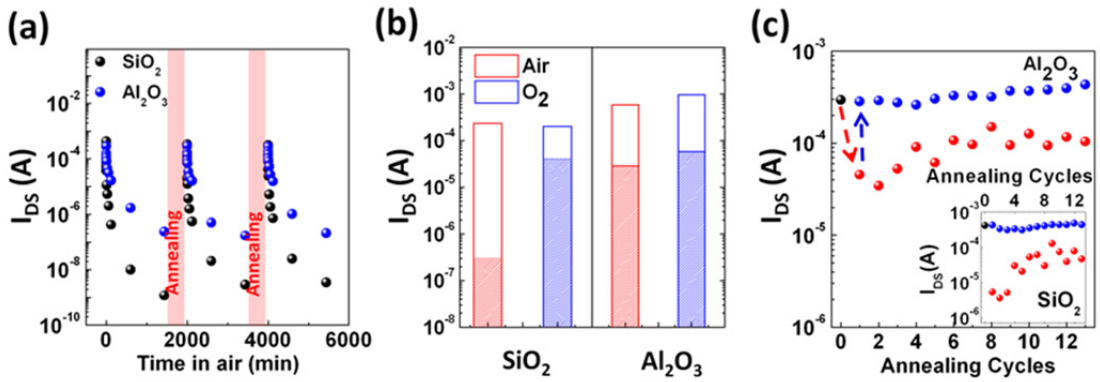

Figure 6.6 (A) Cyclic degradation as a function of air exposure time and recovery upon re-annealing at 200 ^{o}C for 5 min for FETs fabricated on Al_2O_3 and SiO_2 gate dielectric stacks. (B) Degradation in air versus in pure oxygen environment (open bar : initial, filled bar : exposure) for Al_2O_3 and SiO_2 gate dielectric stacks. (C) As-prepared (black) and upon successive cycles of air exposure for 30 min (red) and recovery by annealing at 200 ^{o}C for 5 min (blue) on Al_2O_3 and (inset) SiO_2 gate dielectric stacks. [Adapted from reference 3]

To test the recovery effect, we repeatedly expose devices to air and re-anneal it under N_2, and monitor the electron current (V_{DS} = 5 V and V_G = 50 V) [Figure 6.6(A)]. The NC FET can be attacked by oxygen, water and other chemicals at 1) the surface of the NCs and 2) the interface between the NC film and dielectric layer. As shown in section 6.2, we find that the interface between the NC film and dielectric layer plays an important role in charge transport.

We examine the effect of the interface on charge transport upon oxygen and water adsorption. When an SiO_2 gate dielectric layer is used, the device performance degrades quickly with a characteristic time constant of τ=0.14 min. However when an Al_2O_3/SiO_2 gate dielectric stack is used, the device degrades more slowly with τ=5.00 min. This clearly indicates the dominant role of interface trapping. In order to further investigate the role of dielectric layer and separate the effect of oxygen from air, we intentionally expose the device with SiO_2 and Al_2O_3/SiO_2 gate dielectric layers to pure oxygen and air [Figure 6.6 (B)]. While both devices similarly degrade upon oxygen exposure, we find that the device with SiO_2 degrades more quickly than that with an Al_2O_3/SiO_2 gate dielectric upon air exposure. This difference is consistent with greater water adsorption on the SiO_2 surface. Water is known to adsorb to surface hydroxyl groups on both SiO_2 and Al_2O_3 surfaces, but the larger concentration of surface hydroxyl versus bridged oxygen groups on the SiO_2 surface gives rise to the more acidic nature and greater water adsorption on SiO_2 in contrast to more basic Al_2O_3.[42] 3-Mercaptopropyl)trimethoxysilane (MPTS) treatment to passivate surface hydroxyl groups on the SiO_2 gate dielectric layer also reduces the device degradation (not shown here).

The recovery effect is successfully and repeatedly shown many times upon air exposure and re-annealing [Figure 6.6(C)]. As the device is annealed, oxygen and water are desorbed from the NC surface and the semiconductor-gate dielectric interface and indium diffuses from the electrodes to passivate the NC surface and restore the high performance properties [as shown schematically in Fig. 6.5(B)]. Additional indium diffusion at 200 ^{o}C does not significantly dope CdSe NC thin films, maintaining semiconducting behavior. It should be noted that CdSe NC FETs with Al contacts degrade very quickly, within 1 min of air exposure, and does not show any recovery behavior under the same annealing conditions, further supporting the indium diffusion process. As the re-annealing process is repeated, more indium diffuses into NC thin films. This leads over time to improved air stability and device performance [Figure 6.6 (C)] after several cycles of air-exposure and annealing.

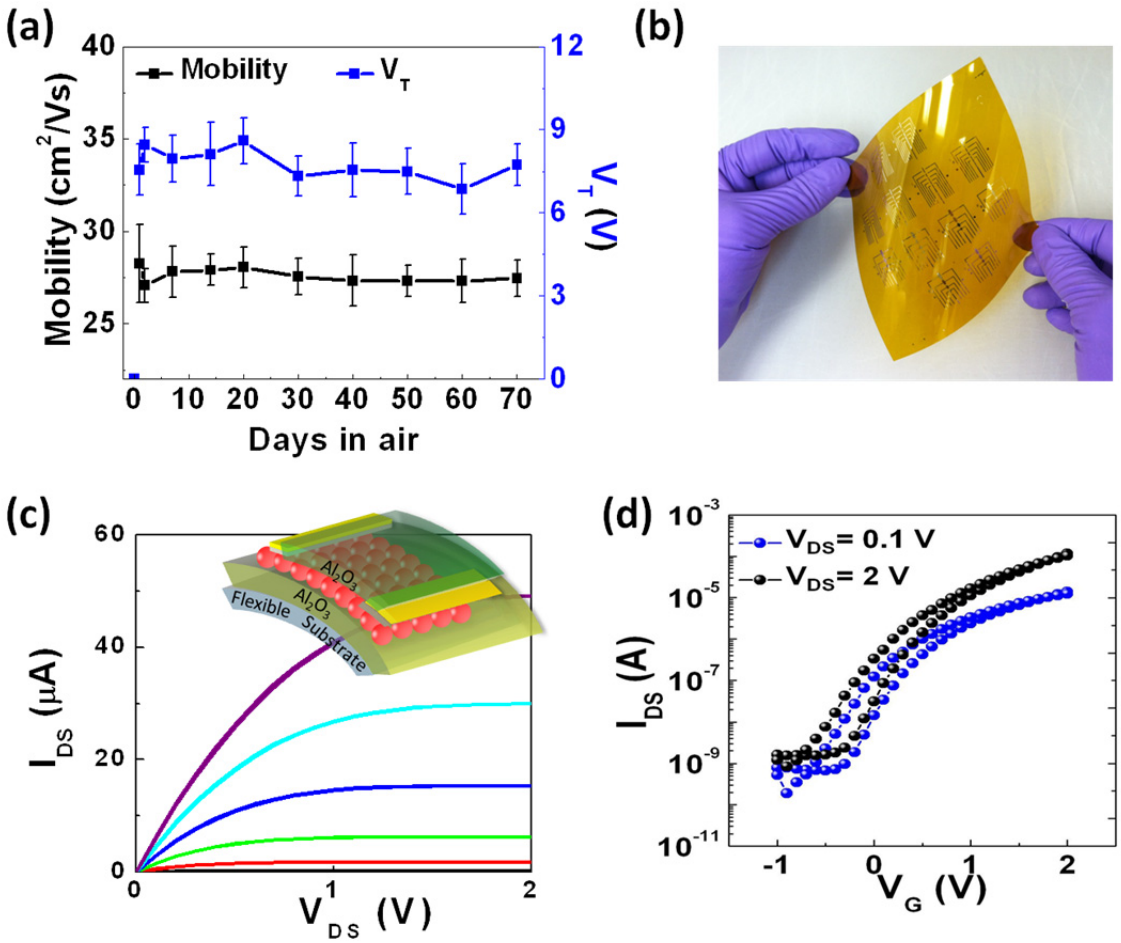

Figure 6.7. (A) Al_2O_3 encapsulated NC FET electron mobility (black) and threshold voltage (blue) as a function of time stored and operated in air. (B) A photograph of NC FETs fabricated by photolithography on flexible Kapton substrates (C) Output and (D) transfer characteristics (V_{DS}=0.1, 2V) of flexible, NC FETs (channel length L=30 μm, width W=450 μm). [inset (C)] Schematic of the device structure. [Adapted from reference 3]

We exploit this unique recovery effect to fabricate air stable devices. ALD encapsulation is known to completely passivate the NC thin films and protect them from the surroundings. However, in the previously report,[25] NC thin films had to be transferred to an ALD chamber integrated within the nitrogen-filled glovebox, preventing air exposure, as even short time exposure of NCs to air kills the device performance. Here, we utilize the ability to recover the device performance to conduct the ALD process after air-exposure in a common cleanroom tool. The temperature of 150 ºC, typically used in ALD deposition of Al_2O_3, is high enough over the time of the deposition to desorb the oxygen and water from the device and promote indium diffusion.

The air stability of these devices is tested as seen in figure 6.7 (A). The CdSe NC thin film FETs with an ALD encapsulation layer shows excellent stability without any degradation in performance over 70 days of measurement. We further utilize these methods to fabricate large area devices on flexible substrates using photolithography [Figure 6.7 (B)]. The deposition of an ultrathin 1nm of Al_2O_3 is found to prevent de-lamination of the NC thin film which otherwise happens during subsequent photolithographic patterning, developed by Yuming Lai in our group. The representative output and transfer characteristics of CdSe NC FETs are shown in figure 6.7 (C, D). The devices show air-stable and high performance FET characteristics with the mobility of ~20 cm^2/Vs and I_{on}/I_{off} of ~10^5.

In conclusion, we introduce the compact ligand, thiocyanate, to enhance the electronic coupling between NCs and fabricate high performance photodetectors. Combined with indium doping, we engineer the carrier concentration, passivate midgap

trap states, and tune the Fermi level of CdSe NC thin films to show high mobility, band-like transport properties. Last, we utilize indium passivation to demonstrate a recovery process to enable large-area, flexible, high-performance and air-stable NC device fabrication.

6.4 References

(1) Fafarman, A. T.; Koh, W.-K.; Diroll, B. T.; Kim, D. K.; Ko, D.-K.; Oh, S. J.; Ye X.; Doan-Nguyen, V; Crump, M. R; Reifsnyder, D. C. et al., J. Am. Chem. Soc. 2011, 133, 15753–15761

(2) Choi, J.-H.; Fafarman, A. T.; Oh, S. J.; Ko, D.-K.; Kim, D. K.; Diroll, B. T.; Muramoto, S.; Gillen, J. G.; Murray, C. B.; Kagan, C. R. *Nano Lett.* **2012**, *12*, 2631–2638.

(3) Choi, J.-H.; Oh, S.; Lai, Y.; Kim, D.; Zhao, T.; Fafarman, A. T.; Diroll, B. T.; Murray, C. B.; Kagan, C. R. *ACS Nano* **2013**, 8275–8283.

(4) Mashford, B.; Stevenson, M.; Popovic, Z. *Nat. Photonics* **2013**, *7*, 407–412.

(5) Cho, K.; Lee, E.; Joo, W.; Jang, E.; Kim, T. et al., *Nat. Photonics* **2009**, *3*, 2–6.

(6) Shirasaki, Y.; Supran, G.; Bawendi, M.; Bulović, V. *Nat. Photonics* **2013**, *7*, 13.

(7) Caruge, J. M.; Halpert, J. E.; Wood, V.; Bulović, V.; Bawendi, M. G. *Nat. Photonics* **2008**, *2*, 247–250.

(8) Somers, R. C.; Bawendi, M. G.; Nocera, D. G. *Chem. Soc. Rev.* **2007**, *36*, 579–591.

(9) Biju, V.; Itoh, T.; Ishikawa, M. *Chem. Soc. Rev.* **2010**, *39*, 3031

(10) Yu, W. W.; Peng, X. *Angew.Chem.-Int.Edit.* **2007**, *46*, 2559.

(11) Geyer, S. Porter, V. J. Halpert, J. E. Mentzel, T. S. Kastner, M. A.; Bawendi, M. G. *Phys. Rev. B* **2010**, *82*, 155201.

(12) Oertel, D. C. Bawendi, M. G. Arango, A. C.; Bulović, V. *Appl. Phys. Lett.* **2005**, *87*, 213505.

(13) Fratini, S. & Ciuchi, S. *Phys. Rev. Lett* **103**, (2009)

(14) Kang, M.S., Sahu, A., Norris, D.J. & Frisbie, C.D. *Nano letters* **11**, 3887-3892 (2011).

(15) Torsi, L., Dodabalapur, a, Rothberg, L., Fung, A. & Katz, H.. *Science* **272**, 1462-4 (1996).

(16) Le Comber, P. & Spear, W. *Phys. Rev. Lett* **25**, 509–511 (1970).

(17) Lee, J.-S., Kovalenko, M.V., Huang, J., Chung, D.S. & Talapin, D.V. *Nat. nanotech* **6**, 348-52 (2011).

(18) Leschkies, K. S., Kang, M. S., Aydil, E. S. & Norris, D. J. *J. Phys. Chem. C* **114,** 9988–9996 (2010).

(19) Luther, J. M. *et al. Nano Lett.* **8,** 3488–3492 (2008).

(20) Koleilat, G., Levina, L., Shukla, H. & Myrskog, S. *ACS Nano* **2,** 833–840 (2008).

(21) Oh, S. J.; Berry, N. E.; Choi, J.-H.; Gaulding, E. A.; Paik, T.; Hong, S.-H.; Murray, C. B.; Kagan, C. R. *ACS Nano* **2013**, *7*, 2413–2421.

(22) Zarghami, M., Liu, Y. & Gibbs, M. *ACS Nano* **4,** 2475–85 (2010).

(23) D. K. Kim, Y. Lai, T. R. Vemulkar, C. R. Kagan, *ACS Nano* **2011**, 5, 10074–10083

(24) A. Arico, V. Baglio, A. D. Blasi, P. Creti, *Solid State Ionics* **2003**, 161, 251.

(25) Y. Liu, M. Gibbs, C. L. Perkins, J. Tolentino, M. H. Zarghami,J. Bustamante and M. Law, *Nano Lett.* **2011**, 11, 5349–55.

CHAPTER 7 : Correlated Scanning photocurrent microscopy and scanning confocal photoluminescence microscopy to investigate the photoelectric and photophysical properties of semiconductor structures and devices

Chapter 7 introduces a novel technique, correlated scanning photocurrent microscopy (SPCM) and scanning confocal photoluminescence microscopy (SPLM), to probe charge carrier recombination, separation and transport in semiconducting materials and devices. This tool was used to 1) to map the inhomogeneities in the performance of organic solar cells arising from phase segregation and to investigate the beneficial role of compatibilizers[1] [Figure 7.1 (A)] and small molecule additives to form uniform, high performance devices[2] 2) to probe the photonic enhancement of poly(3-hexylthiophene) [P3HT] and the [6,6]-phenyl-C61-butyric acid methyl ester [PCBM] solar cells through geometrical effects introduced by wrinkles and folds[3] [Figure 7.1 (B)] 3) to study the photocurrent response and behavior in Ag_2Te,[4] CdSe,[5] and PbSe NC thin films[6] [Figure 7.1 (C)] and 4) to investigate the plasmonic enhancement of nanophosphor luminescence [Figure 7.1 (D)].[7] In this chapter, utilizing this tool, we study the fate of photoexcited charge carrier in bulk hetero junction organic solar cells.

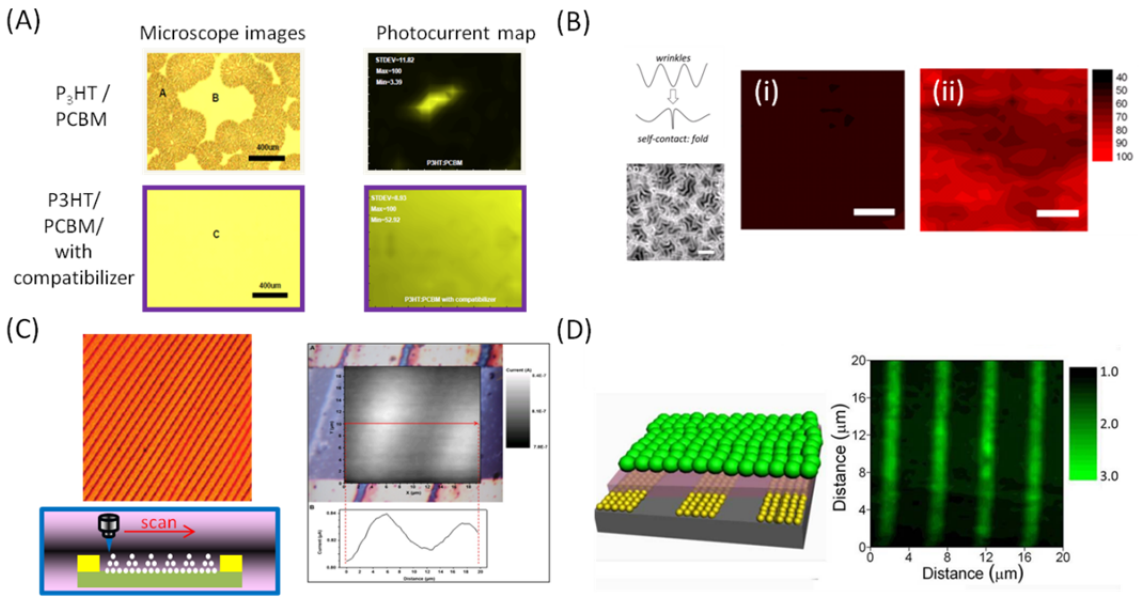

Figure 7.1 (A) Microscope image and photocurrent map of P3HT/PCBM solar cells (top) without and (bottom) with a compatibilizer.[1] (B) (left) Schematic and AFM image of wrinkles and folds and (right) the photocurrent map of P3HT/PCBM solar cells for surfaces that are (i) flat and (ii) with wrinkles and folds under 750 nm illumination[3] (C) (left, top) Photograph and (left, botom) schematic of SPCM investigation of a striped PbSe NC thin film photoconductor. (right, top) 2D, and (right, down) 1D photocurrent mapping overlaid on the optical image of a striped PbSe NC film.[6] (D) (left) Schematic and (right) photocurrent map of plasmonic enhancement of a monolayer of nanophosphors separated by an Al_2O_3 thin film from a patterned Au NP layer.[7]

7.1 Introduction

Thin film organic solar cells (OSCs) have attracted much attention due to their potential application as low-cost, high efficiency, flexible solar energy conversion devices.[8,9] The most promising and successful thin film OSC architecture is the bulkheterojunction (BHJ) structure, particularly junctions fabricated by combining a polymeric electron donor and a derivatized-fullerene electron acceptor.[10,11] In BHJs, light absorbed in the photoactive layer excites an electron-hole pair (exciton) and the exciton diffuses to an interface between donor and acceptor where photoinduced electron transfer occurs from the conjugated polymer to the derivatized-fullerene[11]. Phase separated donor-acceptor heterojunctions form throughout the three-dimensional bulk at the nanoscale on length scales comparable to the exciton diffusion length of ~10 nm.[12,13] A well-blended, bicontinuous, nanoscale donor and acceptor network is key to efficient charge separation and charge transport and collection for conversion of solar energy to electricity. Otherwise excitons recombine often by emitting light.

Thus photoluminescence (PL) quenching has generally been used as a measure of the charge separation yield.[14] As more PL quenching occurs, efficient charge transfer and separation occurs and thus higher photoconductivity (PC) is expected macroscopically.[15,16,17] When new organic materials are synthesized for OSCs, PL quenching is commonly used to evaluate their promise for photovoltaics. PL quenching and PC measurements have been correlated by probing large-area thin films.[11,15,18–20] However, at the microscopic scale, the relationship between PC and PL has not been

established and it is questionable whether PL quenching is truly predictive of photovoltaic properties.

This motivates us to study the photoelectric properties of OSCs microscopically and follow the fate of photogenerated charge carriers. We use correlated scanning photocurrent microscopy (SPCM) and scanning confocal photoluminescence microscopy (SPLM) techniques. We spatially localize the excitation and simultaneously collect photoconductivity (PC) and photo-luminescence (PL) to probe the efficiency of charge separation and recombination in BHJ solar cells from a diffraction limited spot size of 0.5 μm.

Using these technique, we probe a BHJ OSC of the polymeric donor P3HT and the derivatized-fullerene acceptor PCBM and find that higher PL is observed where PC is higher, in contrast to the generally accepted relationship that a reduction in PL is reflective of higher PC.[8] We design a model structure to study to correlate the PL and PC before and after bulk heterojunction formation. We selectively pattern a bilayer of PCBM on top of P3HT to create a step junction between P3HT only and PCBM/P3HT. As expected, higher PL and lower PC are observed in the P3HT layer and PL quenching accompanied by increased PC is seen on the PCBM/P3HT bilayer side. We then anneal the structure to allow for extended intermixing of P3HT and PCBM across the junction. We find PL and PC are proportional in the intermixed area, resembling BHJ OSCs. We carry out conductive, atomic force microscopy (cAFM) to map the hole mobility and reveal that competition between charge transport and charge separation may lead to the proportional relationship between PC and PL. We conclude that PL quenching does not

always reflect an increase of PC in well-blended, heterojunction OSCs, and therefore PL quenching is not an appropriate indicator of the photovoltaic performance of newly synthesized organic materials. This work was done in collaboration with Dr. Jongbok Kim and Prof. Yueh-Lin Loo at Princeton University.

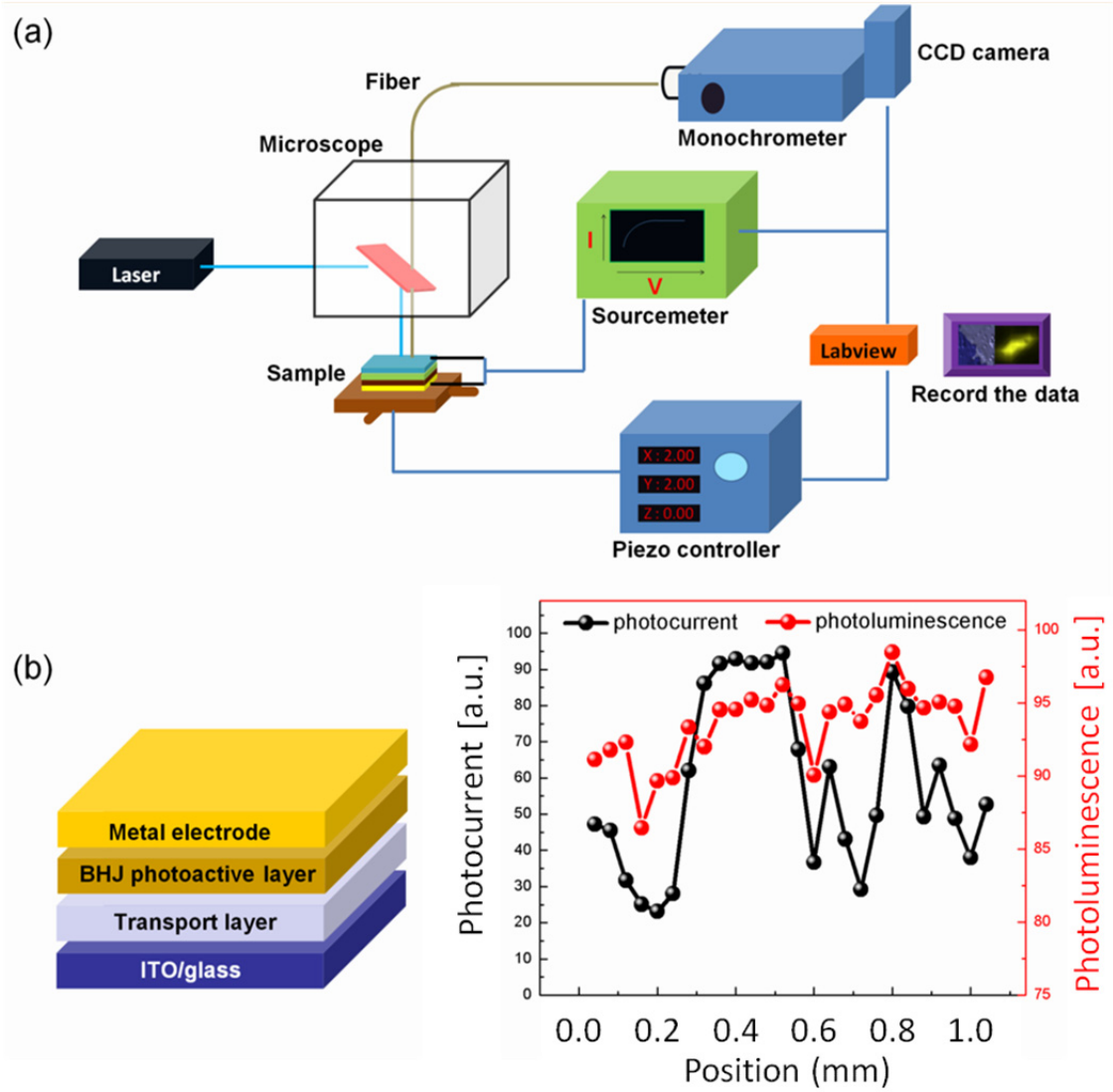

Figure 7.2 (A) Schematic of the correlated, scanning photocurrent microscopy and scanning confocal photoluminescence microscopy setup. (B) BHJ solar cell structure and (C) line scan mapping the microscopic PC and PL across a BHJ solar cell.

7.2 Experimental details

7.2.1 SPCM and SPLM on bulk heterojunction

We fabricate a P3HT:PCBM BHJ solar cell with an efficiency of 2.0%. To construct organic solar cells with a bulk-heterojunction architecture, pre-patterned ITO substrates (15 Ω/sq.; Colorado Concept Coatings) are cleaned with acetone, isopropyl alcohol and deionized water by sonication. After drying in a nitrogen stream and further cleaning by UV/Ozone for 10 min, we spin-coat a solution of 1 wt% titanium isopropoxide in isopropyl alcohol on the ITO substrates at 3000 rpm for 30 s. The precursor films are allowed to hydrolyze in air for 1 hr at room temperature followed by 10 min at 170 ^{o}C to yield 40 nm thick titania electron transport layers. A co-solution is prepared by dissolving P3HT and PCBM at an equimass ratio to form a 2.4 wt% solution in chlorobenzene. Then, the co-solution of P3HT and PCBM is deposited by spin-coating on the titania-coated ITO substrates at 500 rpm for 60 s and thermally annealed at 150 ^{o}C for 1 min. Thermal evaporation of gold through a stencil mask is used to complete the construction of P3HT:PCBM BHJ OSCs with active areas of 0.18 cm^2. The OSC is subsequently sealed by epoxy under a cover glass slip in the nitrogen glove box to prevent possible oxidation upon air exposure during measurement.

Figure 7.2 (A) depicts the experimental set-up. SPCM and SPLM measurements are carried out by illuminating the OSC through the transparent ITO top window of the device with 488 nm light from an Innova 70C spectrum Ar:Kr laser focused to a spot size of 500 nm using a 0.3 NA objective lens. The device is mounted on a stage with stepper

motors (Thorlabs BSC102) and it is scanned under the focused illumination across 100 μm x 100 μm with a step size of 0.5 μm. PC is recorded by a source meter (Keithley 2400). At zero applied voltage, the short circuit current is mapped, which allows us to locally probe the performance of the solar cell.[1] PL is simultaneously collected through the same objective lens, filtered by a super notch filter, captured confocally by a fiber and relayed to a monochrometer in combination with a CCD camera. Forward and reverse scan directions are conducted to rule out possible aging effects or biasing effects.

Figure 7.2 (B) represents the schematic of the solar cell device and Figure 7.2 (C) shows the PC and PL intensity as a function of distance. As seen in Figure 7.2 (C), the region that yields higher PC also shows higher PL. This is in direct contrast to the expectation that PL quenching induces higher PC by efficient charge separation.[15] Throughout the paper, we use the term "proportional behavior" when high PL and high PC are observed and "inversely-proportional behavior" when high PL and low PC are measured.

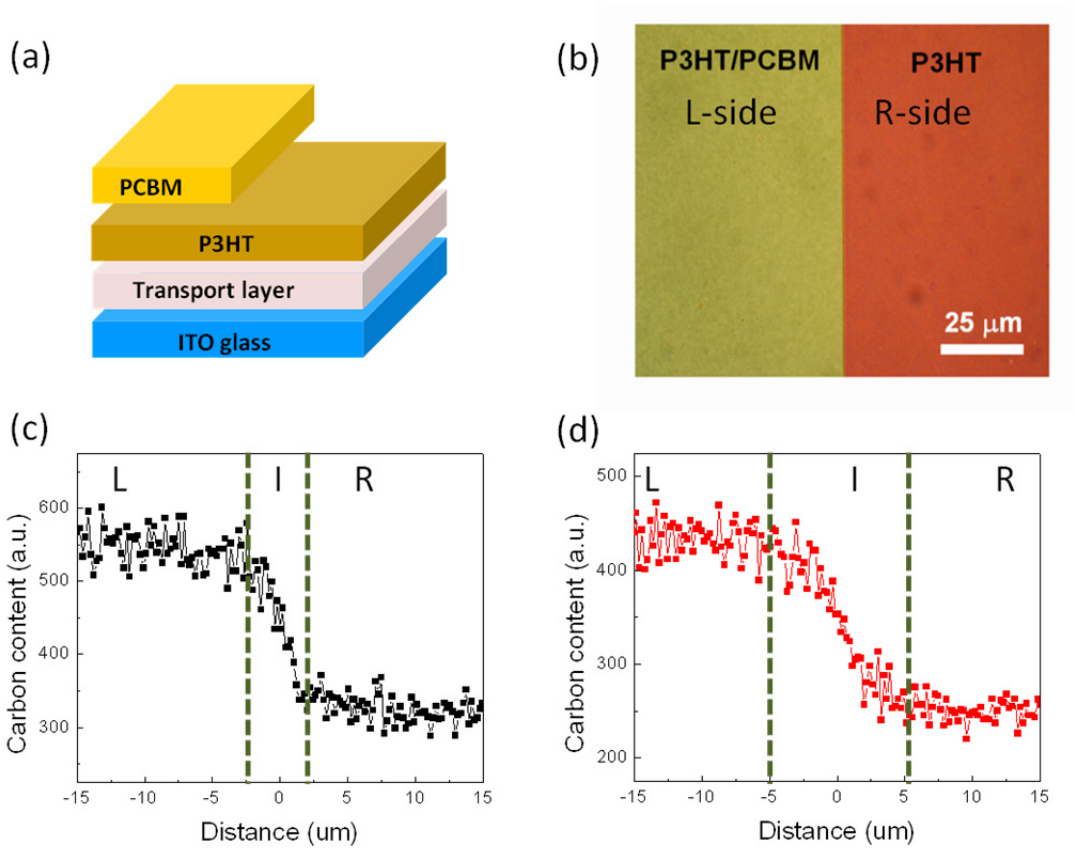

Figure 7.3 (A) Schematic and (B) photograph of the PCBM/P3HT bilayer (left) and P3HT only step junction (right). EDX mapping the carbon content (C) before and (D) after annealing at 130 ºC for 3 min.

7.2.2 SPCM and SPLM on a patterned device

To understand this phenomenon and simplify the system, we prepare a selectively patterned device using lamination[21,22] to form a PCBM/P3HT bilayer on half of the device and leave P3HT only on the other half, as shown in Figure 7.3 (A, B). To fabricate the patterned devices comprising P3HT/PCBM planar heterojunctions and single P3HT junctions, we clean pre-patterned ITO substrates with acetone and isopropyl alcohol, spin-coat PEDOT:PSS (Clevios P) at 2000 rpm for 120 s and anneal the samples at 150 ^{o}C for 20 min. Then, 1 wt% P3HT in chlorobenzene is deposited by spin-coating at 1000 rpm for 1 min. The uniform P3HT layer ensures the same light absorption across the patterned device. To selectively laminate and transfer PCBM onto P3HT and form the bilayer step junction, we prepare a 0.5 wt% PCBM solution in chloroform and spin-coat it at 3000 rpm for 60 s onto a UV/Ozone-treated Si wafer. A flat poly(dimethylsiloxane) (PDMS) stamp is prepared by mixing the PDMS precursor (Sylgard 184A) and curing agent (Sylgard 184B) at a 10:1 weight ratio. The PCBM/Si was placed in direct contact with the PDMS. The assembly is immersed in water. The water penetrates the interface between the hydrophobic PCBM and the hydrophilic UV/Ozone-treated Si wafer, allowing removal of the Si wafer and transfer of the PCBM layer onto the PDMS stamp. We then selectively laminate PCBM on half of the P3HT layer on the PEDOT:PSS-coated ITO substrate, forming a P3HT/PCBM planar-heterojunction on the left(L)-side and leaving P3HT only on the right(R)-side of the step junction. We carefully remove the PDMS stamp. Finally, we evaporate 80 nm aluminum through a stencil mask to complete the fabrication of the patterned OSC device.

This simplified step-junction architecture allows us to study the relationship between PC and PL. We denote the PCBM/P3HT bilayer side by L-side, the interdiffusion zone by I-zone and the P3HT-only layer by R-side. We expect higher PC and lower PL on the PCBM/P3HT bilayer side due to efficient charge separation,[16] and greater PL and less PC on the P3HT-only layer due to the higher probability of charge recombination in the absence of charge transfer between donor and acceptor. To characterize the structure of this device architecture, energy dispersive x-ray (EDX) elemental analysis was conducted. EDX mapping (Figure 7.3) is shown (C) before and (D) after annealing the device at 130 ºC for 3 min. A dramatic change in carbon content is seen between the L-side and R-side, with a small I-zone from -2.5μm to 2.5μm. After annealing, interdiffusion of PCBM and P3HT occurs over ~10 μm and an extended I-zone[23] forms across the mapped region from -5 μm to 5 μm. It should be mentioned that interdiffusion of PCBM occurs over very long micron-scale distances within a few minutes of annealing at 100 - 150 Cº, [23] resulting in the gradient in measured PCBM. This indicates that short time annealing can transform the bilayer of each of 50nm thickness into a complete BHJ. AFM characterization also shows similar behavior - - the step-junction becomes intermixed, reducing the variation in sample thickness upon annealing (data not shown here). No significant changes before and after annealing are observed by optical microscopy.

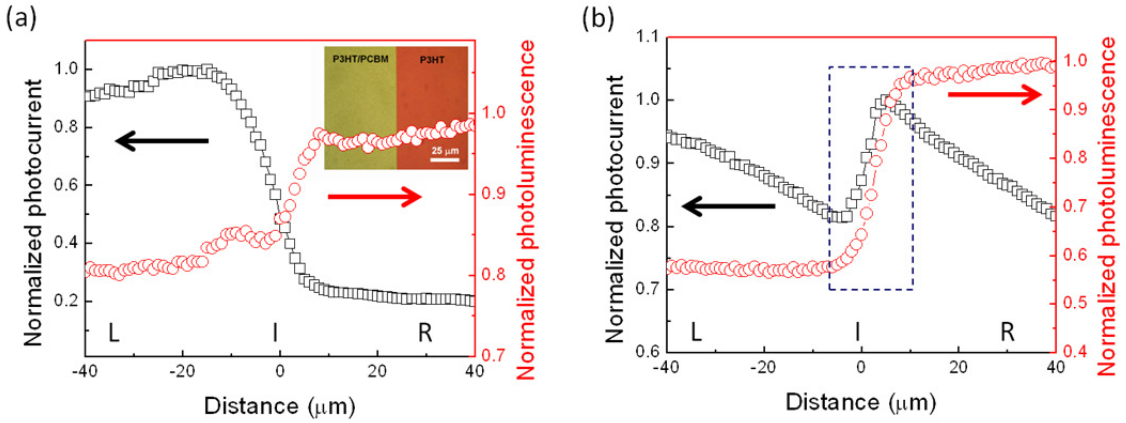

Figure 7.4. Line scan of PC and PL on a patterned device (A) before and (B) after annealing at 130 ºC for 3 min.

7.3 Results and discussions

We map the PC and PL in 1D across the junction. Figure 7.4 shows representative line scans (A) before and (B) after annealing of the full 1D scans. Before annealing, the R-side shows lower PC and higher PL, indicating that photoexcitons recombine radiatively rather than undergoing dissociation. At the L-side, higher PC and lower PL are observed, reflective of PL quenching and more efficient charge separation. After annealing, a similar phenomenon is observed on the L-side and R-side away from the junction, *i.e.* PL and PC are inversely proportional. At the L-side, a more significant PL quenching ~ 40% is observed after annealing, while there was only ~20% PL quenching before annealing. This is consistent with efficient interdiffusion, transforming the bilayer into a BHJ device.

In the I-zone before annealing [Figure 7.4(A)], the PC and PL are inversely proportional. In Figure 7.4(B) upon annealing, the I-zone extends over a larger region across the junction and in contrast, the PC and PL are directly proportional. As the device is translated from -5 μm to 5 μm [Figure 7.4(B)], the PCBM content decreases gradually [Figure 7.3(D)], and the PL increases as the probability of charge separation is reduced. However, in this region the PC is also observed to increase even though more excitons decay. As stated before, PL quenching is commonly accepted as a measure of charge separation and increased PC in organic heterojunction thin films, but here we show that PL and PC are not always inversely proportional.

To understand why the L-side of the I-zone with higher PCBM:P3HT ratio shows smaller PC even though it shows more PL quenching, we examine the contributing processes to photon to electron conversion efficiency (η_{eqe}): 1) light absorption (η_{abs}), 2) exciton diffusion (η_{diff}), 3) charge separation (η_{cs}), 4) charge transport (η_{ct}) and 5) charge collection at the electrodes (η_{cc}).[24,25]

$$\eta_{eqe} = \eta_{abs} \cdot \eta_{diff} \cdot \eta_{cs} \cdot \eta_{ct} \cdot \eta_{cc}$$

Since Ohmic contacts are formed at both the anode and cathode by using ITO and Al contacts respectively,[26] we exclude effects of charge collection efficiency at the electrodes and assume η_{cc}~1. We compare light absorption in both the L-side and R-side layer. The absorption on both sides of the junction is almost the same or perhaps slightly higher on L-side than R-side given the uniform deposition of P3HT and the small, but non-zero absorption in PCBM. If the absorption is the limiting factor, the L-side and R-side of junction should show the similar PC or slightly higher PC on L-side. Therefore we exclude the effect of absorption and assume η_{abs} is constant. After annealing, interdiffusion occurs in the I-zone. It is known and reported that the bilayer structure becomes a bulk heterojunction within a few seconds of annealing, forming effective nanoscale networks, and the efficiency becomes similar to blended device.[23] Therefore, while there may be differences in the length scale of the network with concentration, we exclude the possibility that exciton diffusion is the limiting factor and also assume η_{diff} is constant for the complete interdiffusion. Therefore we focus on the contributions charge separation and transport to the efficiency of the OSCs.

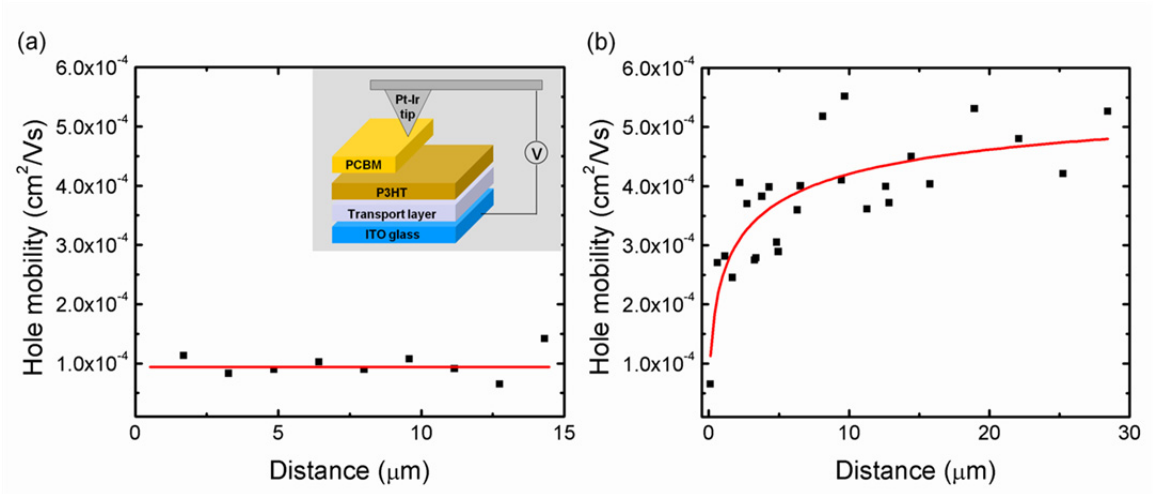

Figure 7.5 Hole mobility as a function of distance (A) before and (B) after annealing. Inset (A) a schematic of conductive atomic force microscopy characterization of the junction.

To quantify the transport properties, we carry out conductive probe, Atomic Force Microscopy (cAFM), as seen inset in Figure 7.5(A). We prepare a patterned P3HT/PCBM planar-heterojunction and P3HT single junction following procedures analogous to those used to measure PC and PL, but without depositing the cathode. We use the Pt-Ir tip in the AFM as an electrode and measured current passing through the organic semiconductor as we scan across the junction. The high work function of Pt-Ir enables us to calculate the hole mobility from the current as a function of position.

Before annealing [Figure 7.5(A)], the hole mobility is low and unchanged as a function of position across the junction as the uniform P3HT layer has poor packing density and crystallinity. After annealing [Figure 7.5(B)], the L-side (higher PCBM:P3HT ratio) shows lower mobility than the R-side. This observation is consistent with previous report[27] of an increase in hole mobility with decreasing PCBM ratio for PCBM:P3HT<0.5, as PCBM disrupts the semicrystalline packing of P3HT. In our structures the PCBM:P3HT ratio similarly changes from at most 50% (for the bilayer, L-side) to 0% (for the P3HT-only layer, R-side).

As PC is defined as $\sigma_{ph}=e(n\mu_e+p\mu_h)$,[28] mobility[29] is an important factor in photovoltaic performance. In the unannealed sample, the hole mobility is constant and therefore charge separation governs the device efficiency. However after annealing, we show that while at the L-side of the I-zone (higher PCBM:P3HT ratio) the efficiency of charge separation is higher, the lower mobility for hole transport limits the overall efficiency. At the R-side of the I-zone (lower PCBM:P3HT ratio), charge separation is less efficient so PL is high and the higher hole mobility induces higher PC. The spatial

variation of charge separation and hole mobility show that the charge separation and transport processes can compete, limiting the charge collection efficiency. It should be noted that the proportional behavior does not come from a film thickness effect as PC and PL are continuous over the scanned area and the PC and PL are inversely proportional prior to annealing.

This conclusion is further supported by previous work showing that, among samples with the different ratios of P3HT and PCBM[18] or other similar blends,[30] the greatest PL quenching does not always show the highest device photovoltaic efficiency. In addition, the high efficiency solar cells are mostly fabricated with ratios of PCBM:P3HT of 0.6-0.8:1,[31–33] which may correspond to part of our intermixed zone assuming the complete interdiffusion, rather than 1:1. This well agrees with our observation that the PCBM:P3HT gradient in the I-zone creates a gradient in carrier mobility, resulting in a change in PC that is proportional to PL in the I-zone. While we simplify the model and further study is needed to completely understand exciton dissociation, charge transfer, and the structure after interdiffusion, we believe it explains the correlation between PC and PL.

In our simplifying model structure, the intermixed zone shows clearly correlated behavior of PC and PL, due to the competition between mobility and charge separation. This region after annealing is representative of the bulk heterojunction, and therefore in BHJs, all the factors including mobility as well as charge separation should be carefully considered as important factors in the photon electron conversion process.

7.4 Conclusions

In conclusions, we studied charge recombination and separation using a correlated spatially resolved photoconductivity and photoluminescence mapping technique and further investigate charge transport using conductive atomic force microscopy. We prepare bulk heterojunction solar cells and patterned devices to study the fate of photoexcitations in OSCs. Unlike the conventional expectation where PC and PL are inversely proportional, we observed that PC and PL may be proportional in BHJs. For example, regions with higher PCBM show more PL quenching due to efficient charge separation, but lower PC arising from the lower hole mobility in P3HT. We found that this phenomenon is consistent with a competition between charge separation and transport. We conclude that in well-blend bulk heterostructures PL quenching cannot be directly used as a measure of PC or OSC efficiency, and that for efficient charge collection all factors including charge separation and mobility should be carefully considered.

7.5 References

(1) Kim, J. B.; Allen, K.; Oh, S. J.; Lee, S.; Toney, M. F.; Kim, Y. S.; Kagan, C. R.; Nuckolls, C.; Loo, Y.-L. *Chem. Mater.* **2010**, *22*, 5762–5773.

(2) Li, W.; Lee, T.; Oh, S. J.; Kagan, C. R. *ACS Appl. Mater. Inter.* **2011**, *3*, 3874–3883.

(3) Kim, J.; Kim, P.; Pégard, N.; Oh, S. J.;Kagan, C. R.; Fleischer, J. W.; Stone, H.A.; Loo, Y.-L. *Nat. Photonics* **2012**, *6*, 327-332.

(4) Liu, Y.; Ko, D.; Oh, S.; Gordon. T.; Doan-Nguyen, V.; Paik, T.; Kang, Y.; Ye, X.; Jin, L.; Kagan, C.R.; Murary, C. B. *Chem. Mater.* **2011**, *23*, 4657–4659.

(5) Fafarman, A. T.; Koh, W.-K.; Diroll, B. T.; Kim, D. K.; Ko, D.-K.; Oh, S. J.; Ye X.; Doan-Nguyen, V; Crump, M. R; Reifsnyder, D. C. et al., J. Am. Chem. Soc. 2011, 133, 15753–15761

(6) Dong, A.; Chen, J.; Oh, S. J.; Koh, W.; Xiu, F.; Ye, X.; Ko, D.; Wang, K. L.; Kagan, C. R.; Murray, C. B. *Nano lett.* **2011**, *11*, 841–846.

(7) Saboktakin, M.; Ye, X.; Oh, S.J.; Hong, S.; Fafarman, A. T.; Chettiar, U. K.; Engheta, N.; Murray, C. B.; Kagan, C. R. *ACS Nano* **2012**, 8758–8766.

(8) Gunes, S.; Neugebauer, H.; Sariciftci, N. *Chem. Rev.* **2007**.

(9) Coakley, K. M.; McGehee, M. D. *Chem. Mater.* **2004**, *16*, 4533–4542.

(10) Yu, G.; Gao, J.; Hummelen, J. *Science* **1995**, *270*, 1789.

(11) Sariciftci, N. S.; Smilowitz, L.; Heeger, a J.; Wudl, F. *Science* **1992**, *258*, 1474–1476.

(12) Halls, J.; Pichler, K.; Friend, R. *Appl. Phys. Lett.* **1996**, *68*, 3120.

(13) Haugeneder, a.; Neges, M.; Kallinger, C.; Spirkl, W.; Lemmer, U.; Feldmann, J.; Scherf, U.; Harth, E.; Gügel, A.; Müllen, K. *Phys. Rev. B* **1999**, *59*, 15346–15351.

(14) Cook, S.; Ohkita, H.; Durrant, J. R.; Kim, Y.; Benson-Smith, J. J.; Nelson, J.; Bradley, D. D. C. *Appl. Phys. Lett.* **2006**, *89*, 101128.

(15) Drees, M.; Premaratne, K.; Graupner, W.; Heflin, J. R.; Davis, R. M.; Marciu, D.; Miller, M. *Appl. Phys. Lett.* **2002**, *81*, 4607.

(16) Ohkita, H.; Cook, S.; Astuti, Y.; Duffy, W.; Tierney, S.; Zhang, W.; Heeney, M.; McCulloch, I.; Nelson, J.; Bradley, D. D. C.; Durrant, J. R. *J. Am. Chem. Soc.* **2008**, *130*, 3030–3042.

(17) Yin, C.; Kietzke, T.; Neher, D.; Hörhold, H.-H. *Appl. Phys. Lett.* **2007**, *90*, 092117.

(18) Kim, Y.; Choulis, S. a.; Nelson, J.; Bradley, D. D. C.; Cook, S.; Durrant, J. R. *J. Mater. Sci.* **2005**, *40*, 1371–1376.

(19) Ayzner, A. L.; Tassone, C. J.; Tolbert, S. H.; Schwartz, B. J. *J. Phys. Chem. C* **2009**, *113*, 20050–20060.

(20) Piris, J.; Dykstra, T. E.; Bakulin, A. a.; Loosdrecht, P. H. M. Van; Knulst, W.; Trinh, M. T.; Schins, J. M.; Siebbeles, L. D. a. *J. Phys. Chem. C* **2009**, *113*, 14500–14506.

(21) Kim, J.; Guan, Z.; Lee, S.; Pavlopoulou, E. *Org. Electron.* **2011**, *12*, 1963.

(22) Kim, J. B.; Guan, Z.-L.; Shu, A. L.; Kahn, A.; Loo, Y.-L. *Langmuir* **2011**, *27*, 11265–11271.

(23) Chen, D.; Liu, F.; Wang, C.; Nakahara, A.; Russell, T. *Nano Lett.* **2011**, 2071–2078.

(24) Clarke, T. M.; Durrant, J. R. *Chem. Rev.* **2010**, *110*, 6736–6767.

(25) Guo, J.; Ohkita, H.; Benten, H.; Ito, S. *J. Am. Chem. Soc* **2010**, 6154–6164.

(26) Blom, P. W. M.; Mihailetchi, V. D.; Koster, L. J. a.; Markov, D. E. *Adv. Mater.* **2007**, *19*, 1551–1566.

(27) Baumann, a.; Lorrmann, J.; Deibel, C.; Dyakonov, V. *Appl. Phys. Lett.* **2008**, *93*, 252104.

(28) Sze, S. M.; Ng, K. K. *Physics of Semiconductor Devices*; 3rd ed.; John Wiley & Sons: New Jersey, 2007.

(29) Kim, Y.; Cook, S.; Choulis, S. a.; Nelson, J.; Durrant, J. R.; Bradley, D. D. C. *Chem. Mater.* **2004**, *16*, 4812–4818.

(30) Snaith, H. J.; Arias, A. C.; Morteani, A. C.; Silva, C.; Friend, R. H. *Nano Lett.* **2002**, *2*, 1353.

(31) Thompson, B. C.; Fréchet, J. M. J. *Angew. Chem. Int. Ed.* **2008**, *47*, 58–77.

(32) Yun, M. H.; Kim, G.-H.; Yang, C.; Kim, J. Y. *J. Mater. Chem.* **2010**, *20*, 7710.

(33) Li, F.; Kou, L.; Chen, W.; Wu, C.; Guo, T. *NPG Asia Mater.* **2013**, *5*, e6

CHAPTER 8 Future works and Conclusions

This chapter introduces 1) a design of novel nanostructure device, 2) characterizing technique to investigate the physical properties of semiconducting nanostructures, and 3) a unique method to enhance the nanostructure optoelectronic device. First, P-N junction on a single PbSe NW and PbSe NC thin films will be designed through a partial stoichiometry control that is introduced in chapter 2 and 3. Second, SPC/PLM technique that was introduced in chapter 7 will be used to investigate the characteristic length and time of charge carriers in a single PbSe NW, PbSe, CdSe NCs thin films and the binary systems. This knowledge will be a basis to design the efficient nanocrystal device. Last, a new, post-deposited NC trap passivation method, that is an extended method of post-synthetic colloidal atomic layer deposition introduced in Chapter 3, will be introduced. This demonstrates the effective passivation of traps in the conducting NC thin films. The systematic passivation and optimization of the device will enhance the photovoltaic cell efficiency.

8.1 P-N junction on PbSe NW and PbSe NC thin films

Semiconducting NW is promising for photovoltaic applications. Especially, PbSe NW can be a great candidate due to its high mobility, large surface area and tunable bandgap. Recently, we found a unique method to change the polarity of PbSe NW and NCs to n-type and p-type[1,2] as introduced in Chapter 2 and 3. Using this method, we will fabricate horizontal p-n junction on a single PbSe NW.

First we fabricated horizontal P-N junction on PbSe NW arrays [Figure 8.1 (A)]. Using e-beam lithography, only one side (right) of PbSe NWs is exposed to O_2 briefly to make p-type[3] and covered by SiO_2 layer, while the other side (left) is covered by PMMA. After lift-off process, extra Pb atoms are deposited only on the left side of PbSe NWs to make n-type, while the right side is covered by SiO_2. The junction shows rectifying behavior [Figure 8.1 (B)] indicating the successful p- and n- doping of NWs. However, simple P-N junction formation does not guarantee the efficient photovoltaic and photo-detection application. For the efficient device application, the characteristic length such as depletion length and diffusion length should be investigated in order to prevent the charge trapping or recombination [Figure 8.1 (C)].

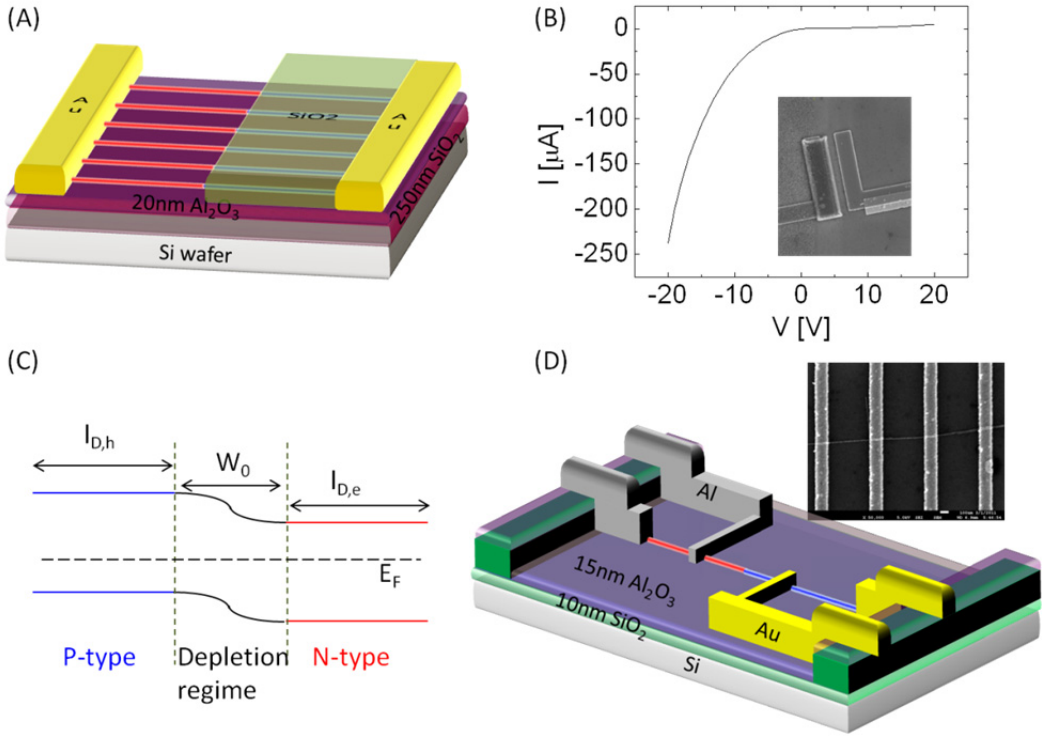

Figure 8.1 (A) Schematic of P-N junction on PbSe NW arrays, (B) Rectifying behavior or P-N junction NW array and (inset) SEM images of P-N junction with blocking layer, (C) band diagram of P-N junction on PbSe NW, and (D) schematic of P-N junction on single PbSe NW with multiple electrodes.

For photovoltaic application, open circuit voltage (V_{OC}) and short circuit current (I_{SC}) should be examined. To maximize V_{OC}, Fermi level of p-type and n-type should be investigated, which depends on the amount of Pb and Se added. By increasing Pb and Se, larger band-bending, higher built-in potential and thus higher V_{OC} is expected but if it is too much, depletion region will be decreased, so optimized level should be studied.

Channel length dependent study using multiple electrodes will be employed to investigate the diffusion and depletion length for both n-type and p-type NW [Figure 8.1 (D)]. This is not only important for photovoltaic applications, but also for principal study to examine the physical property of PbSe NW. Due to its large dielectric constant, high diffusion length would be expected, however, detail examination is needed since effective dielectric for nanostructure would be much smaller than the one for bulk and other factors such as large surface or ligands would affect. The details of the diffusion and depletion length extraction will be introduced in the chapter 8.3.

Next, a vertical P-N junction on PbSe or PbS NC thin films will be fabricated. While Schottky device has a merit of simple planar architecture, there are a few limitations[4,5]: 1) low open circuit voltages limited by Fermi level pinning 2) light absorption starts from Ohmic contacts rather than a junction so that minority carriers should travel a long distance before reaching the electrodes and therefore have a greater chance of recombination. This limitation can be solved in p-n junction device. Using Pb and Se deposition method, p-n junction solar cell will be fabricated. Diffusion length of Pb and Se atoms will be examined by varying the film thickness in FET structure.

Depletion region can be calculated by SPCM or Capacitance-Voltage measurement. The depletion region was calculated from

$$W_0 = \frac{\varepsilon_S \varepsilon_0}{C_D} = \sqrt{\frac{q\varepsilon_S \varepsilon_0 N}{2}} \left(\psi_{bi} - \frac{2kT}{q}\right)^{-1/2}$$

To calculate the depletion region, we assume the dielectric constant of 10 for PbSe NC film using effective media approximation.[6] The volume fraction for PbSe NCs is chosen to be 0.58, assuming random packing. Following Bruggeman theory, the effective dielectric constant can be calculated by:

$$\sum \frac{\varepsilon_i - \varepsilon_{eff}}{\varepsilon_i + 2\varepsilon_{eff}} = 0$$

Where ε_{air}=1, $\varepsilon_{PbSe\ NCs}$=20, and ε_{eff} is obtained as 9.6. Bruggeman Theory can be applied since it is very effective when $1/20 \leq \varepsilon_2/\varepsilon_1 \leq 20$ [6].

Using Cavity-Maxwell Garnett model:

$$\varepsilon_{eff} = \varepsilon_B \left(\frac{1 + 2f_A((\varepsilon_A - \varepsilon_B)/(\varepsilon_A + 2\varepsilon_B))}{1 - f_A((\varepsilon_A - \varepsilon_B)/(\varepsilon_A + 2\varepsilon_B))}\right)$$

ε_{eff} is calculated as 10.2

With this value of effective dielectric constant for 2.4nm PbSe NCs, depletion region can be calculated by C-V measurement. Also in Mott-Schottky plot[7], built in potential can be extracted by extrapolating the curve in C^{-2} vs V graph. Carrier concentration can be calculated by $n = \frac{2}{q\varepsilon_S}\left[-\frac{1}{d(1/C^2{}_D)/dV}\right]$

Finally, carrier concentration, built in potential and depletion layer would be explored by varying the amount of Pb and Se, and optimized photovoltaic cells can be fabricated. We will use selective doping method to achieve p-i-n structure which can maximize photovoltaic performance.

8.2 Investigate the carrier physics in PbSe, CdSe NC and binary NC thin films.

As shown in chapter 7, SPCM/SPLM is a strong tool to understand the electronic, optoelectronic and photovoltaic properties of semiconductor. This technique was used to investigate charge separation, recombination and transport for organic/inorganic semiconductor. Here we will employ SPCM/SPLM to study the detail of diffusion and depletion length. Combining with time resolved photoconductivity, transit times and profiles of carrier transport will be studied. This provides the insight to design the electronic and optoelectronic structures.

A localized illumination creates excess carriers in a small spot and generates electron concentration gradient. This allows us to study the space dependence of excess charges. From the continuity Equation and low injection condition, the decay of excess carriers with distance when one side(x=0) is illuminated can be expressed as[7]

$$\frac{\partial p_n}{\partial t} = 0 = -\frac{p_n - p_{n0}}{\tau_p} + D_p \frac{\partial^2 p_n}{\partial x^2}$$

With a set of proper boundary condition of $p_n(0)$=constant and $p_n(\infty)=p_{no}$, the carrier concentration will be the exponential function as[7]

$$p_n(x) = p_{no} + [p_n(0) - p_{no}]\exp\left(-\frac{x}{L_p}\right)$$

where Lp is the diffusion length. By fitting with an exponential function where $I=I_o\exp(-x/l_D)$, the diffusion length can be achieved. By extracting the diffusion length, carrier recombination life time can be also calculated from the $\tau= ql_D^2/\mu k_B T$, if μ is known. However, the field effect mobility cannot be directly used here to extract the lifetime. Most of nanostructures inherently have many surface-related defect and trap states. In the field effect geometry, those traps are filled with the gate bias that shifts the Fermi level, and higher mobility is extracted. However in the absence of the gate bias, such as in a photodetector or photovoltaic cell, the actual mobility would be lower than that. Therefore, it is desirable to extract the lifetime directly and calculate the field-less mobility for solar cell application.

One of the method to calculate the lifetime is using a pulsed light instead of localized light. When a pulsed light uniformly shine the n-type semiconductor, electrons are excited with a uniform generation rate G_p.[7]

$$\frac{\partial p_n}{\partial t} = G_p - \frac{p_n - p_{no}}{\tau_p}$$

Similarly, with the appropriate boundary conditions of $p_n(0) = p_{no} + \tau_p G_p$ and $p_n(\infty)=p_{no}$, the solution is extracted as[7]

$$p_n(t) = p_{no} + \tau_p G_p \exp\left(-\frac{x}{\tau_p}\right)$$

From this equation, we can solve the lifetime.

When a localized and pulsed light is introduced, both the lifetime and diffusion length can be extracted. With this method, the surface recombination rate of semiconductor, or number of surface trapping centers per unit area, can be also extracted as well.

This technique can be used to probe the carrier behavior in not only a single nanowire but also PbSe NC and CdSe NC thin films and/or these two or other binary NC thin films. From the knowledge we learned, we can build an efficient p-n junction on PbSe NCs or PbSe/other semiconductor NCs thin films as well as on a single PbSe NW.

8.3 Post trap-passivation for high efficiency PbS NC solar cell.

Lead chalcogenide NCs has been shown a great process in solar cell application in a decade. Most successful geometry is the heterojunction structure[8] which consists of titanium oxide and PbS layer. TiO_2 layer acts as an electron collector. Ideally, a highly doped TiO2 layer will create a long depletion region in a lightly doped PbS NC layer. PbS NC thin films actually absorb the light, create and exciton, and separate them to create a free current. However, PbS NCs have a lot of surface-related trap and defect states within the band gaps. The traps collect the charge carriers by recombination. Researchers place a great importance to passivate the trap states to enhance the photovoltaic properties, and actually there has been a great progress. Recently, Sargent group[9] and Matt Beard group[10] add $PbCl_2$ or $CdCl_2$ during or right after synthesis to passivate the trap states that will otherwise be created during ligand exchange process.

Trap sites are known to be generated during ligand exchange or washing process with alcoholic solvents as they can remove the surface metal atoms. Adding Cd to the surfaces can prevent the loss of surface metal-Pb atoms during ligand exchange. However, it is still hard to imagine the pre-Cd passivation can 100% guarantee to prevent the loss of surface of atom and defect formation.

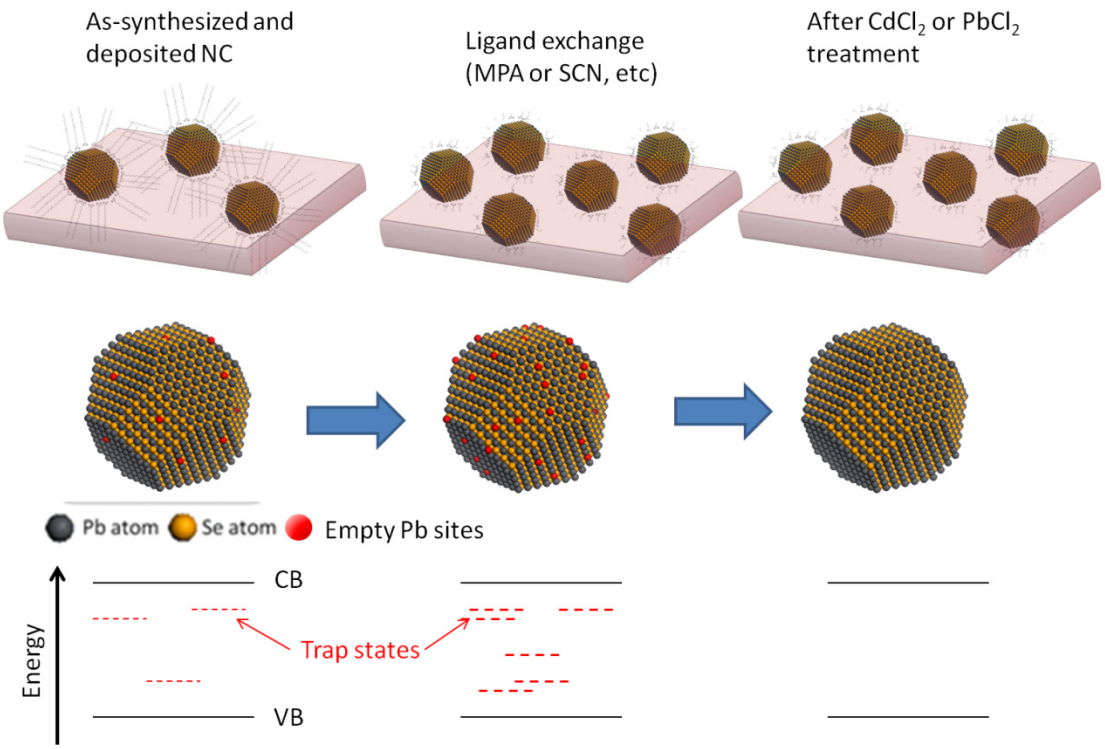

Figure 8.2 Schematic of Post-deposited Passivation of trap states in NC thin films

Here, we propose the post-deposited passivation method to completely fill the empty metal sites and passivate the surface-related defect states. [Figure 8.2] It is no wonder that the most efficient timing to fill the trap would be right after the formation of trap. In chapter 3, we showed that $PbCl_2$ treatment triggers the reaction of Pb ion from $PbCl_2$, and surface chalcogenide from NCs.[2] We will use similar method to passivate the trap sites. NC thin film solar cell is fabricated using MPA treatment, which is known to show the best photovoltaic performance.[9] However, this fast dynamics of MPA ligand exchange process is known to form the surface traps due to incomplete ligand exchange and removal of surface metals.[11] The empty metals sites, that are actually surface chalcogen sites, will be covered with $PbCl_2$ or $CdCl_2$ treatment by obtaining metal ions. This process can efficiently fill the trap sites. We fabricate the heterojunction PbS NC solar cells, [Figure 8.3 (A)] and show that this treatment enhances the photovoltaic performance by two folds [Figure 8.3 (B)]. It is also possible that there would be chalcogen empty sites, and those can be filled by Cl or extra BDT or MPA treatment.

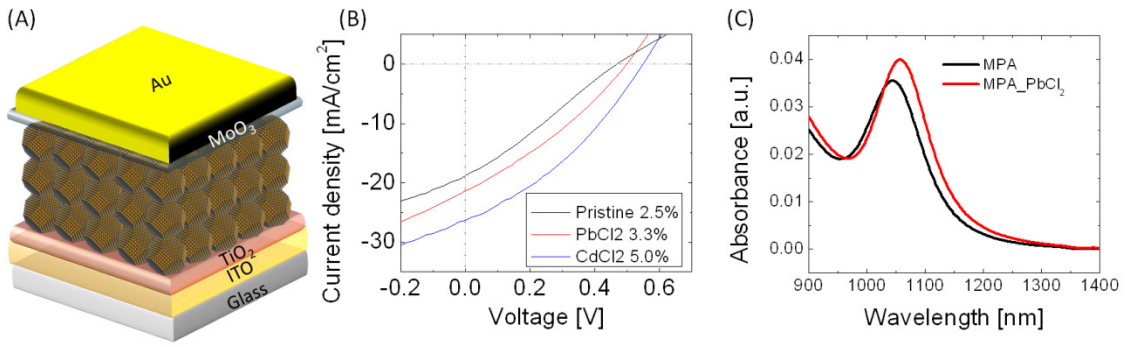

Figure 8.3 (A) schematic of heterojunction PbS NC solar cell, (B) the efficiency of PbS solar cell before and after $PbCl_2$ and $CdCl_2$ treatment, and (C) the absorption spectroscopy of MPA-treated PbS NC thin films before and after $PbCl_2$ treatment.

EDX measurements successfully show that $PbCl_2$ treatment increase the Pb: Se ratio of SCN or MPA treated NC thin films, indicating the filling of surface empty lead sites. Also the effective covering of empty metal sites with additional Pb can enhance its crystallinity of NCs. This effectively fills the mid-gap and tail states, resulting in the decrease of fwhm of excitonic peak of NC thin film [Figure 8.3 (C)]

The systematic passivation of traps and optimization of the device will enhance the photovoltaic performance.

8.4 Concluding Remarks

The goal of this thesis is to understand the fundamental physics of charge carrier behavior in nanocrystals, engineer the charge carrier properties and statistics through novel method, and design the high performance electronic and optoelectronic nanocrystal devices.

In chapter 2 and 3, we introduce the novel method to engineer the electronic properties of nanocrystal thin film solids. We for the first time demonstrate that carrier statistics in nanocrystal (NC) thin film solids can be precisely controlled by stoichiometric imbalance through thermal evaporation of elemental excess. Using this method, we achieved the highest reported mobility in lead chalcogenide NC field-effect transistors (FETs) and enhanced the power conversion efficiency in PbSe NC Schottky solar cells. Furthermore, we develop a simple, solution based post-synthetic colloidal Atomic Layer Deposition method to control the stoichiometry and electronic properties of NC device and design a low-cost and high performance NC device.

In chapter 4, we study the fundamental physics of charge injection and transport in electronic NC device. While the literature on NC electronics only focuses on charge transport, here we emphasize the important role of charge injection at the interface between metal and NCs to achieve high performance electronic device.

While the study was focused on lead chalcogenide nanocrystals so far, in chapter 5, we study the nanowire system. The charge injection and transport are studied with temperature dependent electrical measurement, and uncover that PbSe NW FET behaves

as Shottky barrier FET. Unlike nanocrystals that mostly shows hopping transport, we show the band transport of nanowire, indicating the single crystalline materials. In this work, that remote doping in nanostructures is a promising route to dope nanostructures and to realize high mobility and reduced scattering, in contrast to commonly pursued substitutional doping.

In chapter 6, we study the different nanocrystals, cadmium chalcogenide nanocrystals. We fabricate the high sensitive photodetectors and air-stable, large area, flexible, and high performance field effect transistors. We demonstrate the band-like transport in nanocrystals thin film through the strong electronic coupling and In-doping. We emphasize that the interface between nanocrystals thin film and gate dielectric layers plays an important role for the charge carrier trapping.

In chapter 7, we study the charge carrier behaviors *under* illumination. Correlated scanning photocurrent microscope and scanning confocal photoluminescence measurement is introduced to understand charge generation, separation, and recombination in nanocrystal, organic, and inorganic photoconductors and completed solar cells. With this technique, we study the fate of photoexcited charge carrier in bulk hetero junction organic solars.

Chapter 8 introduces the future works including the characterization technique to investigate the photogenerated charge carriers in nanocrystals solids, an original design of nanocrystals structures, and novel methods to tailor the photoexcited carriers, essential in optimization and development of the nanocrystal devices

I hope this thesis will provide the understanding of the physics of the charge carrier in nanocrystal solids, and new insights to further develop the nanocrystal devices.

8.5 References

(1) Oh, S. J.; Berry, N. E.; Choi, J.-H.; Gaulding, E. A.; Paik, T.; Hong, S.-H.; Murray, C. B.; Kagan, C. R. *ACS Nano* **2013**, *7*, 2413–2421.

(2) Oh, S. J.; Berry, N. E.; Choi, J.-H.; Gaulding, E. A.; Lin, H.; Paik, T.; Diroll, B. T.; Muramoto, S.; Murray, C. B.; Kagan, C. R. *Nano Lett.* **2014**, *14*, 1559–1566.

(3) Oh, S. J.; Kim, D. K.; Kagan, C. R. *ACS Nano* **2012**, *6*, 4328–4334.

(4) Tang, J.; Sargent, E. *Adv. Mater.* **2011**, *23*, 12–29.

(5) Barkhouse, D.; Debnath, R. *Adv. Mater.* **2011**, *23*, 3134–3138.

(6) Webman, I.; Jortner, J.; Cohen, M. *Phys. Rev. B* **1977**, *15*.

(7) Sze, S. M.; Ng, K. K. *Physics of Semiconductor Devices*; 3rd ed.; John Wiley & Sons: New Jersey, 2007.

(8) Maraghechi, P.; Labelle, A. J.; Kirmani, A. R.; Lan, X.; Adachi, M. M.; Thon, S. M.; Hoogland, S.; Lee, A.; Ning, Z.; Fischer, A.; Amassian, A.; Sargent, E. H. *ACS Nano* **2013**, *7*, 6111–6116.

(9) Ip, A. H.; Thon, S. M.; Hoogland, S.; Voznyy, O.; Zhitomirsky, D.; Debnath, R.; Levina, L.; Rollny, L. R.; Carey, G. H.; Fischer, A.; Kemp, K. W.; Kramer, I. J.; Ning, Z.; Labelle, A. J.; Chou, K. W.; Amassian, A.; Sargent, E. H. *Nat. Nanotechnol.* **2012**, *7*, 577–582.

(10) Zhang, J.; Gao, J.; Miller, E. M.; Luther, J. M.; Beard, M. C. *ACS Nano* **2014**, *8*, 614–622.

(11) Thon, S. et al., *ACS nano* **2013**, *7,* 7680–7688